Holocene climate trends in NW Africa:

Inferences from grain-size distributions of terrigenous sediments and isotopic provenance studies

Dissertation

for the doctoral degree in natural sciences
(Dr. rer. nat.) at the

Faculty of Geosciences of Bremen University

submitted by
Inka Meyer

Tag des öffentlichen Kolloqiums
02.05.2011
12 Uhr c.t., Geo-Hörsaal 1550

Gutachter der Dissertation
Prof. Dr. Dierk Hebbeln
PD. Dr. Matthias Zabel

Prüfer
Prof. Dr. Simone Kasemann
Dr. Jan-Berend Stuut

Weitere Mitglieder des Prüfungsausschusses
Dr. Furu Mienes
Stefan Braun

Declaration

Name: Inka Meyer

Date: 01/ 31/ 2011

Address: Kötnerhöfen 9, 28832 Achim

Herewith I declare that

I. this document and the accompanying data has been composed by myself, and describes my own work

II. material from the published or unpublished work of others, which is referred to in the dissertation, is credited to the author in the text

III. this work has not been submitted for any other degree

Bremen, 01/ 31/ 2011

(Signature)

„...but he shed a rain of blood upon the earth in honour of his son...“

Homer‘s *Illiad*
(~ 750 BC)

Preface

This PhD thesis is compiled to establish the characteristics and impact of short-term climate changes on the arid regions of NW Africa during the Holocene. Paleoclimate reconstructions were made on a set of deep-sea sediment cores which were characterized by undisturbed deposition, from offshore Morocco, the Western Sahara, Mauritania, and Senegal. Deep-sea sediments are known to form a natural high-resolution archive of past climate variability provided by the sediments accumulating on the seafloor. Marine sediment cores along the NW African coast record the variations of terrigenous input (both aeolian dust and fluvial matter) from the African continent, which was used to study the variable continent-ocean dynamics between sediment transport processes in the proximal marine environments off NW Africa and the evolution of the continental climate during the Holocene. Different methods including grain-size measurements, end-member modeling and the investigation of strontium and neodymium isotopes were used to reconstruct the environmental evolution on land.
The thesis consists of a series of papers and manuscripts that have been published, submitted for publication, or are ready for submission in international peer-reviewed scientific journals. All references are provided in a single reference list at the end of this thesis. A short summary of the different chapters is given below.

Chapter 1 provides a brief introduction into the global topic of dust and clarifies the scientific motivations and objectives of this thesis. Major tasks and questions are listed.

Chapter 2 presents information about the area of investigation and gives a short review about the modern climate and the Holocene climate evolution as well as a short introduction into the geology of NW Africa.

Chapter 3 specifies the sedimentological processes offshore NW Africa, and gives a brief review about provenance studies. Furthermore, marine sediment cores and dust filter samples investigated within this thesis are listed.

Chapter 4 presents details on sampling techniques, chemical treatments and analytical procedures used for the grain-size measurements and provenance studies.

Chapter 5 addresses the discussion if and to which extent the isotopic composition of strontium and neodymium is influenced by differences in grain size. The data confirm that the isotopic composition of strontium varied as a function of grain size, whereas the isotopic composition of neodymium appeared unaffected by variation is particle size. Furthermore, strontium and neodymium were used to ascertain the provenance of the terrigenous fraction as well as to

reconstruct temporal variations in the NW African weathering regime since the Younger Dryas.

Chapter 6 deals with the question of changes in the latitudinal position of the transition zone between the monsoonal and the North Atlantic climate system over NW Africa. Grain-size measurements, end-member modeling, isotopic and mineralogical investigations were carried out on four marine sediment cores offshore NW African between 30°N and 20°N. The results suggest that the influence of the North Atlantic climate system reached at least down to 26°N during the Younger Dryas. During mid-Holocene times the boundary between both climate systems gradually shifted further north over almost 3° latitude, followed by a small shift southward (~1° latitude) towards the present.

Chapter 7 refers to the spatial and temporal variations of short-term climate events within NW Africa during the Holocene. The study was accomplished using seven deep sea sediment cores from the NW African continental margin. The characterization of terrigenous sediments is used to detect differences and local imprints along the coast. Results show that the input of terrigenous material and the characteristics of both, aeolian fraction and fluvial material differ between nearby core locations, due to local features. Hence, climate reconstructions for the entire NW Africa based on the investigation of single sediment cores are probably dominated by more local imprints, and can hardly be used for general climatic predictions.

Chapter 8 is focused on the increase in dust flux since the last 3.200 years within the Sahel region. In order to gain information about the human contribution to land degradation and dust mobilization the chemistry and grain-size distributions of the terrigenous sediment fraction were studied. The results show that the enhanced dust deposition since the beginning of the nineteenth century coincides with the beginning of commercial agriculture in the area.

Chapter 9 summarizes the key findings of this PhD thesis and provides answers to the major scientific issues, specified in Chapter 1. Furthermore, perspectives for presently ongoing studies as well as open questions are briefly mentioned.

Abstract

On a global scale fluvial sediments, transported by rivers to the world's oceans, provide the major component in deep sea sediments, amounting to about ten times the total mass that is transported from all deserts combined. In contrast, offshore the NW African coast the most important constituent of the terrigenous fraction is aeolian dust, delivered by different wind systems to the Atlantic Ocean. In the region downwind the Saharan Desert, the world's biggest source of desert dust, aeolian input exceeds the fluvial supply by a factor of ten. Records of aeolian dust and fluvial matter in marine sediments provide one of the most detailed and best preserved sources of paleoclimatic information, in particular to define past hydrological conditions, changes in transport mechanisms, and provenance of terrigenous material as well as the extent of human-induced dust mobilization by land degradation.

The objective of this PhD thesis is the documentation of the temporal and spatial variability of fluvial vs. aeolian input offshore the Saharan Desert and the examination of the provenance of the terrigenous fraction during the Holocene. Compared to the vast glacial-interglacial variations of the Pleistocene, the Holocene climate has been rather stable but is characterized by a number of high-amplitude short-term variations like the Younger Dryas, at the transition between the Pleistocene and the Holocene epoch, and the Holocene Climate Optimum, which is called the "African Humid Period" within the NW African realm. Therefore, the Holocene is well suited to examine potential controls of climate change in a region which is likely to react extremely sensitive to future climate change. The presented investigations were carried out on a set of marine sediment cores retrieved from the continental slope offshore Morocco, the Western Sahara, Mauritania, and Senegal. Using grain-size measurements and end-member modeling the study shows that the terrigenous material in deep-sea sediments between 30°N and 15°N are composed of variable amounts of aeolian and fluvial sediments, which is linked to prevailing climate conditions on land (Chapters 6 and 7). The results indicate that regions south of 30°N are mainly influenced by the seasonal shifts of the NW African monsoonal rainbelt. During the Younger Dryas coarse aeolian dust is the most important sediment component, demonstrating arid and windy conditions on land. In contrast, the mid-Holocene is characterized by enhanced deposition of fluvial material, coinciding with the African Humid Period. Within late Holocene times, fine aeolian dust is the dominant sediment component, reflecting modern dry conditions over NW Africa. North of 30°N terrigenous sediments are mainly governed by variations of the North Atlantic climate system. Furthermore, the data exhibit that the impact of local features has a stronger influence on the terrigenous sediment supply, than commonly anticipated (Chapter 6).

Based on strontium and neodymium isotope measurements, provenance studies and a reconstruction of temporal variations in the NW African weathering regime were carried out. Measured neodymium values indicate that the geological sources of terrigenous material were

nearly constant over the last ~12 ka. In contrast, variations in Sr isotope ratios reflect major changes in the evaporation/precipitation balance and hence the rate of chemical weathering. The data document latitudinal shifts of the transition zone between the African monsoonal climate system south of the Saharan Desert, and the Mediterranean climate regime in the North, causing abrupt and persistent changes in the humidity and rate of chemical weathering over NW Africa since the Younger Dryas (Chapters 5 and 6).

Furthermore, the results presented in this thesis indicate that human activity influences dust emission through agriculture and land-use in a region extremely sensitive to changes in precipitation (Chapter 8). Data suggest that human dust production through land use exceeds natural dust production by far.

Zusammenfassung

Auf globaler Ebene bilden fluviale Sedimente, die über Flüsse in die Meere der Welt eingetragen werden, den Hauptbestandteil mariner Sedimente. Insgesamt wird zehn Mal mehr Flussfracht als Staub, der aus Wüsten und Trockengebieten der Welt ausgeblasen wird, am Meeresboden abgelagert. Die Meeressedimente vor der nordwest afrikanischen Küste zeigen jedoch ein anderes Bild. Hier übersteigt der Staubeintrag aus der Sahara, der weltweit größten Quelle an Wüstenstaub, den Eintrag der Flüsse um ein Zehnfaches. Sedimente aus den der Sahara vorgelagerten Regionen bestehen somit hauptsächlich aus äolisch transportierten Partikeln. Die Ablagerung von wind- und flusstransportierten Sedimenten am Meeresboden bildet eines der hoch-aufgelösten und am besten erhaltenen Archive für paläoklimatische Untersuchungen. Insbesondere dienen sie der Rekonstruktion von hydrologischen Bedingungen an Land sowie der Veränderungen innerhalb der Transportmechanismen und Herkunftsgebiete. Des Weiteren lassen sich mit Hilfe der von Land eingetragenen Sedimente die Folgen menschlichen Handelns, in Form von zu intensiver Landnutzung und somit erhöhter Staubproduktion ermitteln.

Das wissenschaftliche Ziel dieser Doktorarbeit ist es, die räumlichen und zeitlichen Eintragsmuster terrigener Sedimenten in den Meeresablagerungen vor der Sahara während der letzten ~ zwölftausend Jahre (Holozän) zu untersuchen und ihre Herkunftsgebiete zu bestimmen. Verglichen mit den extremen Klimaschwankungen des Pleistozäns, ist das holozäne Klima zwar recht stabil, aber dennoch durch einige ausgeprägte und kurzweilige Klimaschwankungen gekennzeichnet. Beispiele hierfür sind die Jüngere Dryas am Übergang zwischen dem Pleistozän und dem Holozän oder das Holozänen Klimaoptimum, welches in Afrika als „African Humid Period“ bezeichnet wird. Durch diese Schwankungen ist das Holozän besonders gut für die Untersuchung einer Klimaregion geeignet, die voraussichtlich extrem sensibel auf zukünftige Klimaveränderungen reagieren wird.

Die vorliegende Arbeit basiert auf der Untersuchung mariner Sedimentkerne, die am Kontinentalhang vor Marokko, der Westsahara, Mauretanien und dem Senegal erbohrt wurden. Durch Korngrößenanalysen der terrigenen Sedimentfraktion und den daraus errechneten Endglied-Korngrößenverteilungen für wind- und fluvial transportiertes Sediment war es in dieser Arbeit möglich zu zeigen, dass die marinen Sedimente zwischen 30°N und 15°N aus beiden Sedimentkomponenten bestehen (Kapitel 6 und 7), und das deren jeweilige Menge Rückschlüsse auf das vorherrschende Klima in NW Afrika zulässt.

Die Regionen südlich von 30°N werden hauptsächlich durch die saisonale Verlagerung des NW afrikanischen Monsuns beeinflusst. Während der Jüngeren Dryas weist die Ablagerung von gröberen Staubpartikeln auf trockenes Klima und höhere Windgeschwindigkeiten hin. Im Gegensatz dazu wurde während des mittleren Holozäns verstärkt Flußfracht abgelagert, was auf die feuchten Bedingungen während der „African Humid Period“ zurückzuführen ist. Während des späten Holozäns spiegelt die Ablagerung von feinem Staub die trockenen

Klimaverhältnisse in NW Afrika wieder. Nördlich 30°N werden die Sedimente hauptsächlich durch das Nord Atlantische Klima beeinflusst. Weiterhin zeigen die gewonnenen Daten, dass lokale Eigenschaften die Verteilung der vom Land eingetragenen Sedimente stärker beeinflusst als bisher angenommen (Kapitel 6).

Um mögliche Herkunftsgebiete der terrigenen Sedimente ermitteln zu können und um die zeitlichen Veränderungen im Verwitterungsverlauf während des Holozäns zu rekonstruieren, wurden die Isotope der Elemente Strontium und Neodym am Sediment untersucht. Die gemessenen Neodym-Werte weisen darauf hin, dass sich die geologischen Quellgebiete während der letzten zwölftausend Jahre nicht geändert haben. Im Gegensatz dazu zeigen die gemessenen Strontium Isotope starke Schwankungen im Verhältnis zwischen Niederschlag und Verdunstung und somit der chemischen Verwitterung. Die Daten dokumentieren eine Nord-Süd-Verschiebung der Übergangszone vom NW afrikanischen Monsunklima im südlichen Gebiet der Sahara und des mediterranen Klimasystems im Norden. Diese Verschiebung verursachte, seit der Jüngeren Dryas, abrupte und nachweisbare Änderungen in der Feuchtigkeit und der chemischen Verwitterungsrate in NW Afrika (Kapitel 5 und 6).

Des Weiteren zeigen die Daten dieser Arbeit, dass die Emission von Saharastaub innerhalb des sensiblen Klimasystems NW Afrikas, durch menschliche Einflussnahme in Form von falscher oder zu starker Landnutzung extrem beeinflusst wird (Kapitel 8). Die Untersuchungen belegen, dass der durch den Menschen verursacht wird Staubaustrag, den natürlichen bei weitem übersteigt.

Acknowledgements

During my time at the MARUM many people have supported me in different ways and together we have made this thesis into what it is now.
First I would like to thank Prof. Dr. Dierk Hebbeln for offering me this PhD thesis embedded within EUROPROX project III-16. I am grateful to Prof. Dr. Helmut Willems, the chairman of the European graduate college 'Proxies in Earth history' (EUROPROX), and many others EUROPROX members, for making my PhD project possible. All the PhD's and Post-docs of EUROPROX is thanked for fruitful discussions at our "Coffee & Science"-meetings.
I would like to thank the members of my thesis committee Prof. Dr. Dierk Hebbeln, Dr. Jan-Berend W. Stuut, Dr. Christoph Vogt and PD Dr. Matthias Zabel. Their constructive comments and encouragements helped me in planning my work and focusing scientific problems.
Furthermore, I would like to thank a lot of colleagues from the MARUM. First of all, thanks to Marco Klann, I really appreciated your help in looking for samples, for organizing all the labs during our cruises and collecting dust. Alex Wülbers is thanked for always having a table for me. I am grateful to Britt Kokisch for introducing me to the Atterberg-methods and for laboratory assistance. Sincere thanks are given to Wolfgang Bevern for solving several lab problems.
Sincere thanks are also given to Prof. Dr. Bernd Zolitschka from the Department of Geography, University Bremen, who managed to spark my interest in science during my studies.
I would also like to thank some colleagues and friends from the VU Amsterdam. Thanks to Bas van der Wagt, Martijn Klaver and Prof. Dr. Gareth Davies for technical help and assistance in the labs at the VU. I am particular grateful to Richard Smeets for all the help in the clean-lab and with chemical procedures at the VU. Furthermore, I am very thankful to Josepha Kempl for all the nice evenings in Amsterdam.

I gratefully acknowledge to my supervisor Dr. Jan-Berend W. Stuut how opened many doors for me during the last years. Jan-Berend, without your tireless support and optimism, I wouldn't have finished this piece of work with so much fun. Thank you for always pushing me, for introducing me to so many people, for all the help and all the discussions. I will never forget the funny times (as well as scientific discussions...) we had in the lab, during TV sessions, at conferences or even in the middle of the Saharan Desert. Thank you so much for showing me, how science really works!!
I am also very thankful to my second supervisor Dr. Maarten Prins, from the VU Amsterdam. Thank you, for taking care of me during my time in Amsterdam and for sharing a lot of coffees with me. I'm looking very forward to come again!

I thank all my colleagues from my "working group" and our "10 am coffee break", Gema

Martinez-Mendez, Furu Mienis, Jürgen Titschak, Claudia Wienberg, Marko Mohtadi, Jutta Bülten, Christina Klose, Markus Eisele, Hiske Fink, Rike Zimmermann and even they are not part of the group anymore, thanks to Gabi Ratmeyer, Uta Brathauer and Eva Niedermeyer. Furu and Jürgen is thanked for helping with the text and all the discussions during the last weeks.

I am grateful to my lunch-team Lars Hoffmann-Sell, Nick Rackebrandt and Hiske Fink for nice lunch breaks and lots of fun.
Thanks to my (former) office mates: Markus, Hiske and Eva – you were really the perfect combo!! And to the new 1340-crew: still Markus, still Hiske and Rike – stay as you are!!
Furthermore, some colleagues from the FB5 should be mentioned as well. I am grateful to Janna Just. Janna, I thank you so much for all the discussions and support you gave to me especially during the last month. I am very grateful to David Fischer. David, thank you for pushing me and for all the nice time we had as PhD's and as students (Geography, rocks ☺).

Many, many, many thanks goes to all my friends for their motivation and assistance during the last three years.
My personal thanks goes to my family, my parents and my sister for their encouraging support and help at any time during the last three years and even much longer and just for being there.

Last but not least, I want to give the biggest „Thank you" to Clemens Schütte. I thank you so much for everything in the last few years. I thank you for all the support during this time of my life. Thank you for tackling numerous computer problems and to settle me down after busy days and especially throughout the final stressful weeks. Without you it would have been ten times worse!!! Thank you so much!

Important abbreviations

AEJ	African Easterly Jet
AHP	African Humid Period
CHUR	Chondritic Uniform Reservoir value
EMMA	End-member modeling algorithm
Ga	Billion years before present
ITCZ	Intertropical Convergence Zone
ka	Thousand years before present
LH	Late Holocene
Ma	Million years before present
Nd	Neodymium
Rb	Rubidium
REC	Recent time period
REE	Rare earth elements
SAL	Saharan Air Layer
Sm	Samarium
Sr	Strontium
T_{BE}	Model age relative to bulk earth
T_{DM}	Model age relative to depleted mantle
YD	Younger Dryas
ε_{Nd}	Epsilon Nd, calculated based on CHUR value

1. Introduction 1

1.1 Terrigenous sediment transport and deposition off NW Africa 2
1.2 Motivation and scientific questions 3

2. Regional setting 5

2.1 Modern climate of NW Africa 5
2.2 NW African paleoclimate 7
2.3 Geological setting of NW Africa 9

3. Terrigenous sediments 11

3.1 Characterization of terrigenous sediments 11
3.2 Provenance studies 11
3.3 Material 12

4. Methods 14

4.1 Grain-size measurements 14
4.2 End-member modeling 15
4.3 Radiogenic isotopes 18
4.3.1 Sample preparation for isotopic analysis 18
4.3.2 Chemical separation and measurements of strontium 18
4.3.3 Chemical separation and measurements of neodymium 20

5. Grain-size control on Sr-Nd-isotope provenance studies and impact on paleoclimate reconstructions: an example from deep-sea sediments offshore NW Africa 22

I. Meyer, G. R. Davies and J.-B. W. Stuut
Published in *Geochemistry, Geophysics, Geosystems (G^3)*

6. Transition between prevailing climate systems in NW Africa since the Younger Dryas 41

I. Meyer, J.-B. W Stuut, C. Vogt, G. R. Davies and H. Kuhlmann

Submitted to *Aeolian Research*

7. Sensitivity of the deep-marine sediment archive offshore NW Africa to local climate changes during the Holocene 59

I. Meyer and J.-B. W. Stuut
In preparation for *Sedimentology*

8. Increase in African dust flux at the onset of commercial agriculture in the Sahel region 75

S. Mulitza, D. Heslop, D. Pittauerova, H. W. Fischer, I. Meyer,
J.-B. W. Stuut, M. Zabel, G. Mollenhauer, J. A. Collins, H. Kuhnert
and M. Schulz
Published in *Nature*

9. Conclusions 95

References 99

1. Introduction

Aeolian dust was recognized by sailors and observers since classical Greek times. The transport and deposition of desert dust has inspired historians to write peculiar and fantastic myths and stories, such as Zeus "blood rain" in Homer's *Illiad*. In addition, it was also subject of various biblical stories. One of the earliest scientific reports of aeolian dust was made by Charles Darwin in 1846, who observed a dust outbreak that fell offshore the northwest coast of Africa during one of his expeditions with the *"Beagle"*. Since then, there was increasing interest in the atmospheric transport of mineral dust and it has been subject of various scientific studies [e.g. *Carlson and Prospero*, 1972; *Chester and Johnson*, 1971; *Chiapello et al.*, 1995; *Prospero and Lamb*, 2003; *Pye*, 1987; *Rea*, 1994; *Schütz et al.*, 1981; *Swap et al.*, 1992]. Most aeolian dust is derived from the world's deserts and adjacent arid regions, which are mostly covered by sand dunes, arid soils and dried up lake beds, all of which may act as sources for insoluble, continental aerosols. Global dust emission rates are estimated to be around 1000 to 3000 $x10^6$ tons per year [*Goudie and Middleton*, 2001]. The Northern Hemisphere is one to two orders of magnitude more "dusty" than the Southern Hemisphere [*Rea*, 1994]. Presently, most aeolian dust originates from three major source areas, which are the desert regions of eastern Asia, northern Africa, and Arabia, all located in the Northern Hemisphere as shown in Fig. 1.1. Minor dust sources are found in the Southern Hemisphere, like Australia, parts of South

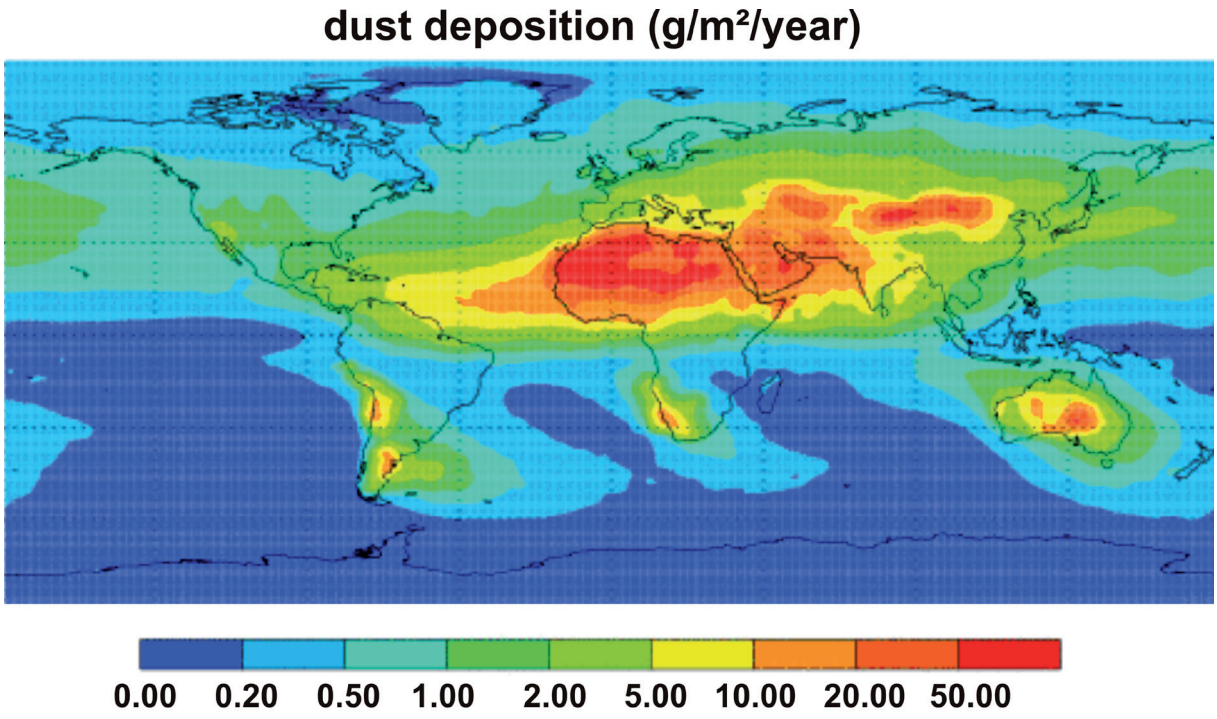

Fig.1.1 Global desert dust deposition (g/m²/year) based on different model simulations and available in situ and satellite observations. Major dust sources, mainly North Africa, the Middle East and Asia are clearly visible (modified after Mahowald, (http://geo.cornell.edu/.../mahowald/dust.htm).

America (Atacama Desert and the arid regions of Patagonia) and southern Africa (Namibian and Kalahari Desert), which contribute far less to the global dust emission.
During the past few decades airborne dust was realized to be an important environmental component, influencing the radiative balance in the atmosphere, and the albedo [e.g. *Harrison et al.*, 2001; *Miller and Tegen*, 1999; *Ramanathan et al.*, 2001], weather phenomena, like cyclone activity [*Evan et al.*, 2006; *Sun et al.*, 2008], marine and terrestrial ecosystems [*Jickells et al.*, 2005; *Okin et al.*, 2004], all with large consequences for future climate change in many regions of the world [*Prospero and Lamb*, 2003; *Tegen et al.*, 2004].

1.1. Terrigenous sediment transport and deposition off NW Africa

At present the Saharan Desert is one of the most arid places in the world and therefore the most important source of mineral dust supplied to the Atlantic Ocean [*Harrison et al.*, 2001]. The modern dust production rate of the Sahara is estimated to be around 700-900 x 10^6 tons aeolian dust per year [*Goudie and Middleton*, 2006]. And since around 70% of the global dust emission is deposited into the world's oceans [*Goudie and Middleton*, 2001; *Jickells et al.*, 2005; *Mahowald et al.*, 2005], Saharan dust is one of the most dominant components in marine sediments of the tropical north-east Atlantic Ocean.
Saharan dust has been observed to travel over enormous distances across the Atlantic Ocean and was identified on the Bahamas [e.g. *Ott et al.*, 1991], in South America [*Prospero et al.*, 1981], in Florida and on Barbados [*Glaccum and Prospero*, 1980; *Muhs et al*., 1990]. Saharan dust also travels towards the Mediterranean and sometimes up to northern Europe [*Franzén*, 1989; *Stuut et al.*, 2009]. Additionally, Saharan dust is transported eastward to the Middle East and even as far as China [*Tanaka et al.*, 2005].
Based on satellite images such as the Total Ozone Mapping Spectrometer (TOMS) three major dust source areas can be identified within Northern Africa (see Fig.1.2.) : I) the Bodélé Depression in Chad, which is by far the most important dust source area not only in the Saharan Desert, but also in the world [*Giles*, 2005; *McTainsh*, 1984], II) The West Saharan region, spanning the northern border of Mali and Mauritania, and, III) the Chotts, a series of temporary and salty lakes, in eastern Algeria and Tunisia. Other minor dust source regions are located south of the northern Atlas Mountains and the Nubian Desert (Egypt and Sudan) [*Goudie and Middleton*, 2006].
Next to the aeolian input, terrigenous sediments are supplied by rivers into the Atlantic Ocean. Globally, the fluvial sediment supply to the oceans exceeds the aeolian transport by a factor of ten; the global river discharge of sediments is estimated to be ~ 20 x 10^{12} tons per year [*Milliman and Syvitski*, 1992]. On the contrary, the total discharge of suspended sediment by NW African rivers into the Atlantic Ocean is estimated to be ~ 110 × 10^6 tons/year in modern times, which represents a factor ten less than the aeolian dust supply in the area [*Milliman and*

Meade, 1983]. The fluvial input within the study area is restricted to river systems in Morocco, like the Sebou or the Souss Rivers, draining the Atlas Mountains year-round but with highest intensities during boreal winter [*Summerhayes et al.*, 1976; *Wynn et al.*, 2002]. The Senegal River is by far the biggest source of fluvial material within the study area. The drainage basin of the Senegal River covers ~ 343.000 km². However, *Gac and Kane* [1986] estimated the sediment load of the Senegal River delivered to the Atlantic Ocean to be ~ 2 x 10^6 tons per year. South of ~29°N the fluvial supply is limited, here mainly smaller river systems and Wadis reach the Atlantic only seasonally [*e.g. Wynn et al.*, 2002].

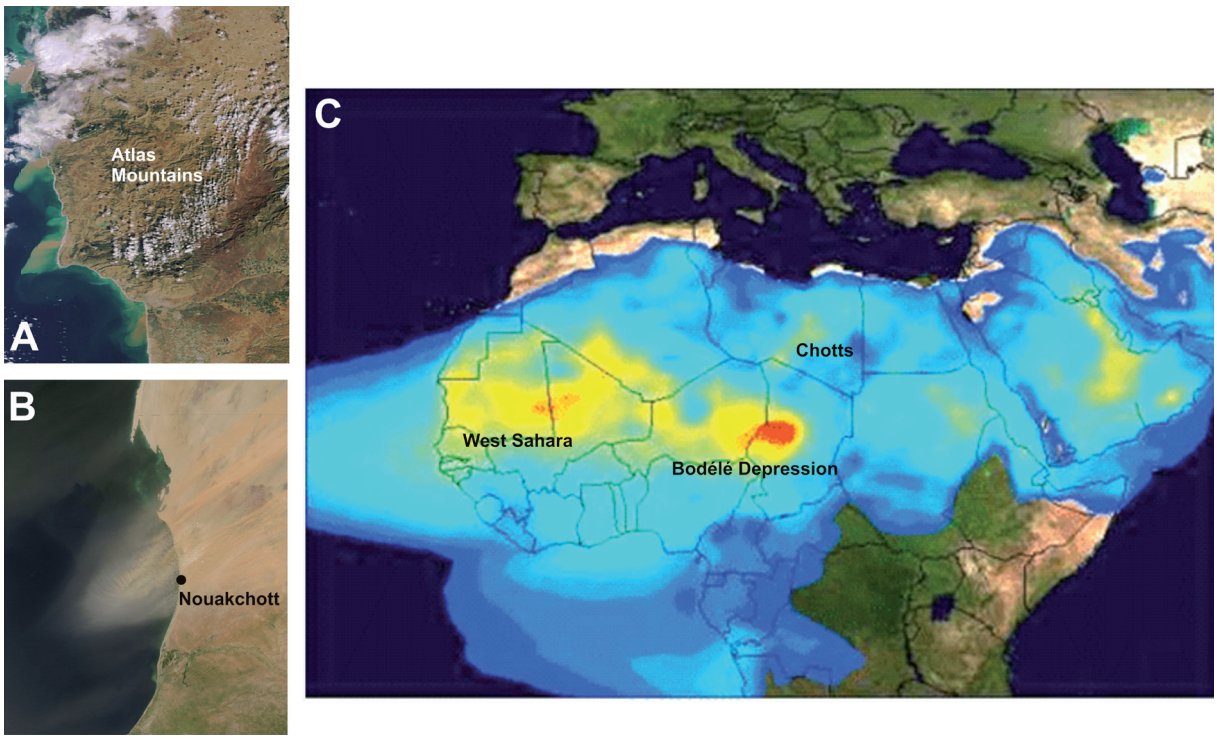

Fig.1.2 Terrigenous sediments off NW Africa are delivered by two different transport mechanisms to the Atlantic Ocean. In A) the Souss River spills sediments transported from the Atlas Mountains into the Atlantic Ocean near Agadir. B) demonstrates aeolian dust emission near Nouakchott, the capital of Mauritania. In C) dust sources obtained from Total Ozone Mapping Spectrometer (TOMS) are shown. The major sources regions, the Bodélé Depression and the Mali/Mauritania region, are clearly visible (http://earthobservatory.nasa.gov/).

1.2. Motivation and scientific questions

In order to improve our predictions of future climate, a better understanding of the coupled continent-ocean dynamics and their role in global heat and moisture transport is essential. Deep-sea sediments are known to form a natural high-resolution archive of past climate variability provided by the land-derived sediments accumulating on the seafloor [*deMenocal et al.*, 2000a; *Rea et al.*, 1985; 1994; *Sarnthein et al.*, 1981; *Tjallingii et al.*, 2008]. An investigation of the sediments downwind of the major desert areas, like the Saharan Desert, allows distinct

fingerprints of land-sea connections through variations of terrigenous input (aeolian dust versus fluvial mud) from the NW African continent and offers excellent opportunities to study continental humidity and aridity, and the variability of the atmospheric circulation as linked to global climate change.

Previous studies of NW African climate have mainly focussed on the long-term climate variations, especially on glacial and interglacial timescales [*Itambi et al.*, 2009; *Jullien et al.*, 2007; *Mulitza et al.*, 2008; *Tjallingii et al.*, 2008]. So far, relatively little is known about short-term (decadal to millennial scale) wet-dry variations within these presently dry regions on the African continent. And although NW African climate was relatively stable during the Holocene (~11.7 ka to present) several climatic shifts, like the Younger Dryas or the African Humid Period have occurred during the last millennia, leading to several new scientific questions that form the basis of this thesis.

The aim of this PhD thesis is to study the impact and characteristics of variability within the prevailing climate systems in NW Africa during the Holocene. The combined investigation of grain-size distributions, end-member modeling and the analysis of strontium and neodymium isotopes enables conclusions about the climatic and hydrological history of NW Africa since the Younger Dryas.

Major scientific questions are:

- ► Is the investigation of terrigenous material found in marine sediment cores a reliable source of information to reconstruct paleoclimatic changes on decadal to millennial scale?
- ► How do the terrigenous sediment supply and its distribution vary during the Holocene on a spatial and temporal scale?
- ► How do the atmospheric circulation and the prevailing climate regimes vary during the Holocene?
- ► Is it possible to identify and quantify the source areas, using the terrigenous fraction?
- ► How do source regions of land-derived material vary due to changes in the atmospheric circulation?
- ► Is it possible to reconstruct the hydrological evolution within NW Africa by using isotopic fingerprinting?
- ► To what extend do human activities influence the dust emission within the area?

2. Regional setting

2.1. Modern climate of NW Africa

The global atmospheric circulation (shown in Fig. 2.1.) consists of a sequence of low-level wind systems and cellular pressure belts spanning the globe [*e.g. Lutgens and Tarbuck*, 2001; *Nicholson and Flohn*, 1980]. A zone of high pressure is located at both poles. At ~60°N and ~60°S the sub-polar low-pressure belts with cyclonic activity dominate, generating easterly winds between the poles and the low-pressure belts (Polar Cell). Between 60° and 30° North and South there are the Mid-Latitude Cells, where strong westerly winds prevail. On both hemispheres a subtropical high-pressure belt is located at around 30°N and 30°S, between the Westerlies and the zone of trade winds with an easterly direction (Hadley Cell). Both trade winds converge in the low-pressure zone of the Intertropical Convergence Zone (ITCZ), which is the main driver of NW African climate. The ITCZ over NW Africa shows a seasonal

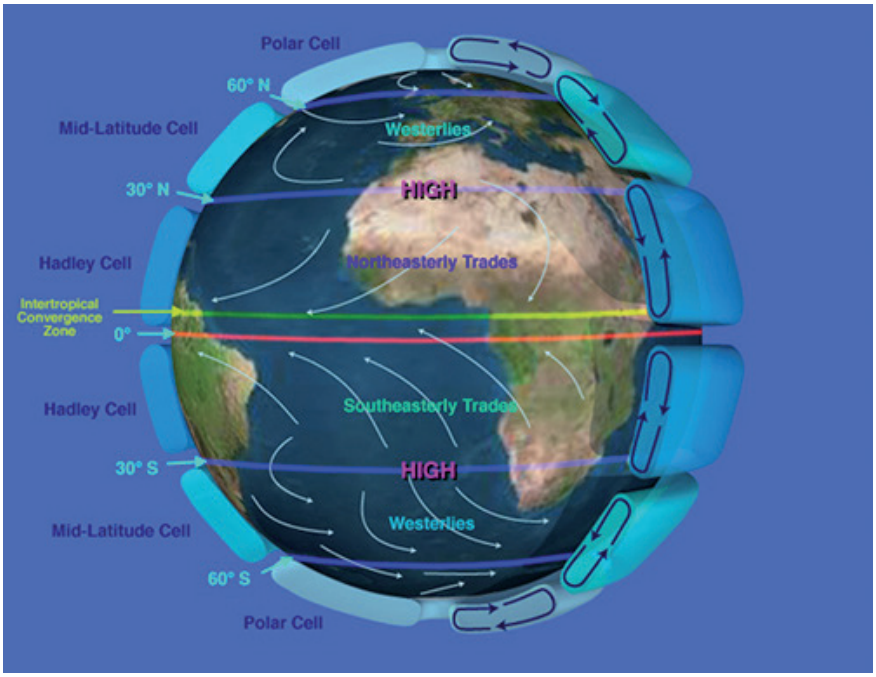

Fig.2.1 Global atmospheric circulation, with three cells on both hemispheres. The deflection of the cells is caused by the Coriolis Force in opposite directions on both hemispheres. Present day wind patterns are generated by pressure gradients and the Coriolis Force, again in opposite directions on both hemispheres [*Lutgens and Tarbuck*, 2001]. Due to the large amount of land mass on the Northern Hemisphere, relative to the Southern Hemisphere, the ITCZ is located north of the equator.

variability with 5°N during boreal winter and 20°N during boreal summer, following the seasonal migration of maximum insolation [*Nicholson*, 2000]. During boreal winter (see also Fig, 2.2) the ITCZ is in its most southerly position and the dry north-eastern trade winds penetrate far into NW Africa. Conversely, during boreal summer the ITCZ is located further

north, diminishing the influence of the trade winds [*Ruddiman*, 2001]. As a consequence, the influence of the humid south-eastern monsoonal flow, located south of the ITCZ, dominates over the region and leads to an increase in precipitation [*Knippertz et al.*, 2003].

In contrast, the northernmost part of the continent, e.g. northern Morocco, is under the influence of the Mediterranean climate system. During the summer this climate is controlled by a high-pressure cell located over the Azores, causing hot and dry conditions. During boreal winter, when all circulation features are displaced to the south, the region is influenced by a westerly flow in the upper atmosphere [*e.g. Nicholson*, 2000], which causes winter rain due to the migration of cyclones [*Nicholson and Flohn*, 1980].

Dust is transported from the NW African interior to the Atlantic Ocean by two prevailing wind systems. In the north-west, the shallow north-eastern (NE) trade-wind layer, including the Harmattan wind system (500 to 1500 m height), transports dust from the Atlas Mountains and coastal plains in south-western direction parallel to the coast [*Sarnthein et al.*, 1981]. The cool and dry trade winds carry dust to the proximal parts of the Atlantic Ocean year-round, but with highest intensities during boreal winter and spring [*Stuut et al.*, 2005]. During boreal winter the atmospheric circulation above the trade-wind layer is dominated by the westerly flow of extratropical air masses [*e.g., Nicholson*, 2000 and see Fig. 2.2]. The influence of the NE trade winds extends from the NW African coast to the Canary and Cape Verde Islands [*e.g. Pye*, 1987]. Dust from the southern Sahara and the bordering Sahel zone is transported directly westward with the higher Saharan Air Layer (SAL), coupled to the mid-tropospheric African Easterly Jet (AEJ) (1000 to 5000 m high) mainly during boreal summer [*Koopmann*, 1981; *Pye*, 1987; *Sarnthein et al.*, 1982]. This easterly flow is made up by a series of tropical turbulences ("easterly waves") that supply energy for the growth and stability of rain-bearing disturbances [*Nicholson*, 2000; *Reed et al*., 1977]. The seasonality of the dust-laden wind systems results in two dust plume mechanisms. During winter the main dust plume is centered between 5°N and 20°N associated with the southerly position of the ITZC and with prevailing easterly SAL [*deMenocal and Rind*, 1993; *Stuut et al.*, 2005]. The summer dust is mainly delivered from the western and central Sahara by the northeastern trade winds resulting in a dust plume at ~ 10-30°N.

Modern vegetation zones of NW Africa respond to the climatic conditions and thus occur in zonal belts almost parallel to the ITCZ [*e.g. Castañeda et al.*, 2009]. The tropical rainforest is restricted to areas with high amounts of precipitation near the core of the ITCZ. To the north, vegetation is progressively adapted to more arid conditions, as shown by the presence of grass- and tree savanna [*e.g. Ruddiman*, 2001]. The transition to the sparsely vegetated desert is covered by grasses and shrubs. North of the Saharan Desert the Mediterranean evergreen forest dominates.

2.2. NW African paleoclimate

The geological epoch Holocene started approximately 12 thousand years before present (hereafter ka) and continues to the present. The Holocene climate is fairly stable compared to the abundant glacial-interglacial changes during the Pleistocene [*Dansgaard et al.*, 1993]. However, several proxy- and model-based records provide evidence that the Holocene climate was much more unstable than commonly anticipated and exhibits variability on (sub-) millennial time scales [*Bond et al.*, 2001; *Schulz and Paul*, 2002].

The end of the Pleistocene (~ 12 ka), which is characterized by a gradual return from glacial to interglacial conditions is marked by a pronounced cold period, called the Younger Dryas (hereafter YD), between approximately 12.8 to 11.5 ka [*Muscheler et al.*, 2008]. The YD, which is known as a period of changing thermohaline circulation is well documented in the North Atlantic realm [*e.g. Mayewski et al.*, 1993] and recent work has established the YD as a Northern Hemisphere event [*e.g. Broecker*, 2006; *Hughen et al.*, 1996]. Evidence for a climate change in NW Africa during the YD is also widespread. *Marret and Turon* [1994] analyzed a marine sediment core offshore Morocco and found a different pollen content and a higher amount of dinoflagellate cysts during the YD, indicating a change in the atmospheric circulation and stronger NE trade winds. Furthermore, changes in some pollen species indicate a shift to cooler conditions during the YD [*Marret and Turon*, 1994]. Similar results were found in lake-level reconstructions and sediment cores from lakes in Western Sahara, the Sahel, and subequatorial Africa [*Gasse and Van Campo*, 1994; *Gasse et al.*, 1990]. In addition, proxy investigations suggest a more southerly position of the African rainbelt during glacial times [*Nicholson*, 1982] and a weaker monsoon during the YD [*Hong et al.*, 2003]. Fig. 2.2. shows the prevailing atmospheric circulation patterns over NW Africa for I) glacial conditions (left panel), II) for an interglacial environment (middle panel), III) recent times (right panel), and during boreal winter (upper part) and boreal summer (lower part).

After the termination of the YD, increased summer insolation and therefore an intensified monsoon circulation linked to a northward shift of the northern limit of the African rainbelt over NW Africa caused more humid conditions and resulted in an increased vegetation cover [*Gasse*, 2000; *Nicholson and Flohn*, 1980; *Tjallingii et al*., 2008; Fig. 2.2., middle panel]. This humid epoch between approximately 9 ka and 5 ka is called the African Humid Period [hereafter AHP; e.g. *deMenocal et al.*, 2000a]. Evidence for a shift towards wetter conditions during the early- and mid-Holocene was found in numerous geological, palynological, and hydrological records from the southern Sahara, the Sahel and the Soudan, Senegal and Mauritania [*Fontes and Gasse*, 1991; *Gasse et al.*, 1990; *Gasse*, 2002; *Hillaire-Marcel et al.*, 1983; *Hoelzmann et al.*, 2004]. The presently hyperarid Sahara was covered with denser and more diverse vegetation, which was caused by a northward shift of southern vegetation types [*Kuper and Kröpelin*, 2006; *Salzmann*, 2000] as well as an expansion of different forest types [*Lézine and Casanova*, 1989; S*alzmann and Waller*, 1998]. The northern boundary

of the monsoonal rainbelt shifted ~ 700 km northward [*Haynes*, 1987; *Neumann*, 1993]. As a consequence of this increased precipitation several lakes occurred in the area [*Drake and Bristow*, 2006; *Gasse*, 2000; *Hoelzmann et al.*, 2000; *Nicholson and Flohn*, 1980].

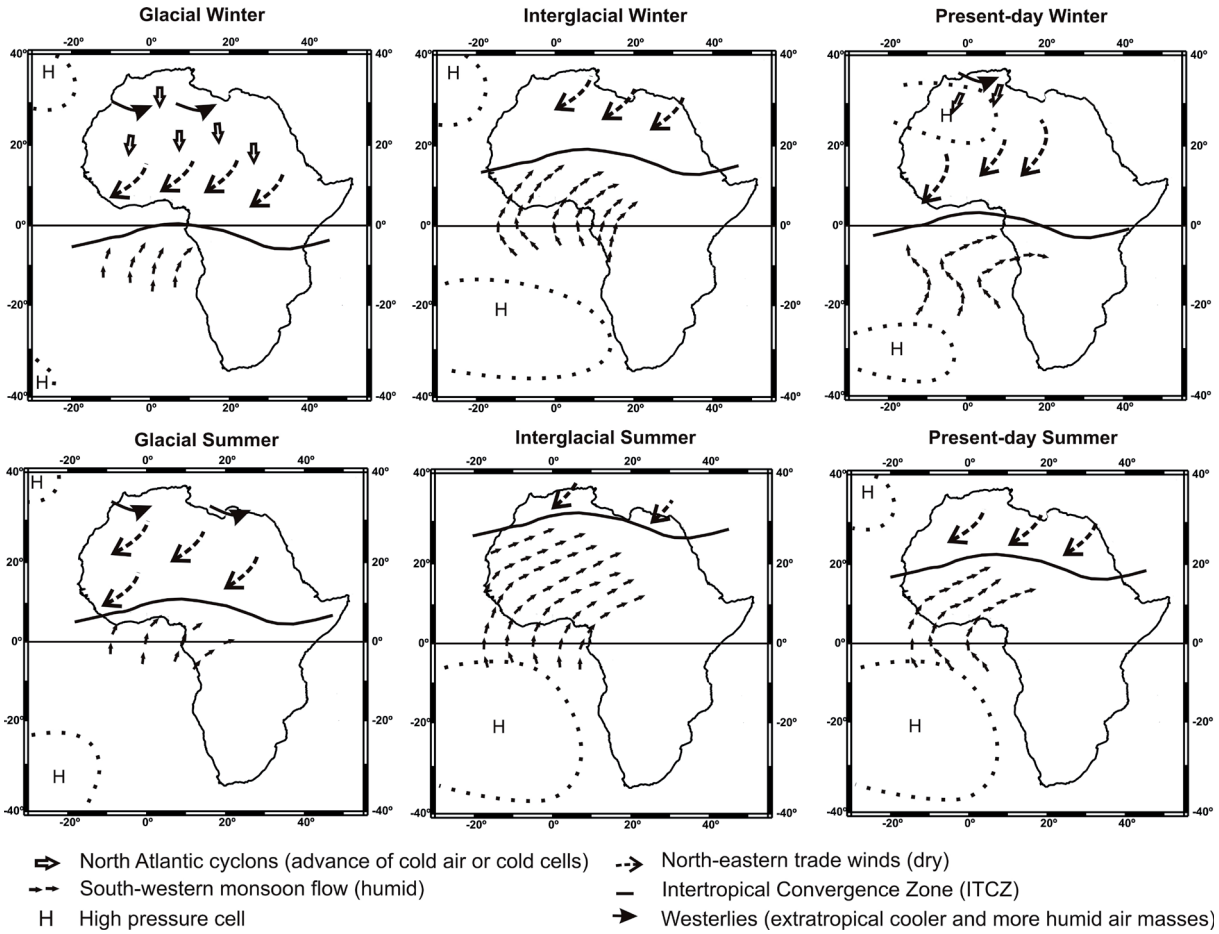

Fig. 2.2 Illustration of the general atmospheric circulation patterns over NW Africa for I) glacial conditions (left), II) for an interglacial environment (middle), and III) for recent times during boreal winter (upper part) and boreal summer conditions (lower part) (modified from *Messerli and Winiger*, [1992], *and Nicholson*, [2000]).

Wadis and coastal streams in western Mauritania drained to the ocean and breached the Pleistocene dunes between Nouakchott and Cape Verde [*Nicholson and Flohn*, 1980]. A huge palaeo-river system, the Tamanrasett River system, is assumed to have drained the Mauritanian interior during such moist conditions [*Zühlsdorff et al.*, 2007]. Kutzbach and Street-Perrott [1985] used an general atmospheric circulation model to simulate the amount of precipitation over the Sahel at 9 ka and found 25-30% higher values compared to modern times. *Renssen et al.* [2006] simulated the climatic evolution in subtropical North Africa using a coupled atmosphere-ocean-vegetation model. In agreement with numerous proxy data they found evidence for a more humid period contemporaneous with the AHP. Furthermore, archaeological

studies evidence prospering human communities and settlements during the mid-Holocene [*McIntosh and Tainter*, 2000; *McIntosh and McIntosh*, 1983]. However, the abruptness of the start and end of the AHP is still a matter of debate. While some studies support the theory of an abrupt start and end of the AHP [*e.g. Cole et al.*, 2009; *deMenocal et al.*, 2000a] other studies argue for a more gradual transition [*Kröpelin et al.*, 2008].

Regardless how abrupt, since the mid Holocene, from ~ 5 ka on, a transition from humid to more arid conditions was observed throughout NW Africa. The modern atmospheric conditions of NW Africa are indicated in Fig. 2.2., right panel. Based on a drop in lake levels, several lacustrine investigations examine an aridification since the mid-Holocene throughout the Sahara and the Sahel [*Gasse and Van Campo*, 1994; *Pachur and Kröpelin*, 1987; *Pachur and Hoelzmann*, 2000]. A distinct change in vegetation towards drier conditions was found at several NW African sites. Pollen data point to an establishment of desert-like conditions around 5.7 - 4.5 ka [*e.g. Lézine*, 1989]. In marine sediment cores offshore the West African continent an increase in dust deposits can be found since 5.5 ka, pointing to drier conditions [*Adkins et al.*, 2006; *deMenocal et al.*, 2000a]. An investigation of the atmospheric patterns over NW Africa indicates a gradual decrease in African monsoon strength during late Holocene times [*Hong et al.*, 2003]. These proxy-based investigations are consistent with climate-modeling studies [*e.g., Renssen et al.*, 2006].

2. 3. Geological setting of NW Africa

Most of the NW African basement belongs to the West African Craton extending from the Anti-Atlas Mountains in the north to the Gulf of Guinea in the south (Fig. 2.3). The West African Craton mainly consists of late Archaean and early to mid- Proterozoic crystalline basement rocks (~ 2.0 Ga) comprising metamorphic rocks and granites, pyroxenites and quartzites [*Lecorche et al.*, 1991]. The oldest rocks are at least 3.5-3.6 Ga and are exposed in the southwestern part of the Reguibat shield and the Leo shield [*Potrel et al.*, 1996]. The Craton is encircled by more recent mobile belts mainly of Pan-African age [~500 Ma; *Körner and Stern*, 2004]. Since lower to mid Proterozoic times (~ 1.7 Ga) the Craton is geologically stable [*Dallmeyer and Lecorche*, 1991]. More than half of the Craton is covered by mid to late Proterozoic to Devonian sediments and metasediments [*Dallmeyer and Lecorche*, 1991; *Wright et al.*, 1985]. The sediments are of marine and terrestrial (fluvial and lacustrine) origin and record sea-level changes over the shallow relief of the NW coastal area [*Wright et al.*, 1985]. The West African Craton is bounded by the Atlas Mountains in the NNW (Morocco, Algeria and Tunisia), that were formed much later during several phases of Earth‘s history, starting ~ 3.0 Ga [*e.g. Ennih and Liegeois*, 2008]. The last period of tectonic deformation occurred during the late Cretaceous-Cenozoic (~ 65 Ma) when Africa and Eurasia collided associated with the formation of the European Alps [*Wright et al.*, 1985]. Parts of the Atlas Mountain are still tectonically and volcanically active [*Ramdani*, 1998]. Another geological feature in the study area is the Canary Archipelago around 600 km

off the African coast.The Canary Archipelago (27°N to 29°N and 13 to 19° W) is a group of seven major young volcanic islands, underlain by several presently active melting areas [*Schmincke*, 2000]. The islands are mainly developed during Miocene and Pliocene times [*Schmincke*, 2000]. The age of the volcanic islands decreases from east to west, with Fuerteventura having the oldest rocks (22 Ma) and El Hierro the youngest rocks [1.2 Ma; *Schmincke*, 2000]. Volcanic eruptions occurred on all islands within the last 5000 years except for La Gomera [*Schmincke*, 1982].

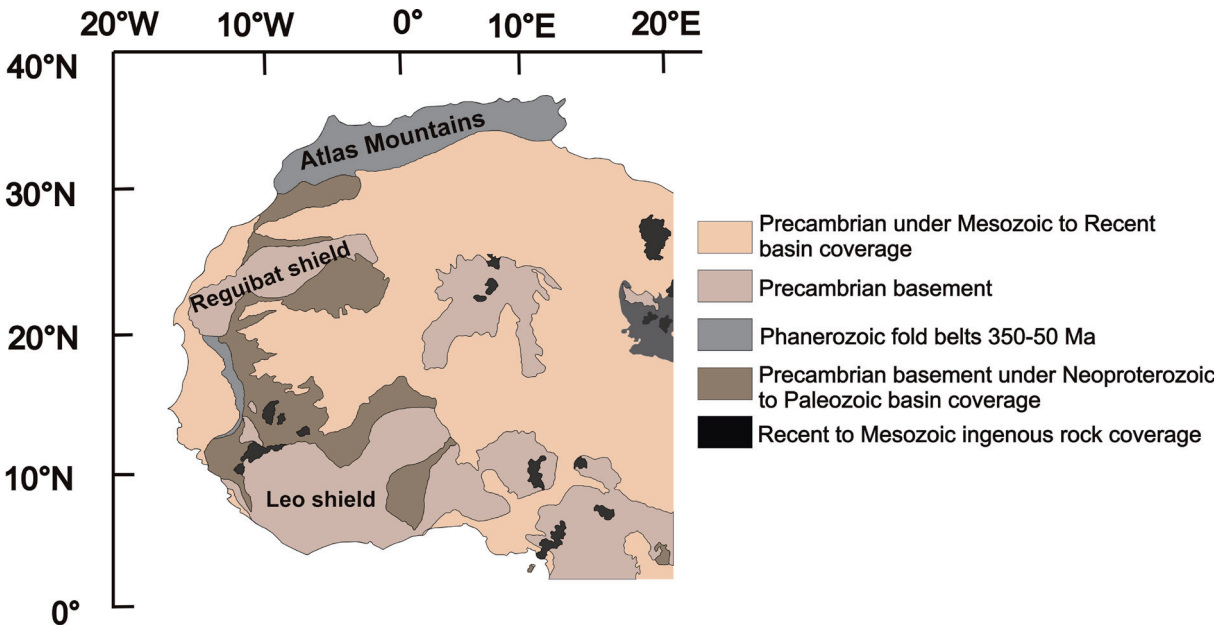

Fig. 2.3 Geological map of NW Africa (modified from *Trauth and Schlüter* [2006]). Most parts of NW Africa are built up of Archean and Precambrian crystalline basement rocks.

3. Terrigenous sediments

3.1. Characterization of terrigenous sediments

The terrigenous fraction preserved in deep-sea sediment cores from continental margins of NW Africa forms an excellent archive of changes in past atmospheric circulation and continental paleoclimate [*deMenocal et al.*, 2000b; *Rea et al.*, 1985; *Sarnthein et al.*, 1981; *Tjallingii et al.*, 2008]. Since the last decades, several methods have been developed to deduce the provenance and transport mechanisms of terrigenous components, like e.g., the investigation of clay minerals [*Biscaye*, 1965; *Biscaye et al.*, 1997; *Caquineau et al.*, 2002]; bulk chemistry [*Moreno et al.*, 2006; *Zabel et al.*, 1999; 2001] or atmospheric back-trajectory models [*Goudie and Middleton*, 2001; *Stuut et al.*, 2005].

In addition, analysis of the grain-size distribution and end-member modeling of terrigenous sediments can be used to detect the different transport mechanisms, which are directly related to the dominant climate conditions prevailing on the continent [e.g. *Prins and Weltje*, 1999; *Stuut et al.*, 2002]. As already mentioned, offshore the NW African coast the main transport mechanisms of terrigenous material are aeolian and fluvial. The particle size of wind-blown dust is a function of the distance from source to sink and altitude at which the particles are transported [*Stuut et al.*, 2005; *Weltje and Prins*, 2003]. Aeolian dust deposited near the coast is generally coarser than distal material [*Holz et al.*, 2004; *Sarnthein and Koopmann*, 1980]. Proximal dust samples from the Cape Verde Islands, 460 km offshore the NW African coast, contain particles up to 90 μm in diameter [*Glaccum and Prospero*, 1980]. *Stuut et al* [2005] detected particle sizes generally larger than 10 μm in present-day dust samples collected off Senegal and Mauritania. Conversely, distal dust reaching the Caribbean is less than 5 μm in size [*Talbot et al.*, 1986], also dust collected at higher altitudes has similar fine particle sizes [*Torres-Padrón et al.*, 2002].

Terrigenous material transported by rivers is much finer in size than proximal aeolian particles. Grain-size measurements of marine sediments offshore several rivers were found to be smaller than 10 μm [*Weltje and Prins*, 2007]. Similar results were obtained by *Gac and Kane* [1986]. They detected 95% of the fluvial sediment supplied by the Senegal River to be smaller than 10 μm.

3.2. Provenance studies

Although grain-size distributions and end-member modeling can reflect different transport mechanisms, they are unlikely to be more revealing of the geological source area of the terrigenous material. Therefore, in this PhD project, isotopic ratios of strontium (Sr) and neodymium (Nd) of the terrigenous sediment fractions were used to establish their provenance, as they were shown to be valuable indicators to identify and quantify source areas of terrigenous matter (Nd) as well as to reconstruct the hydrological evolution of the source region (Sr) [e.g.

Borg and Banner, 1996; *Capo et al.*, 1998; Cole et al., 2009; *Colin et al.*, 2006; *Grousset et al.*, 1998; *Grousset and Biscaye*, 2005; *Jung et al.*, 2004; *Rutberg et al.*, 2005].

Strontium (atomic number 38) is an alkali earth element, which is incorporated in minerals or rocks, like feldspars and plagioclases. Strontium (Sr) has four naturally occurring isotopes ^{84}Sr, ^{86}Sr, ^{87}Sr, and ^{88}Sr, which are all stable. However, ^{87}Sr is produced by the radioactive decay of rubidium (^{87}Rb) with a half-life of ~ 48.8 x 10^9 years [*Frank*, 2002]. Therefore, the amount of ^{87}Sr increases over geological time whereas the amounts of ^{84}Sr, ^{86}Sr and ^{88}Sr remain constant [*Faure and Powell*, 1972]. Rb and Sr were often used for dating Rb-bearing rocks and minerals and for studying the formation and age of igneous rocks [*Compston et al.*, 1965; *Faure*, 1986]. However, several studies suggest that tectonic activity and hydrological changes can strongly affect the amount and isotopic composition of Sr since ^{87}Sr in rocks is easily released by weathering [*Capo et al.*, 1998; *Colin et al.*, 2006; *Jung et al.*, 2004]. Therefore, changes in the intensity of weathering processes as well as the type of rocks subject to weathering have an influence on the Sr isotopic compositions [*Capo et al.*, 1998; *Edmond*, 1992].

Neodymium (atomic number 60) belongs to the rare earth elements (REE) and appears only in small amounts in most minerals or rocks [*DePaolo*, 1988]. Naturally occurring neodymium (Nd) has seven isotopes, which are ^{142}Nd, ^{143}Nd, ^{144}Nd, ^{145}Nd and ^{146}Nd, ^{148}Nd and ^{150}Nd. Variations between ^{143}Nd (produced by the radioactive decay of samarium (^{147}Sm), with a half-life of ~ 106 Ga) and ^{144}Nd (not formed by radioactive decay and constant over time) has shown to be a powerful tool to study the provenance of silicate detritus in marine sediment cores [e.g. *Cullen et al.*, 2000; *Grousset et al.*, 1998; *Grousset and Biscaye*, 2005; *Jullien et al.*, 2007; *Jung et al.*, 2004; *Nakai et al.*, 1993; *Rutberg et al.*, 2005; *Weldeab et al.*, 2002]. The isotopic composition of Nd is significantly different in mantle- vs. crust-derived rocks, permitting the distinction between these two extreme origins and of lithologies in between: young volcanic areas and old continental crusts [*DePaolo*, 1988]. An advantage of using Nd isotopes for provenance studies relative to using Sr ratios is that the rare earth elements are less mobile and therefore not fractionated during near-surface conditions, such as chemical weathering [*DePaolo*, 1988].

3.3. Material

Deep-sea sediment cores offshore major deserts can provide continuous records of paleoenvironmental conditions on land. This study was carried out using eight undisturbed deep-sea sediment cores from the continental margin of NW Africa, between 15°N and 30°N.

Grain-size measurements and end-member modeling were carried out on all marine sediment cores during this thesis. In addition isotopic analyses were done on seven of them. Exact positions and further details of the deep-sea sediment cores are provided in Table 1.

Table 1 Core locations and age model references

Core	Longitude (°W)	Latitude (°N)	Water depth (m)	Sampling resolution (cm)	Location	References Age models
GeoB 6007-2	10°16 W	30°51 N	-900	2	off Cape Ghir	[*Kuhlmann et al.,* 2004a]
GeoB 4223-2	12°28 W	29°01 N	-775	1	Agadir Canyon	[*Freudenthal et al.*, 2002]
GeoB 7430-3	15°09 W	26°22 N	-1165	1	off Cape Bojador	[*Kuhlmann,* unpubl.data]
GIK 12379-1	18°75 W	23°14 N	-2136	1	off Cape Barbas	[*Sarnthein et al.,* 1994]
GeoB 7920-2	18°34 W	20°45 N	-2278	5	off Cape Blanc	[*Tjallingii et al.,* 2008]
GIK 13588-3	17°15 W	19°38 N	-1000	1	off Banc d'Arguin	[*Diester-Haaß,* 1981]
GeoB 9501-4	16°44 W	16°50 N	-330	2	Mauritania Canyon	[*Mulitza et al.,* 2010]
GeoB 9508-5	17°57 W	15°30 N	-2384	5	off Senegal	[*Mulitza et al.,* 2008]

Additionally, several present-day atmospheric dust samples, collected during *R/V Meteor* cruise M41/1 were analyzed for grain-size distributions and strontium isotopes. Exact positions and further details of the atmospheric dust samples can be found in Table 2.

Table 2 Position of dust filter samples

Dust filter	Start	End	Location	Cruise	Reference
D1	24°55′75′′N/ 16°53′12′′ W	20°16′47′′ N/ 17°55′08′′ W	off Morocco	M41/1	[*Schulz and cruise participants*, 1998]
D2	20°11′72′′ N/ 17°54′91′′ W	19°16′40′′ N/ 17°54′80′′ W	off Mauritania	M41/1	
D3	16°22′72′′ N/ 17°54′95′′ W	15°37′01′′ N/ 17°54′93′′ W	off Mauritania	M41/1	
D4	14°57′11′′ N/ 17°55′16′′ W	14°26′28′′ N/ 17°55′08′′ W	off Senegal	M41/1	

4. Methods

All pre-treatments and grain-size measurements were carried out in the grain-size lab at the MARUM, Center for Marine Environmental Sciences, at the University of Bremen (run by Dr. Jan-Berend W. Stuut and Inka Meyer). Sample preparations for isotopic analysis and isotopic measurements were performed at the Vrije Universiteit (VU), Amsterdam. Since the chemical processing prior to isotopic analyses requires a very clean environment, laboratories for radiogenic isotope geochemistry at the VU Amsterdam consist of two parts: 1) the clean lab for sample preparation and chemical separation (run by Richard Smeets), and 2) the thermal ionization mass spectrometer lab (run by Prof. Gareth Davies).

4.1. Grain-size measurements

Since grain-size measurements were carried out only on the terrigenous sediment fraction, all biogenic components were removed before digestion. To remove the organic material, 10 ml of H_2O_2 (35%) was added to about 300 mg of sediment sample, suspended in about 25 ml demineralised water and boiled until the reaction stopped. In a second step, samples were boiled for one minute with 10 ml of HCl (10%) to remove calcium carbonate ($CaCO_3$) in e.g., tests of coccolithophorids, planktonic and benthic foraminifers. To dissolve the biogenic silica that is present in e.g., algal remains, diatoms, and radiolarids, the samples were treated with 6g NaOH pellets and boiled for 10 minutes. After these treatments the samples were diluted with demineralised water until a neutral pH was established. The samples were finally boiled with 300 mg tetra-Natriumdiphosphate-Decahydrate ($Na_4P_2O_2$ x 10 H_2O) in order to disperse remaining aggregates. Grain-size distributions were determined using the Laser Diffraction Particle Size Analyzer (Beckman Coulter) LS200, resulting in volume percentages of 92 size classes from 0.4 to 2000 µm. The method allows a fast operation with a high reproducibility. Fig. 4.1. shows a schematic sketch of the Beckman Coulter LS200. The LS200 is composed of four major elements: I) the light source that generates a monochromatic laser beam (750 nm), II) two types of lenses to keep the laser beam at a constant intensity and to focus the beam III) the sample cell, where the sample solution is pumped through the laser beam and IV) the detector array to collect the signal of laser light that was dispersed by the particles. During the measurement, the sample suspension is continuously pumped through the system and thus passes the laser beam. The particles scatter the laser light and generate unique angular scattering patterns. Small particles will deflect the beam much stronger than larger particles. A processing software (based on Fraunhofer scattering theory) converts the set of diffraction diagrams into a particle size distribution. Hence, results are obtained directly in a digital format and can be processed easily. Furthermore, several moment statistics, including mean and median grain size, standard deviation, skewness, and kurtosis are directly calculated by the software.

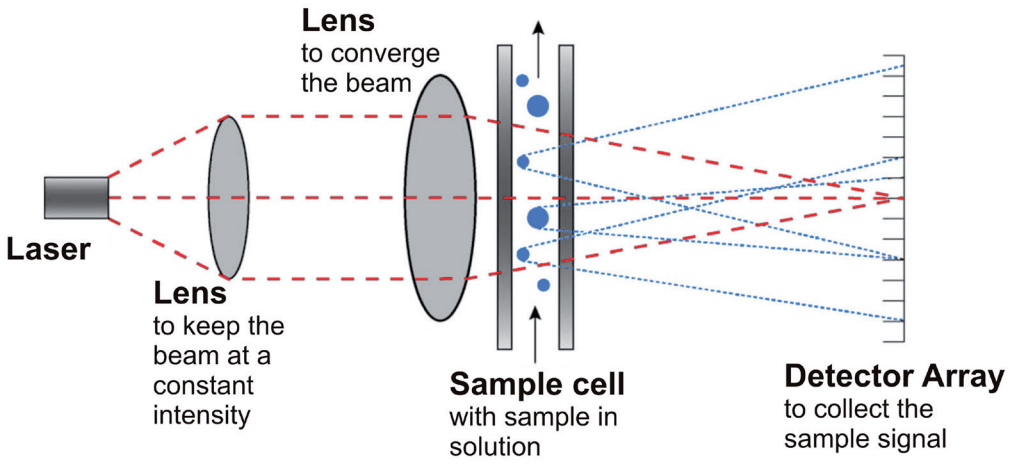

Figure 4.1 Schematic of the Laser Diffraction Particle Size Analyzer LS200. Major components are the laser beam (750nm), two types of lenses, the sample cell (where the sample solution is pumped through the laser beam) and the detector array to collect the signal of laser light that was dispersed by the particles (modified after *Pye and Blott* [2004]).

4.2. End-member modeling

The terrigenous fraction deposited in marine sediments consists of a mixture of sediment populations supplied from various sources and transported by different transport mechanisms [*e.g. Weltje and Prins*, 2003]. This results in bi-or even polymodal grain-size distributions, which are hard to interpret in terms of sediment transport mechanisms or paleoclimatic reconstructions.

The mathematical-statistical end-member modeling algorithm EMMA [*Weltje*, 1997] was applied in order to define the different sub-populations of terrigenous sediments [e.g., *Prins and Weltje*, 1999; *Stuut et al.*, 2002; *Weltje and Prins*, 2007]. The method aims at the construction of a physical mixing model that expresses the observations as mixtures of a limited number of end members with real grain-size distributions. In the following, measured grain-size data of core GeoB 9508-5 are used to explain the end-member algorithm EMMA and to show how the end members are calculated from a set of grain-size distributions. Sediment core GeoB 9508-5 was recovered from the continental slope off Senegal at 15°N and 17°W from 2384 m water depth. Age determination based on planktonic foraminifers gave a maximum age of 57.210 ka [*Mulitza et al.*, 2008].

Grain-size distributions of GeoB 9508-5 show a clear bimodal character with modes at ~8 and ~55 µm (Fig. 4.2). 190 samples were used to calculate the dominant end members. Summary statistics for the mean size distribution as well as the minimum and maximum range of frequency were calculated for each grain-size class (Fig. 4.3a). The coefficient of determination (r^2) is calculated to identify the minimal numbers of end members necessary for a good statistical

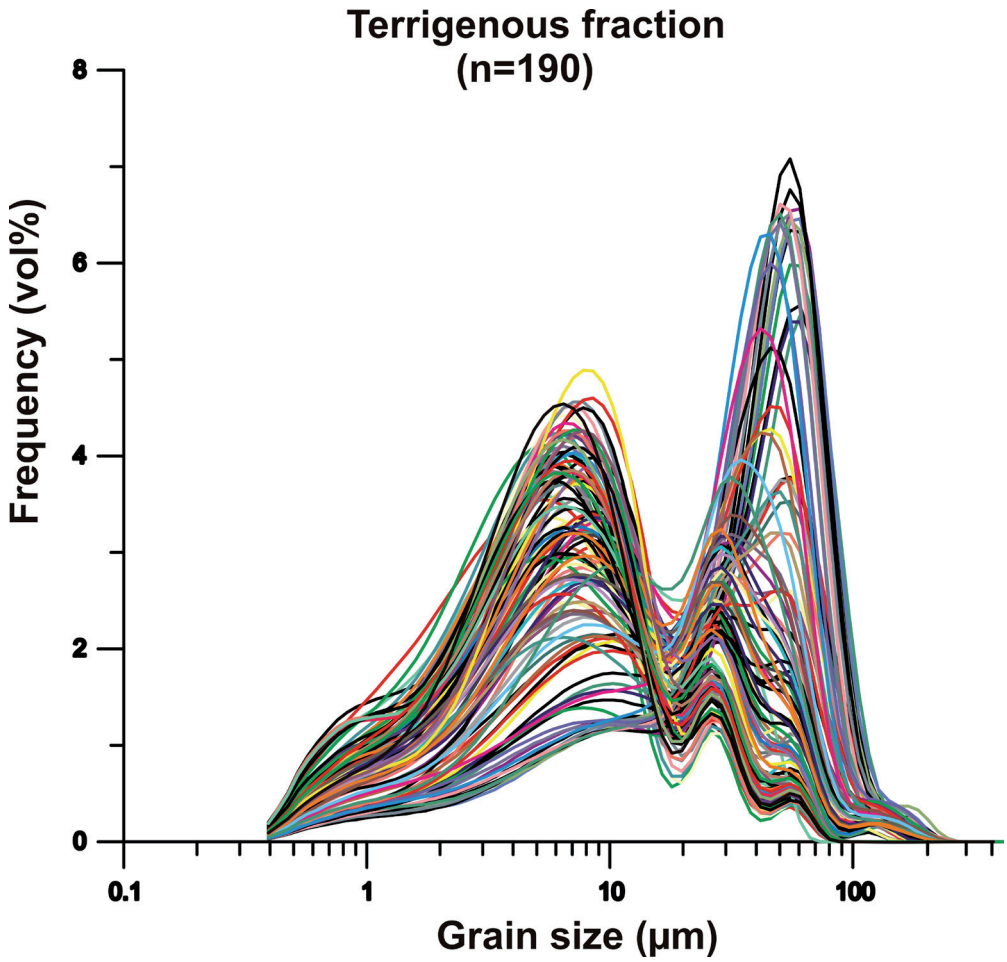

Fig. 4.2 Grain-size distributions of the terrigenous sediment fraction (n=190) of core GeoB 9508-5, offshore Senegal. Measured grain-size distributions show several modes, most obvious at ~8 µm and ~55 µm.

explanation of the data. r^2 characterizes the proportion of variance of every grain-size class that can be reproduced by the approximated data [*Weltje*, 1997; *Weltje and Prins*, 2003].

The distribution of r^2 was plotted against grain size for different numbers of end-member models (Fig 4.3b). With the two end-member model, grain sizes between 13-16 µm are poorly reproduced. It can be clearly seen in Fig. 4.3b that the higher the number of end members, the better the reproducibility. This is obvious in Fig. 4.3c as well. Here, the mean coefficient of determination (r^2_{mean}) is plotted against different end-member models, ranging from two to 10 end members. In general, the higher r^2_{mean}, the better the reproducibility. The r^2_{mean} for the three end-member model is 0.84, i.e. on average 84% of the variance in each grain-size class can be reproduced (Fig. 4.3c). The r^2 increases only slightly for models with more than three end members. Consequently, the three-end member model provides a realistic resolution and meets the requirement of a minimum number of end members and maximum reproducibility [*Prins and Weltje*, 1999; *Weltje*, 1997]. The grain-size distributions of the three end-members are presented in Fig. 4.3d.

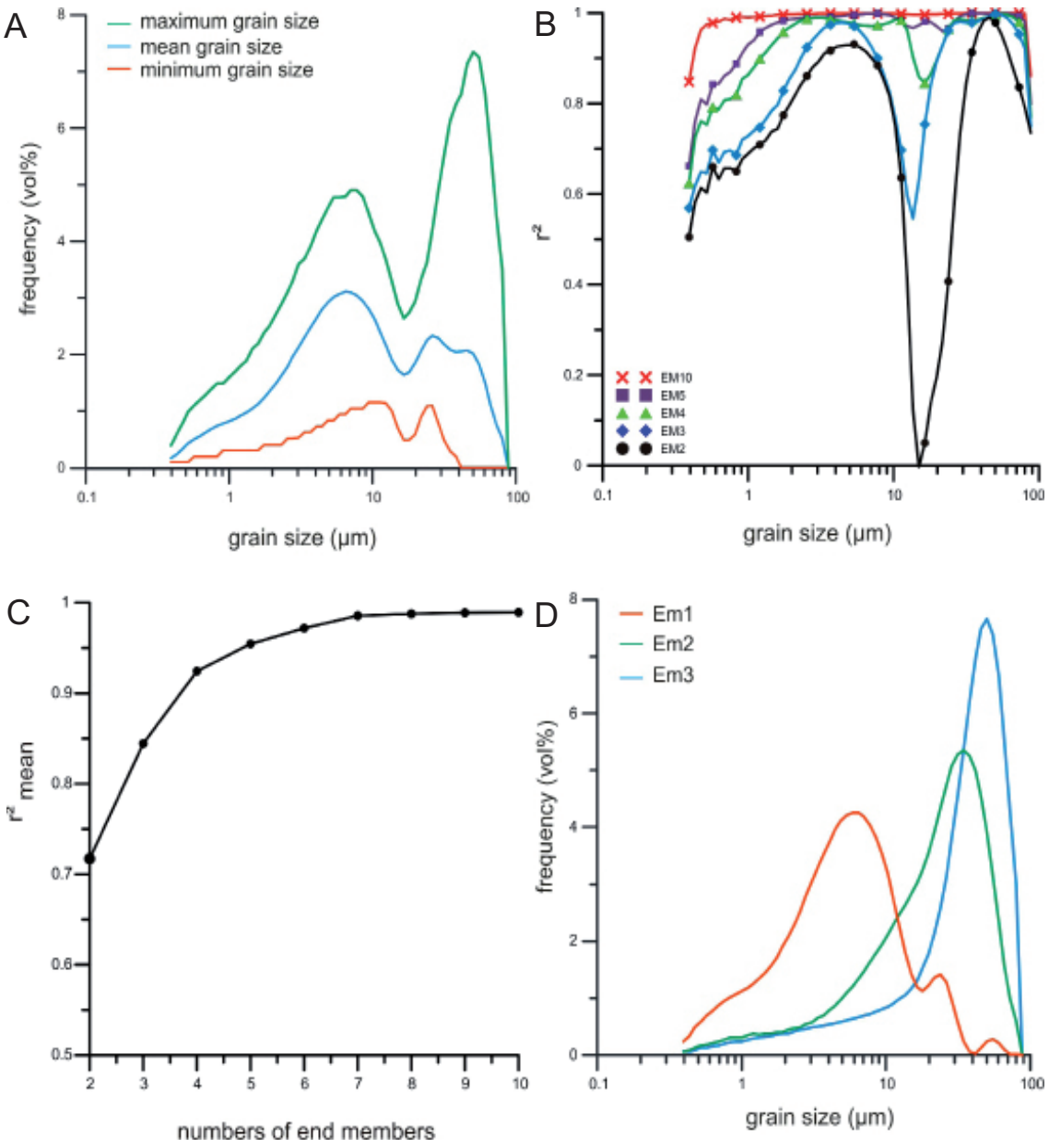

Fig. 4.3 End-member modeling results of core GeoB 9508-5. (A) Summary statistics for the mean, minimum and maximum size distribution. (B) Coefficients of determination (r^2) for each size class of end-member models. (C) Mean coefficient of determination (r^2_{mean}) for models with two to ten end members. (D) The three end-member model chosen for GeoB 9508.

All end members are almost perfectly unimodal and very-well sorted. The coarsest end member (EM3) has a clearly defined mode at 55 µm. EM2 shows a mode at 32 µm. EM1 has a modal grain size of 5 µm.

Based on the assumption that each calculated end member is independent and resulted from distinct transport and/or depositional mechanisms, one is able to reconstruct paleoenvironmental conditions (climate, atmosphere and ocean circulation) at the time of deposition.

4.3. Radiogenic isotopes

Isotopic analyses were carried out in three different time slices of contrasting climate conditions within NW Africa: I) recent = REC/ or late Holocene times = LH (arid and warm), II) African Humid Period = AHP (wet and warm) and III) Younger Dryas = YD (arid and cool). Time slices were chosen based on individual age models of the marine sediment cores combined with results from grain-size measurements, assuming that the median grain size is finer during humid periods, due to an enhanced fluvial supply and an increase in grain size as an indicator of more arid conditions. Isotopic analyses were determined in two distinct size fractions, a fine fraction (0-10 µm) and a coarse fraction (10-40 µm). Grain-size separation was performed at the Atterberg laboratory (University of Bremen) in settling tubes using Stoke's Law. After the separation grain-size measurements on both size fractions were carried out to check if the separation was successful.

4.3.1. Sample preparation for isotopic analysis

Sample preparations for the isotopic analysis were carried out in a "class-100" ultraclean laboratory (according to the U.S. Federal Standard 209B) at the VU Amsterdam. The term "class -100 laboratory" means that every cubic meter of air contains less than 100 particles. About 100 mg of every sample was used for radiogenic isotope analysis. In order to dissolve all authigenic and biogenic carbonates, as well as absorbed marine Sr-Nd fractions, all samples were leached with 1 *N* HCl before digestion. 4 ml 40% HF distilled and 1 ml concentrated HNO_3 (65%) were added to the dried and finely powdered sediment. This mixture was heated for 5 days on a hotplate at 140°C. Dissolution of the coarser fraction (>10 µm) took place in Teflon-lined acid digestion bombs to dissolve zircons, which potentially remain intact in the samples. The bombs were put in stainless steel jackets and were stored in an oven at 220°C for at least five days. Afterwards, the samples were dried again on a hotplate and heated with 1 ml concentrated HNO_3 (65%) for at least 2 hours. This step was repeated a second time. Finally ± 28 g HCl (distilled) was added to the samples and heated for one day at 120°C, dried and re-dissolved with 1 ml 3.0 *N* HNO_3. After total digestion the samples were centrifuged 4 minutes at 12.000 rounds per minute. An aliquot of the residue was used for major- and trace-element analyses. Measurements were obtained using an Quadrupole Thermo X-Series II inductively coupled plasma-mass spectrometer (ICP-MS) at the VU, Amsterdam.

4.3.2. Chemical separation and measurement of strontium

An aliquot of the residual fractions of the samples, which corresponds to 1 µg Sr, was used for the isotope analysis. The separation of strontium was done using column extraction with cation-exchange resin. Approximately 100 µl of SrSpec® resin was filled into calibrated quartz-columns and washed three times alternating with 3 *N* HNO_3 dist. and deionised water (Milli-Q). The preconditioning of the resin was done with 3 *N* HNO_3. Subsequently, each sample was

loaded on one single column. Finally Sr fraction was eluted with 2 ml deionised water and collected in pre-cleaned PFA beakers. Those PFA beakers consist of a perfluoxy copolymer, which is highly resistant to heat and chemical contamination. Before the ICP-MS-measurements the dried samples were nitrated twice with a drop of concentrated HNO_3 (65%).

Isolated Sr was evaporated onto an outgassed rhenium filament using 2 µl 2% H_3PO_4 as loading chemical and 2 µl $TaCl_5$ as a surface modifier. Samples were measured with a Finnigan MAT 262 thermal ionization mass spectrometer (TIMS) in a static mode (run temperature: ~ 1800 C°). A mass spectrometer is capable of making very precise measurements with a precision of better than 0.01%, of isotope ratios of elements that can be ionized thermally. The Finnigan MAT 262 (see Fig. 4.4) is composed of three major components: 1) the ion source, where ions are produced by thermal heating, accelerated, and focused; 2) the electromagnetic analyzer, where the beam is dispersed into separate beams on the basis of their mass to charge ratio; and 3) the collector, where the ion beams are measured. The Finnigan MAT 262 at the VU Amsterdam is a multi collector, which means that there are several detectors so that different isotopes or masses can be measured simultaneously. Mass-dependent fractionation of $^{87}Sr/^{86}Sr$ ratios was corrected during mass spectrometric measurements following an exponential law based on $^{86}Sr/^{87}Sr = 0.1194$. To facilitate immediate comparison of data from different laboratories, Sr

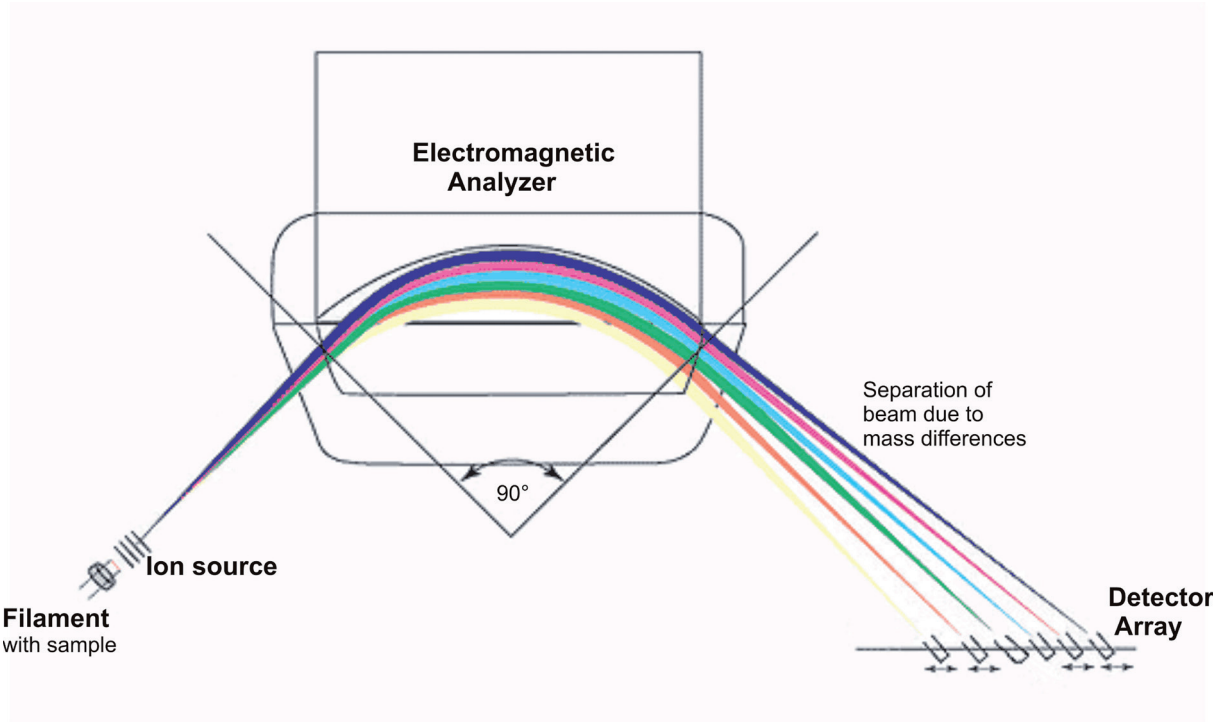

Fig. 4.4 Schematic of the Finnigan MAT 262 thermal ionization mass spectrometer (TIMS). The Finnigan MAT 262 is composed of three major components: 1) the ion source, where ions are produced by thermal heating, accelerated, and focused; 2) the electromagnetic analyzer, where the beam is dispersed into separate beams on the basis of their mass to charge ratio; and 3) the collector, where the ion beams are measured (modified after Mueller and Vervoort [2010]; (http://serc.carleton.edu/research_education/geochemsheets/techniques/TIMS.html).

isotope data are also reported relative to known standards. During the course of analyses the international standard NBS 987 was measured. Values for all measured standards in this study are listed in Table 4.1. Blanks yield < 200 pg so that blank contribution to the analyses can be neglected. Duplicate Sr isotope analyses were performed on some samples. All duplicates fall within uncertainty and variations can be considered negligible compared to the overall variation of isotopic compositions.

4.3.3. Chemical separation and measurement of neodymium

Isolation of the neodymium from the samples was done in two steps. The first step was to separate the rare earth elements (REE) from the aqueous solutions. This was done via column extraction. Approximately 600 µl of TRU-Spec resin was pipetted onto each column and washed three times alternating with 2 *N* HNO_3 distilled and deionised water. The preconditioning of the resin was done with 2 *N* HNO_3. Subsequently, each sample was loaded on one single column. Finally, the REE fraction was eluted with 3 ml deionised water and collected in pre-cleaned PFA beakers. After evaporation of the overlying solution the residue was re-dissolved in 0.5 ml 0.165 *N* HCl and centrifuged 4 minutes at 12.000 rounds per minute.

In a second step Hexyl di-ethyl hydrogen phosphate (HDEHP) columns were used to extract the neodymium from the REE fraction. The resin was washed 3 times alternating with 6 *N* HNO_3 and deionised water. Furthermore, the columns were cleaned with 30 ml 6 *N* HCl over night. Subsequently, the resin was washed with 3 ml deionised water again and preconditioned with 0.165 *N* HCl. Again, each centrifuged sample was loaded on one single column. After washing the loaded sample with 0.165 *N* HCl, neodymium was eluted with 2 ml 0.30 *N* HCl and collected in pre-cleaned PFA beakers.

Nd isotope composition were determined on a ThermoFinnigan Neptune multiple collector inductively coupled plasma mass spectrometer (MC-ICP-MS), VU Amsterdam. By simultaneous collection of several isotopic peaks the Neptune ensures high precision for isotope ratios on transient signals. Prior to measurement, the Nd fractions were re-dissolved with 2% HNO_3 and aspirated into the ICP source using a nebulizer. To minimize memory effects, the introduction system was cleaned with a 3% HNO_3 solution after each measurement. $^{143}Nd/^{144}Nd$ isotope ratios were corrected for mass fractionation by normalizing to $^{146}Nd/^{144}Nd = 0.7219$ respectively. An internal standard, CIGO (see Table 4.1), is used to monitor Neptune performance.

Due to the extremely small variations in the isotopic composition between $^{143}Nd/^{144}Nd$ isotope ratios are often shown relative to the Chondritic Uniform Reservoir value (CHUR). This value is calculated based on measurements of stony meteorites that have not been modified by melting or differentiation processes during origin [*Bischoff & Geiger*, 1995]. Nd isotopic compositions are calculated like:

$$\varepsilon_{Nd}\left[\frac{\left(\frac{^{143}Nd}{^{144}Nd}\right)sample-\left(\frac{^{143}Nd}{^{144}Nd}\right)CHUR}{\left(\frac{^{143}Nd}{^{144}Nd}\right)CHUR}\right]x\,10^{4}$$

The CHUR value represents the global mean isotopic composition deduced from measurements in chondrites. This value is presently 0.512636 according to *Jacobsen &Wasserburg* [1980]. For a better comparison with other data sets $^{143}Nd/^{144}Nd$ isotope ratios determined in this thesis are expressed in ε_{Nd}.

Table 4.1. Values of standards measured during this isotopic study.

Standards	Isotope	Value	Quantity	std.err.
CIGO	$^{143}Nd/^{144}Nd$	0.511335	n=18	0.000002
BHVO 2	$^{87}Sr/^{86}Sr$	0.703488	n=5	0.000007
BHVO 2	$^{143}Nd/^{144}Nd$	0.512987	n=3	0.000005
MAG-1	$^{87}Sr/^{86}Sr$	0.722638	n=3	0.000009
MAG-1	$^{143}Nd/^{144}Nd$	0.512070	n=2	0.000008
NBS 987	$^{87}Sr/^{86}Sr$	0.710241	n=10	0.000004

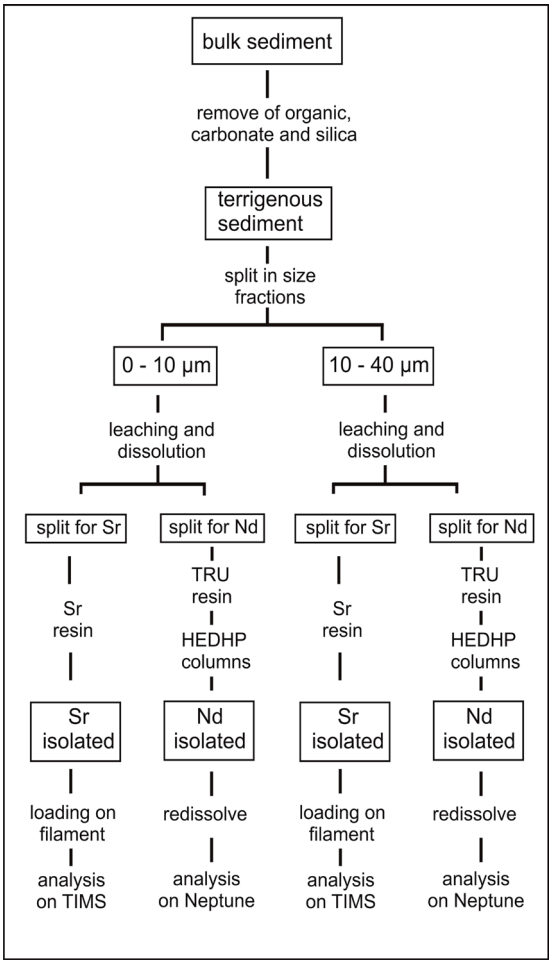

Fig. 4.5 Analytical chemistry flow chart for isotopic analyses of the terrigenous sediment samples including pre-treatment steps and grain-size separation using Stoke's law. In addition an aliquot of the dissolved fractions were analysed for major- and trace-elements.

Grain-size control on Sr-Nd-isotope provenance studies and impact on paleoclimate reconstructions: an example from deep-sea sediments offshore NW-Africa

Inka Meyer[1], Gareth R. Davies[2], Jan-Berend W. Stuut[1,3]

[1] MARUM- Center for Marine Environmental Sciences, Bremen, Germany
[2] Department of Petrology, VU University Amsterdam, The Netherlands
[3] NIOZ, Royal Netherlands Institute For Sea Research, The Netherlands

Published in *Geochemistry, Geophysics, Geosystems (G^3)*

Five sediment cores from offshore NW Africa were analyzed for strontium and neodymium isotope ratios to reconstruct temporal variations in the continental weathering regimes. Sediments were taken from three time slices with well-known and distinctive environmental conditions (present-day – dry/warm; ~6 ka – wet/warm; ~12 ka – dry/cold). Terrigenous sediment samples were split into two size fractions to distinguish between the two dominant transport mechanisms offshore NW Africa, fluvial (0-10 µm) and aeolian (10-40 µm). Sr isotope data record evidence of marked grain-size control with higher isotopic ratios in the fine fraction. In contrast, ε_{Nd} values are unaffected by grain size.
Minor variability in Nd isotope data, <3 ε_{Nd}, at each sampling site indicates near constant sources of terrigenous matter over the last ~12 ka. Variations in Sr isotope ratios are interpreted to reflect major changes in the evaporation/precipitation balance. We suggest that the Sr-Nd isotope data record a latitudinal shift of the African rainbelt and associated wind systems causing changes in the humidity and rate of chemical weathering over NW Africa. While hyperarid conditions prevailed ~12 ka, more humid conditions and intensified monsoonal rainfall at ~6 ka resulted in greater breakdown of easily weathered k-bearing phases and increased $^{87}Sr/^{86}Sr$ in the detritus. In late-Holocene times, the monsoonal circulation diminished resulting in a return to arid conditions. Our results clearly show that it is of vital importance in paleo-environmental studies to carry out isotopic analyses on individual sediment fractions that were carried to the studied deposition site by distinct sediment transport mechanisms. If isotopic analyses are carried out on bulk sediments, the observed variability in isotopic values most likely represents changes in the particle size, and mixing proportions of the sediment subpopulations.

Keywords: Holocene, Sr-Nd isotopes, provenance, grain-size effect

This chapter is based on: doi:10.1029/2010GC003355

1. Introduction

1.1. Provenance studies

The terrigenous fraction deposited in marine sediments offshore NW Africa forms an excellent archive of hydrological and climatic changes on the continent at different temporal and spatial scales [e.g., *Tjallingii et al.,* 2008]. In regions downwind of deserts, such as the Sahara, aeolian dust is the major component of the terrigenous fraction in deep-sea sediments [e.g., *Stuut et al.,* 2002]. Based on satellite images, like Total Ozone Mapping Spectrophotometer (TOMS; Fig.1) the huge plume transporting dust from the African interior to the Atlantic can be easily monitored. The particle size of the transported dust varies as a function of the distance from source to sink and altitude

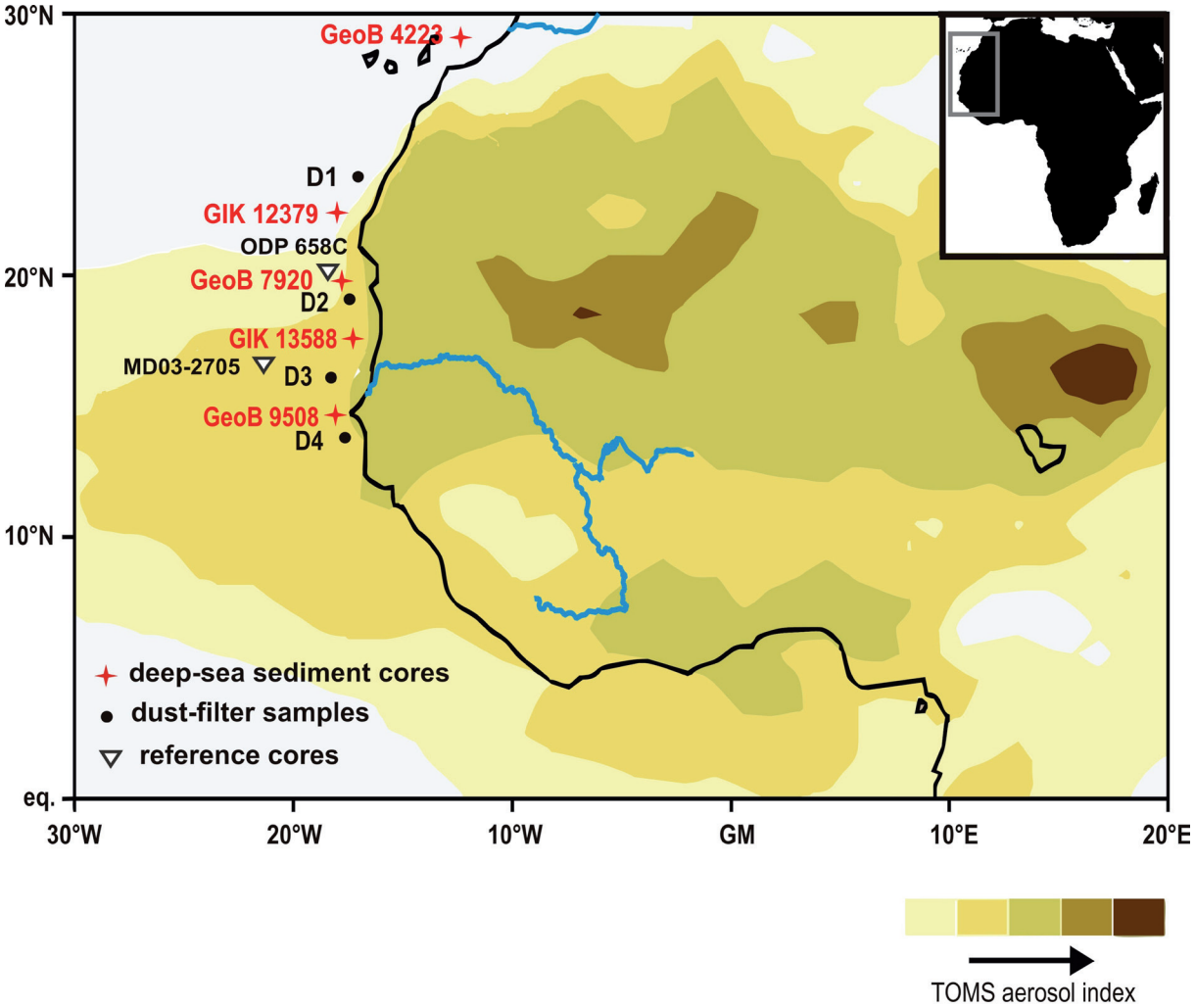

Fig. 1.
Averaged aerosol concentrations using TOMS (http://toms.gsfc.nasa.gov/) with location of sediment cores and averaged dustfilter samples, labled D1 to D4 (plotted is the middle position between start and end of sampling). White triangles display location of reference cores.

at which the particles are transported [*Stuut et al.,* 2005]. Proximal aeolian dust from the Cape Verde Islands contain grains up to 90 µm in diameter [*Glaccum and Prospero,* 1980]. *Stuut et al* [2005] detected particle sizes larger than 10 µm in modern atmospheric dust samples collected off Senegal and Mauritania. Although NW Africa is presently a dry region, terrigenous material supplied by rivers is another significant component in NE Atlantic sediments [*Holz et al.,* 2007]. Terrigenous material transported by rivers is much finer in size compared to the dust fraction. *Gac and Kane* [1986] investigated the fluvial sediment supplied by the Senegal River and found that 95% of the grain sizes are below 10 µm. Similar values were observed offshore of the Souss River system, which drains the Atlas Mountains in Morocco [*Weltje and Prins,* 2007].

Grain-size measurements can successfully distinguish between the different transport mechanisms of terrigenous sediments because the sediment-transport process leaves a characteristic grain-size signature on the sediments it carries [e.g. *Stuut et al.,* 2002; *Weltje and Prins,* 2007]. Downcore measurements of grain sizes on marine sediment cores offshore NW Africa demonstrate a temporal change in the amount of fluvial and aeolian input, with an increase of fluvial supply during humid periods [e.g. *Tjallingii et al.,* 2008]. Conversely, during arid periods the amount of wind- blown material is higher than the fluvial supply [e.g. *Mulitza et al.,* 2008].

Although grain-size measurements can constrain different transport mechanisms, they are unlikely to be diagnostic of the geological source area of the terrigenous material or to reflect the environmental conditions on land. The aim of this study is to reconstruct the provenance of the terrigenous fraction and to investigate the hydrological changes in NW Africa since ~12 ka in three key time slices that represent expected periods of extreme climate (present-day – dry/warm; ~mid-Holocene – wet/warm; Younger Dryas (~12 ka) – dry/cold). Therefore, in addition to grain-size distributions of the terrigenous sediment fraction we report the strontium (Sr) and neodymium (Nd) isotopic composition of the terrigenous sediments to provide information on sediment provenance and continental weathering.

Strontium is very mobile during chemical weathering and easily removed from the source region [*Blum and Erel,* 2003; 1997]. Therefore, variations in the $^{87}Sr/^{86}Sr$ ratio of sediments have been demonstrated to be a powerful tool to identify changes in the continental hydrology and chemical weathering regimes [e.g. *Blum and Erel,* 2003; *Jung et al.,* 2004; *Weldeab et al.,* 2002]. Contrary, Nd isotopes are not altered and therefore not fractionated during near-surface processes, such as chemical weathering. Hence, the isotopic composition of $^{143}Nd/^{144}Nd$ has been demonstrated to be a reliable indicator of the provenance of the terrigenous fraction of marine sediments [*Blum and Erel*, 2003; *Fagel et al.,* 2002; *Goldstein and O'Nions,* 1981].

Hence, combined Sr-Nd isotope analysis of sediments characterized by size-selective

sediment-transport mechanisms potentially enables the distinction and quantification of the contribution of different source areas and the reconstruction of regional weathering regimes. This study applies this methodology to the Holocene within NW Africa to determine how the sedimentary record responds to major climatic change.

1.2. Modern and Holocene NW African climate

Presently, two main features control the rainfall over NW Africa. In the southern parts of the Saharan Desert the West African monsoon generates summer rainfall. The northern part is dominated by the migration of cyclones, causing winter rain [*Nicholson,* 2000]. The main driver of the atmospheric circulation over the region is the seasonal migration of the tropical rainbelt; its core lies at 5°N during boreal winter and at 20°N during boreal summer [*Nicholson,* 2000]. Besides these seasonal fluctuations it is assumed that the latitudinal position and/or the intensity of the wind belts has changed over geological time scales and caused variations in the hydrological conditions on land. Evidence for a change in the evaporation/precipitation balance in NW Africa during the Holocene is reported in several studies [e.g. *Gasse and Van Campo,* 1994; *Gasse et al.,* 1990]. At least on the Northern Hemisphere, the end of the Pleistocene is marked by a pronounced cold and dry period, the Younger Dryas [YD; ~12.8 to 11.5 ka; *Kennett,* 1990]. Evidence of the YD in NW Africa is widespread [*Gasse and Van Campo,* 1994; *Marret and Turon,* 1994]. Proxy and model based reconstructions indicate a change in the atmospheric circulation and stronger northeastern trade winds as well as a shift to cooler and drier conditions throughout NW Africa [*Holz et al.,* 2007; *Marret and Turon,* 1994].

After the termination of the YD, increased summer insolation and an intensified monsoon circulation linked to a northward shift of the African rainbelt over NW Africa caused more humid conditions and increased vegetation cover [*Nicholson,* 2000; *Tjallingii et al.,* 2008]. Evidence for wetter conditions during the early- and mid-Holocene was found in numerous geological, palynological, and hydrological records throughout NW Africa; the so-called African Humid Period [AHP; e.g. *deMenocal et al.,* 2000a]. Based on an atmospheric general circulation model *Kutzbach and Street-Perrott* [1985] concluded that the precipitation over the Sahel at 9 ka was ~30% higher than today. *DeMenocal et al.* [2000b] reported 47% less aeolian dust supply to the Atlantic during the AHP, providing further evidence of significant climate change.

In marine sediment cores offshore West Africa an increase in dust deposits is recorded since 5.5 ka, towards the end of the Holocene, pointing to drier conditions [*deMenocal et al.,* 2000a]. Several proxy investigations report evidence of an aridification since the mid-Holocene throughout the Sahara and the Sahel [*Gasse and Van Campo,* 1994]. These proxy- based investigations are consistent with climate-modeling studies [*Renssen et al.,* 2006].

1.3. Grain-size effect in Sr and Nd isotopes

The impact of grain-size on the isotopic fractionation in sedimentary rocks is a known but often neglected problem. Many studies have established differences in the isotopic signature of different grain-size fractions [e.g. *Blum and Erel,* 2003; *Dasch,* 1969]. While the influence of grain size on the isotopic composition of Sr is proven by numerous studies [e.g., see review by *Blum and Erel,* 2003], the effect of grain size on Nd isotope ratios is still a matter of debate. *Dasch* [1969] was the first to report increasing $^{87}Sr/^{86}Sr$ ratios with decreasing grain size and vice versa. In contrast, comprehensive studies of the isotopic composition of $^{143}Nd/^{144}Nd$ have shown that Nd is largely unaffected by grain-size variations. *Goldstein et al.* [1984] found only slightly changes of about $\pm 0.3\varepsilon_{Nd}$ between different size fractions of fluvial sediments. Several studies report the influence of grain size on the combined Sr-Nd isotope composition of different sediments [e.g. *Grousset et al.,* 1992]. Recently, *Feng et al.* [2010] analysed Sr and Nd concentrations in seven distinct size fractions from Chinese loess and aeolian dust. They discovered that the isotopic ratio of Sr is strongly influenced by grain size but that there is no influence on ε_{Nd} values.

Most previous Sr-Nd isotope provenance studies concentrated on bulk samples or single size fractions [e.g. *Cole et al.,* 2009; *Jullien et al.,* 2007]. However, numerous proxy studies suggest that there are variable contributions of detritus to individual sediments from different grain-size fractions, related to different sediment-transport mechanisms, such as riverine suspension load and wind-blown dust [e.g. *Holz et al.,* 2007; *Stuut et al.,* 2002; *Weltje and Prins,* 2003]. Hence different transport mechanisms contributing different grain-size fractions, which should be visible within the isotopic composition as well. For a detailed paleo-environmental interpretation or to reconstruct the evaporation/precipitation balance we need to take these grain-size differences into account.

The aim of this work is to quantify the magnitude of the grain-size effect by using two different size fractions that represent clearly resolved end members following detailed grain-size analysis, a fine fraction (0-10 μm) and a coarse fraction (10-40 μm), representing fluvial mud, and aeolian dust, respectively.

2. Material and methods

The study was performed on five deep-sea sediment cores offshore NW Africa, sampled at three time slices, and four dust filter samples (Fig. 1). The marine cores (between 29°N and 15°N) and atmospheric dust samples were recovered during several cruises of *R/V Meteor* offshore Morocco, Western Sahara, Mauritania and Senegal. Exact locations of marine cores and dust filter samples can be found in the Supplementary Information (SI).

2.1. Grain-size analyses

In order to investigate variations in the sediment supply of the terrigenous fraction since the YD, grain-size distributions were determined using a laser diffraction particle

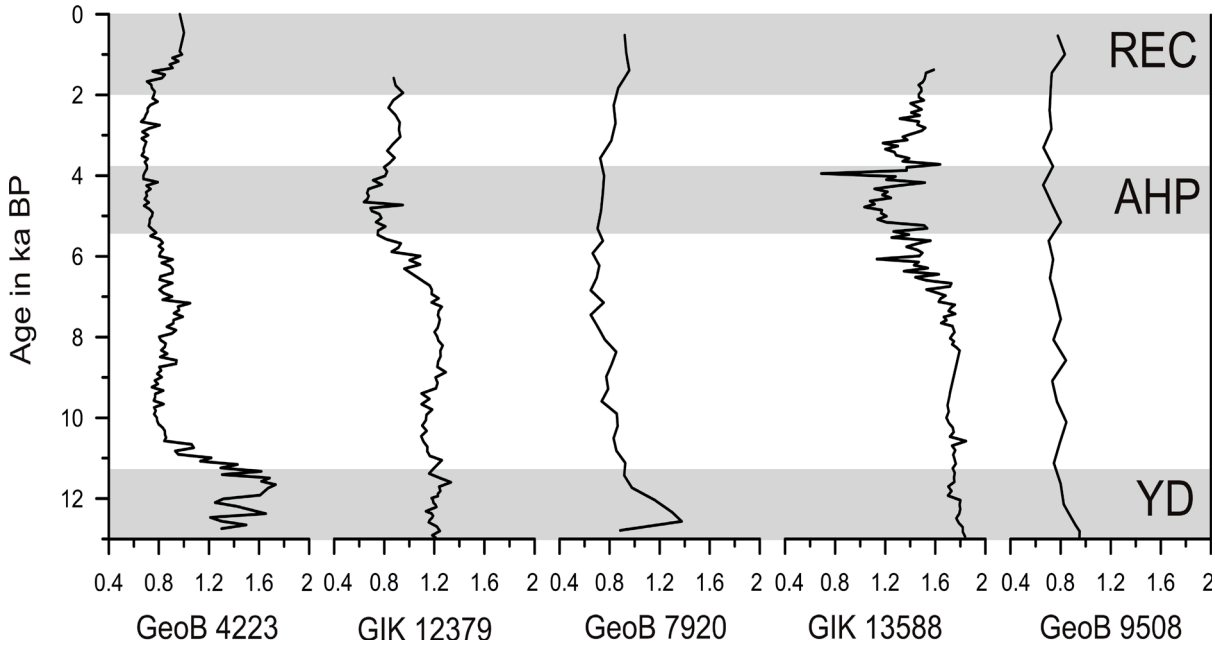

Fig. 2.
Log-ratios of the median grain sizes of all five cores are calculated relative to a basis of 10 (log_{10}) and plotted against sedimentary age. Grey bars are defined time slices of recent times (REC), the African Humid Period (AHP) and Younger Dryas (YD).

size analyzer (Beckman Coulter) LS200, resulting in 92 size classes from 0.4-2000 µm. Organic material, calcium carbonate, and biogenic silica were removed before the measurement. To verify that all components were removed successfully, microscope analyses were carried out on selected samples. For the grain-size measurements cores GeoB 4223, GIK 12379 and GIK 13588 were sampled every cm, core GeoB 9508 and GeoB 7920 every 5 cm. All pre-treatments and grain-size analyses were performed in the laboratories at MARUM, Bremen.

Downcore log_{10}-ratios of the median grain sizes of all cores are reported in Fig. 2. With emphasise on the trend and not on the amplitude log_{10}-ratios are chosen. As absolute dates were not always available for the individual sediment records, samples were selected based on maxima and minima in the median grain-size records, in combination with the published age models for the individual records (see SI). This means that samples were selected to cover the well-known climatic extremes (recent= REC, African Humid Period=AHP, Younger Dryas= YD) based on the observed expression of those extremes in the grain-size data, rather than based on reconstructed age models. Generally the YD yield coarsest grain sizes, while during the AHP finest grain sizes are observed. The REC period yields coarser material again. Grain-size measurements of

Following page

Table 1
Results of isotopic measurements of all five deep-sea sediment cores and three time slices and of the four dustfilter samples. Due to the limited sample size Nd measurements of GIK 12379 and GIK 13588 are only available for the fine fraction. For Sr duplicates from a separate solution are listed.

Core	Period	Fraction	$^{143}Nd/^{144}Nd$ ($\pm$ 2σ)	ε_{Nd}	$^{87}Sr/^{86}Sr$ ($\pm$ 2σ)	Rb/ppm	Sr/ppm	$^{87}Rb/^{86}Sr$	Sm/ ppm	Nd/ ppm	$^{147}Sm/^{144}Nd$	T_{BE}(Ga)	T_{DM}(GA)	T_{BE} /T_{DM}
GeoB 4223	REC	0-10 µm	0.512058 (12)	-11.3	0.716003 (09)	133.0	283.4	1.359	8.20	45.02	0.11009	0.61	1.65	0.368
Duplicate					0.716771 (08)									
GeoB 4223	AHP	0-10 µm	0.512042 (12)	-11.6	0.713654 (07)	124.8	424.2	0.852	7.06	39.68	0.10754	0.80	1.64	0.485
Duplicate					0.713220 (10)									
GeoB 4223	YD	0-10 µm	0.512028 (12)	-11.9	0.712549 (12)	105.8	439.8	0.690	6.47	35.85	0.10908	0.87	1.68	0.518
Duplicate					0.711915 (09)									
GeoB 4223	REC	10-40 µm	0.512071 (14)	-11.0	0.716460 (09)	70.70	204.4	1.002	5.56	28.35	0.11854	0.88	1.89	0.466
Duplicate					0.716481 (10)									
GeoB 4223	AHP	10-40 µm	0.512053 (08)	-11.4	0.710725 (08)	53.58	537.5	0.289	5.28	26.11	0.12222	2.00	1.96	1.020
Duplicate					0.710688 (09)									
GeoB 4223	YD	10-40 µm	0.511993 (11)	-12.6	0.721564 (10)	16.23	51.13	0.927	0.35	1.85	0.11435	1.38	1.82	0.758
Duplicate					0.721557 (10)									
GIK 12379	REC	0-10 µm	0.511911 (09)	-14.2	0.725240 (08)	129.8	137.5	2.732	5.79	33.80	0.10354	0.54	1.75	0.307
GIK 12379	AHP	0-10 µm	0.511848 (14)	-15.4	0.725904 (14)	21.90	226.0	0.281	2.03	9.41	0.13038	0.52	1.74	0.297
GIK 12379	YD	0-10 µm	0.511910 (12)	-14.2	0.730458 (11)	101.6	82.82	3.550	5.22	30.87	0.10220	7.31	2.15	3.402
GIK 12379	REC	10-40 µm	--	--	0.718471 (10)	65.18	187.0	1.011	5.31	33.80	0.09495	1.02	--	--
GIK 12379	AHP	10-40 µm	--	--	0.720755 (23)	27.27	165.8	0.478	2.70	35.00	0.11615	2.80	--	--
GIK 12379	YD	10-40 µm	--	--	0.720560 (13)	28.35	38.11	2.170	0.20	30.87	0.09990	0.53	--	--
GeoB 7920	REC	0-10 µm	0.511876 (14)	-14.8	0.729342 (08)	58.90	68.57	2.509	2.95	17.40	0.10247	0.71	1.79	0.394
Duplicate					0.725364 (06)									
GeoB 7920	AHP	0-10 µm	0.511925 (09)	-13.9	0.723640 (08)	142.6	195.8	2.109	6.51	38.66	0.10177	0.65	1.71	0.378
Duplicate					0.721890 (09)									
GeoB 7920	YD	0-10 µm	0.511869 (10)	-15.0	0.729979 (10)	95.19	255.2	1.080	4.84	28.62	0.10221	0.36	1.62	0.219
Duplicate					0.729981 (07)									
GeoB 7920	REC	10-40 µm	0.511942 (08)	-13.5	0.718066 (09)	67.80	208.1	0.944	4.50	22.80	0.11929	1.07	1.99	0.537
Duplicate					0.717641 (06)									
GeoB 7920	AHP	10-40 µm	0.511843 (09)	-15.4	0.717148 (10)	24.61	91.25	0.780	1.93	8.95	0.13033	1.43	2.43	0.588
Duplicate					0.716607 (10)									
GeoB 7920	YD	10-40 µm	0.511795 (08)	-16.4	0.727354 (09)	28.60	45.66	1.830	0.52	3.16	0.09946	0.29	1.84	0.156
Duplicate					0.727332 (11)									
GIK 13588	REC	0-10 µm	0.511897 (10)	-14.4	0.725818 (13)	161.1	145.2	3.212	6.79	38.65	0.09336	0.47	1.63	0.287
GIK 13588	AHP	0-10 µm	0.511909 (10)	-14.2	0.720430 (18)	47.30	121.7	1.125	1.15	6.33	0.08815	1.04	1.65	0.672
GIK 13588	YD	0-10 µm	0.511932 (11)	-13.7	0.726690 (10)	140.5	151.1	2.690	7.41	33.35	0.09084	0.59	1.79	0.418
GIK 13588	REC	10-40 µm	--	--	0.718345 (09)	11.20	52.36	0.620	2.64	13.50	0.11819	1.75	--	--

GIK 13588	AHP	10-40 µm	--	--	0.718634 (09)	66.20	184.6	1.038	15.00	35.00	0.25904	0.56	--	--
GIK 13588	YD	10-40 µm	--	--	0.712188 (09)	24.81	23.35	3.154	0.30	1.45	0.12505	0.17	--	--
GeoB 9508	REC	0-10 µm	0.511920 (11)	-14.0	0.724864 (06)	43.90	58.13	2.188	2.47	14.32	0.10425	0.66	1.75	0.378
Duplicate					0.725033 (08)									
GeoB 9508	AHP	0-10 µm	0.511923 (09)	-13.9	0.721935 (07)	109.75	117.2	2.712	5.43	30.07	0.10700	0.22	1.64	0.136
Duplicate					0.721929 (09)									
GeoB 9508	YD	0-10 µm	0.511918 (09)	-14.0	0.725970 (09)	65.16	147.4	1.286	5.48	30.48	0.10521	0.51	1.65	0.317
Duplicate					0.725177 (13)									
GeoB 9508	REC	10-40 µm	0.511875 (14)	-14.8	0.719875 (07)	35.50	112.94	0.847	2.36	12.24	0.10247	1.56	1.79	0.871
Duplicate					0.711541 (10)									
GeoB 9508	AHP	10-40 µm	0.511862(08)	-15.1	0.719413 (06)	68.10	156.4	1.173	4.46	22.51	0.10601	0.93	1.86	0.501
Duplicate					0.719830 (06)									
GeoB 9508	YD	10-40 µm	0.511890 (09)	-14.6	0.723053 (09)	25.38	73.43	0.942	3.04	14.87	0.10865	1.38	1.85	0.863
Duplicate					0.723478 (10)									

Dustfilter 1	REC	10-40 µm	0.511900 (10)	-14.3	0.719584 (14)
Dustfilter 2	REC	10-40 µm	0.511881 (09)	-14.7	0.719579 (12)
Dustfilter 3	REC	10-40 µm	0.511872 (09)	-14.9	0.723345 (09)
Dustfilter 4	REC	10-40 µm	0.511908 (10)	-14.2	0.722852 (08)

the dust-filter samples show a mean grain size between 7.1 to 21.7 µm [*Stuut et al.,* 2005]. Based on published end-member modeling [*Tjallingii et al.,* 2008] we separated our terrigenous fraction into two size classes. The fine fraction (0-10 µm) is interpreted as fluvial input, the coarse fraction (10-40 µm) as aeolian material. Grain-size separation was undertaken in settling tubes using Stoke's Law. Grain-size analyses of the single size fractions indicated only minor overlap between both fractions. Furthermore, differences in the mineralogy of the two size fractions were determined by visual inspection using a binocular microscope.

2.2. Sample preparation

Sample preparations for the isotopic analyses were carried out in a "class-100" clean laboratory at the VU Amsterdam. In order to dissolve all authigenic, biogenic carbonate, and absorbed marine Sr-Nd signals, all samples were leached with 1*N* HCl and the dissolved fraction discarded before digestion. Subsequently, samples were dissolved in a HF-HNO_3-HCl mixture. In order to dissolve any possible refractory phases such as zircon, dissolutions of the coarser fractions were performed in Teflon-lined acid digestion bombs at 200°C for 5 days. Two international standards (BHVO-2, MAG-1) were also included in the analytical procedure. Values for standard BHVO-2 gave a value of 0.703488 ± 0.000007 (2σ; n=5) for $^{87}Sr/^{86}Sr$ and 0.512987 ± 0.000005 (2σ; n=3) for $^{143}Nd/^{144}Nd$. Standard MAG-1 gave a value of 0.722638 ± 0.000009 (2σ; n=3) for $^{87}Sr/^{86}Sr$ and 0.512070 ± 0.000008 (2σ; n=2) for $^{143}Nd/^{144}Nd$.

2.3. Isotope analysis

Isotopic measurements where performed at the VU Amsterdam. Strontium isotope compositions were determined using a MAT 262 TIMS. Samples were loaded onto single rhenium filaments and measured in static mode. $^{87}Sr/^{86}Sr$ ratios were corrected for mass fractionation by normalizing to $^{86}Sr/^{88}Sr$ = 0.1194. Over the period of the study, the NBS 987 standard gave an average value of $^{87}Sr/^{86}Sr$ = 0.710241 ± 0.000004 (2σ), n=10. Blanks typically yield < 200 pg so that blank contribution to the analyses can be neglected. Duplicate Sr isotope analyses were performed on separate solutions for some samples (Table 1). The results show that nearly all duplicates fall within uncertainty and variations can be considered negligible considering the overall variation of isotopic compositions.

Neodymium isotope ratios were measured using a ThermoFinnigan Neptune MC-ICP-MS. $^{143}Nd/^{144}Nd$ isotope ratios were corrected for mass fractionation by normalizing to $^{146}Nd/^{144}Nd$ = 0.7219. An internal standard, CIGO, is used to monitor Neptune performance. The analysis of CIGO gave an average value of $^{143}Nd/^{144}Nd$ = 0.511342 ± 0.000004 (2σ), n=10, which equates to a value for the La Jolla international standard determined by TIMS of 0.511850 ± 0.000008 (n=43). Isotope values for all samples are reported in Table 1. Results are reported as $^{143}Nd/^{144}Nd$ and as ε_{Nd} [ε_{Nd} = (($^{143}Nd/^{144}Nd$ sample/ 0.512636)-1)×10^4] using the present-day "chondritic

uniform reservoir" (CHUR) value of 0.512636 [*Jacobsen and Wasserburg,* 1980]. An aliquot (~5%) of each sediment size-fraction was analysed for trace elements by using a Quadrupole Thermo X-Series II ICP-MS.

3. Results

Measured Nd isotope ratios range between ε_{Nd} -11.0 and -16.4 (Table 1). There is a clear difference between the northern-most core (-11.0 to -12.6) and the four cores lying between 23°5 S and 15°5 S (-13.5 to -16.4). Differences in Nd isotope ratios between the three periods in each core are insignificant, < 0.4 ε_{Nd} in all cases. In contrast, $^{87}Sr/^{86}Sr$ ratios vary significantly, between 0.7172 and 0.7304 (Table 1). Data for the fine fraction range between 0.7160 and 0.7293 in the REC. Compared to the REC fine fraction, the $^{87}Sr/^{86}Sr$ ratios of the fine fraction of the AHP time slice are less radiogenic, between 0.7136 and 0.7259. $^{87}Sr/^{86}Sr$ ratios for the fine fraction of the YD are between 0.7126 and 0.7305, reaching values higher than for the REC period. A similar relationship can be observed in the 10-40 µm fractions, where REC samples range between 0.7164 and 0.7199. AHP samples are less radiogenic (0.7107 to 0.7207). The YD has more radiogenic values than the REC, with ratios between 0.7122 and 0.7274. The Sr isotope ratios of the coarse REC samples are within the range recorded for the dust filter samples (0.7196 to 0.7233) and establish that the terrigenous sediment fractions are a good proxy of detritus eroded from NW Africa.

In order to estimate the temporal geochemical evolution of the source regions, Nd and Sr isotope data were used to calculate model ages of the terrigenous material relative to depleted mantle (T_{DM}) and bulk earth (T_{BE}; Table 1). The majority of Nd and Sr model ages vary between 1.62-2.43 Ga and 0.22-2.80 Ga, respectively. The T_{BE} value of 7.31 Ga, calculated for the fine fraction of the YD in core GIK 12379, is considered as an outlier and not taken into account for further discussion. T_{DM} model ages are generally older in the coarse than in the fine fraction. Highest Nd model ages are found in the AHP coarse fraction. Importantly, there is no significant difference between T_{DM} ages of the fine fractions. The Rb/Sr ratio of continental crust is increased by several intra-crustal processes, for example crustal melting or weathering. The greater the number of times crustal material is subjected to such processes the greater the increase in the Rb/Sr ratio [*Blum and Erel,* 2003; *McDermott and Hawkesworth,* 1990]. In contrast, REE abundances are hardly changed by inter-crustal processes so that Sm/Nd remains relatively constant in the upper crust [*Blum and Erel,* 2003]. The effect of increasing Rb/Sr is that Sr model ages (T_{BE}) are reduced whereas Nd model ages (T_{DM}) remain hardly changed. A monitor of the changes caused to Rb/Sr by variations of physical and chemical weathering in sedimentary source regions is therefore provided by the ratio of Sr and Nd model ages; T_{BE}/T_{DM} [see Table 1; *Davies et al.,* 1989; *McDermott and Hawkesworth,* 1990]. This ratio averages 0.35 for the fine fraction compared to 0.63 for the coarse fraction.

4. Discussion

4.1 Grain-size effect

We analysed Sr and Nd in two separate grain-size fractions in order to identify if there is a grain-size effect on the isotopic composition of both elements. Our measurements confirm that the grain-size effect on the Sr isotope composition is significant and must be taken into account when Sr isotope values are interpreted in terms of provenance and/or weathering intensity. It is apparent from Fig. 3 that $^{87}Sr/^{86}Sr$ ratios vary as a function of grain size independently of any climatic fluctuations (left panel). Thirteen of fifteen samples of the fine fraction (open symbols) display higher $^{87}Sr/^{86}Sr$ isotopic ratios than the coarse fraction (filled symbols). This isotopic variation is most obvious within the AHP (Fig. 3, middle). The fine fraction has an average ratio of ~0.721 ± 0.000011 (2σ, n=5), whereas the coarse fraction yields ~0.716 ± 0.000011 (2σ, n=5). A similar distinction is also recorded by the REC samples and the YD samples. Hence, our $^{87}Sr/^{86}Sr$ data demonstrate that there is a significant difference between the fine and coarse size fractions. Isotopic measurements on bulk-sediment samples that are not split into size fractions would give a mixed signal of both size fractions. If transport processes lead to variations in the input of the different size fractions, then bulk analyses will give biases in the isotopic measurements. One possible reason for the grain-size effect could be found in the mineralogy of the samples. From the visual inspection of the samples we know that the coarse fraction is dominated by quartz and feldspar while the fine fraction is enriched in clay minerals and micas. Our observation is corroborated by other investigations of Saharan dust and fluvial supply [*Pye,* 1987; *Stuut et al.,* 2005]. Since Sr is produced by the radioactive decay of Rb, sediments derived from Rb-bearing phases such as clay minerals, yield high $^{87}Sr/^{86}Sr$ rations [*Blum and Erel,* 1997]. However, minerals exhibit different response to chemical weathering [*Blum and Erel,* 1997] with quartz showing a strong resistance to chemical weathering whereas feldspars and clays are more easily broken down. Since Sr is more readily released into solution than Rb during chemical weathering, finer-grained weathering products tend to be enriched in Rb-bearing alteration products such as clays [*Blum and Erel,* 1997; *Faure,* 1986]. Therefore, during enhanced chemical weathering particles and minerals become smaller in size and Sr isotope ratio increases with decreasing particle size. In summary, strontium isotope ratios in sediments are generally higher than the parent rocks and this tendency is more extreme the smaller the sediment grain size and the higher the influence of chemical weathering. In terms of Sr isotope ratios, quartz acts almost as an inert phase in sedimentary systems diluting the influence of Rb and Sr bearing phases. The data presented in this study demonstrates that grain size has a significant impact on the isotopic composition of Sr. Consequently, investigations of bulk-sediment samples without grain-size separations are hard to interpret as the observed changes in isotopic values could simply be the result of changes in grain size due to varying input of dust and

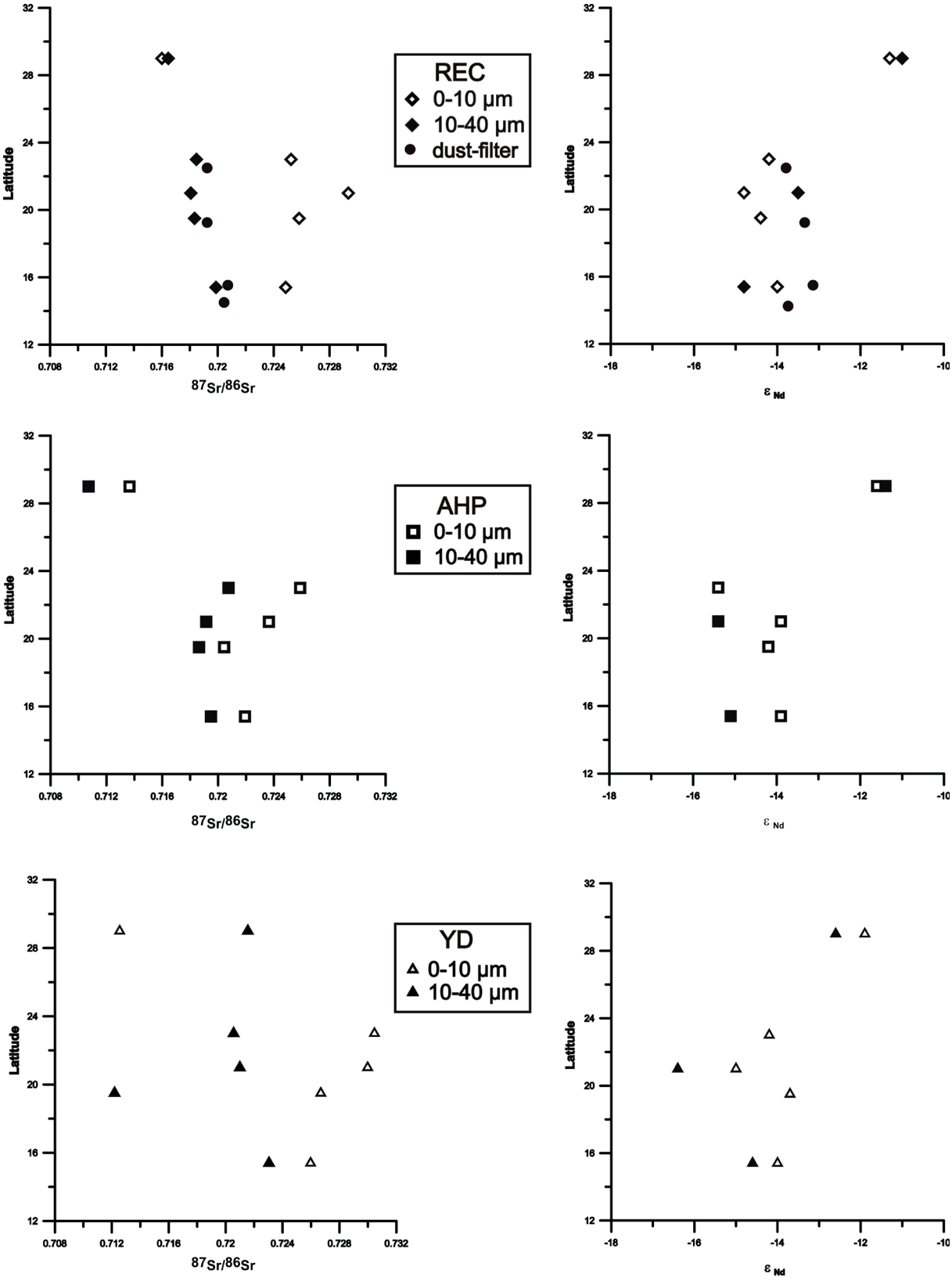

Fig. 3.
Isotopic variations of Sr (left side) and Nd (right side) with grain size. The figure clearly demonstrates that Sr isotopes are strongly influenced by grain size. The fine fraction (open symbols) shows generally more radiogenic values than the coarse fraction (filled symbols). Nd isotopes are not influenced by grain size.

fluvial material. Therefore, great care should be taken with the interpretation of analyses in which size separation has not been performed. In contrast, ε_{Nd} appears unaffected by grain size (Fig. 3, right panel). Averaged ε_{Nd} values for the coarse and fine fractions are very similar, with -13.4 in the fine fraction and -13.8 in the coarse fraction. Equally, the Nd isotope difference between fine and coarse fractions within the different time periods is also minor; REC is 0.3 ε_{Nd}, for the AHP 0.8 ε_{Nd} and for the YD 0.9 ε_{Nd}. Therefore, our data supports the finding of *Goldstein et al.* [1984] that grain size has no significant effect on the ε_{Nd} composition. However, in all cases calculated T_{DM} model ages are older in the coarse than the fine fraction. Since there is no change in the ε_{Nd} values between the fine and the coarse fraction, the difference in model ages can only be due to higher Sm/Nd ratios in the coarser fractions due to the greater abundance of heavy minerals such as zircon [*White et al.*, 1986].

4.2. Provenance of marine sediments off NW Africa

The Nd isotope composition of marine sediments can be influenced by the isotopic composition and crustal age of their parent rocks and by mixing with other material during transport between source and sink. Since Nd isotopes are not fractionated by chemical weathering we use ε_{Nd} as a tracer of the geological provenance. The isotopic data show a clear difference between the northern core off Morocco (~ -11.6 ε_{Nd}) and the cores off Mauritania and Senegal (between -13.5 and -16.4 ε_{Nd}). The observed ε_{Nd} values can be explained by the diverse geology in the area (Fig. 4). Most of the NW African basement belongs to the West African Craton extending

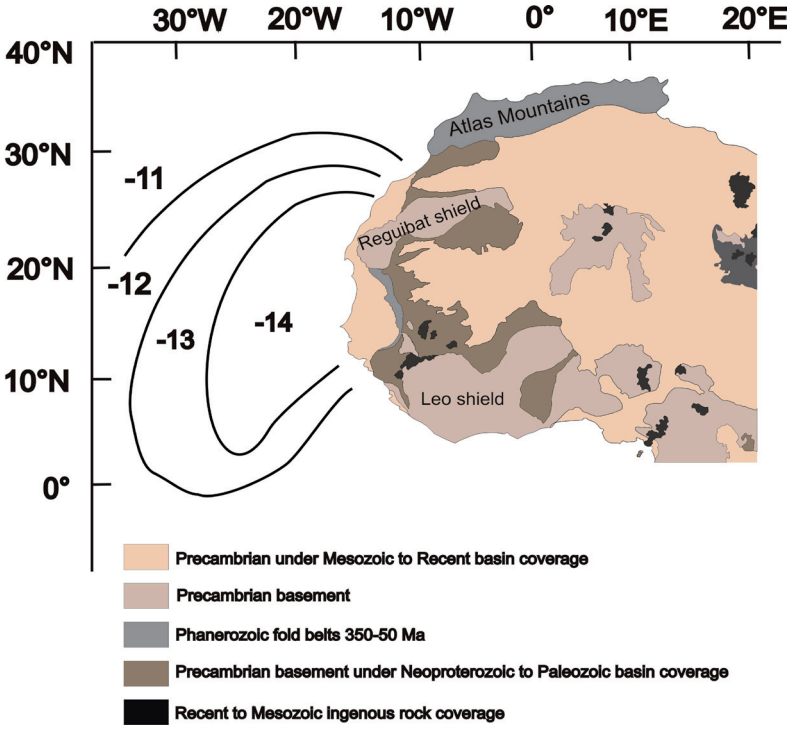

Fig. 4.
Geological map of NW Africa (modified from *Trauth and Schlüter* [2006]). Map shows the present day ε_{Nd} distributions of surface sediments (modified from *Grousset et al.* [1998]).

from the Atlas Mountains in the north to the Gulf of Guinea in the south. The Craton is mainly made up of late Archaean and early-mid Proterozoic crystalline basement rocks [~2.0 Ga; *Lecorche et al.,* 1991]. The oldest rocks are 3.5-3.6 Ga and are exposed in the southwestern part of the Reguibat shield [Fig. 4; *Potrel et al.,* 1996]. The Craton is bounded by the Atlas Mountains in the NNW and, were formed much later in several phases of Earth's history [e.g. *Ennih and Liegeois,* 2008]. The last period of tectonic deformation occurred during the Late Cretaceous-Cenozoic (~65 Ma) when Africa and Eurasia started colliding [*Wright et al.,* 1985]. Therefore, the more radiogenic ratios of GeoB 4223 off Morocco are a consequence of the younger material eroded from the Atlas Mountains. T_{DM} model ages given in Table 1 demonstrate that core GeoB 4223 yields T_{DM} ages of ~1.66 Ga in the fine fraction and ~1.83 Ga in the coarse fraction. In contrast T_{DM} model ages for the southern cores are older, with ~1.74 Ga in the fine and ~1.96 Ga in the coarse fraction. We interpret the isotopic values of the southern cores as dominated by the Archaean West African Craton.

On a Sr-Nd mixing diagram (Fig. 5) we try to interpret the mixtures of the investigated sediments between two possible end-members of the terrigenous fraction obtained from *Grousset et al.* [1998]. In agreement with

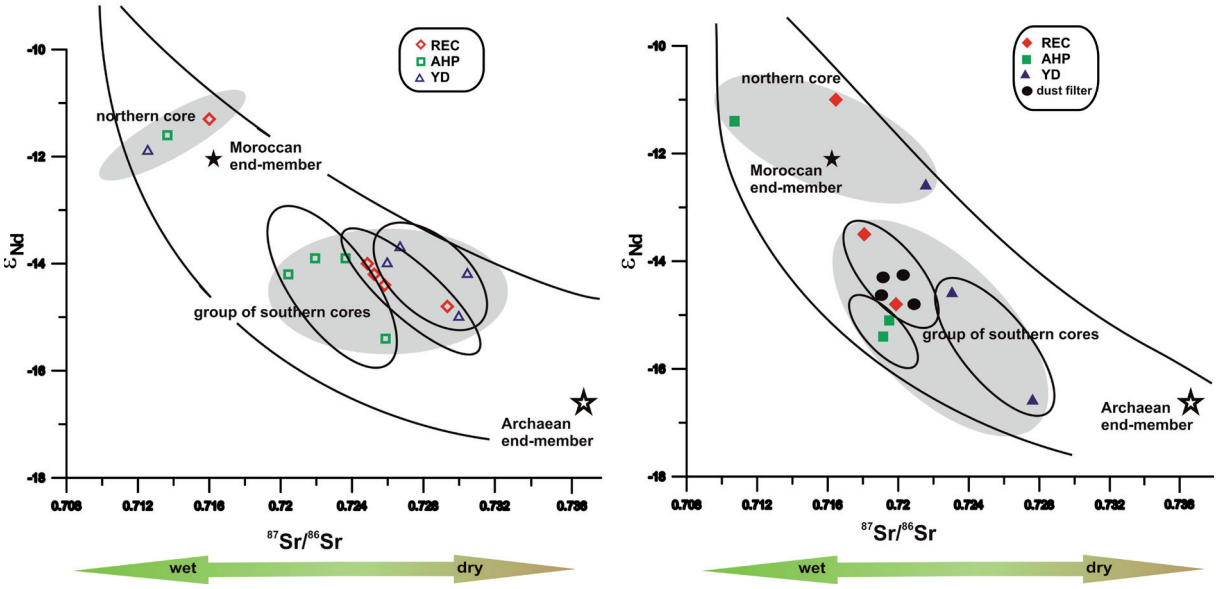

Fig. 5.
A comparison between the isotopic compositions of $^{87}Sr/^{86}Sr$ and ε_{Nd} for the fine (left) and the coarse fraction (right). The figure shows the distinctions between the three periods (ellipse). During the YD (triangles) hyperarid conditions are prevailing, during the AHP (squares) moist conditions can be observed. At recent times (diamonds) a return to dry conditions is indicated. Present-day dustfilter samples (dots, obtained from Stuut et al. [2005]) are in line with REC sampes. ε_{Nd} data show a clear difference of the geologic source area between the northern core and the group of cores south of 23°N. A comparison between both size fractions shows the same trend but a different isotopic ratio. To define possible end members, data from dust source regions on land are included (see Grousset et al., [1998]).

these data the samples presented in this study allow a distinction between the relatively unradiogenic northerly sediment, influenced by sources in the Atlas Mountains and a southerly source dominated by the very unradiogenic signal derived from the Archaean outcrops in Mauritania with ε_{Nd} values between -20.4 and -54.2 [*Potrel et al.,* 1996]. The ε_{Nd} variability in the source areas is, however, not reflected by any resolvable temporal variation in the individual cores sampled in the eastern Atlantic Ocean. This observation strongly implies that the provenance of the sediments have remained constant over the entire Holocene.

Similar findings were recently reported by *Cole et al.* [2009]. They studied marine sediment core ODP 658C offshore Mauritania (Fig. 1) where they found only minor variability of <0.9 ε_{Nd} throughout the last 25 ka. Further support that sediment provenance remained constant comes from the work of *Jullien et al.* [2007] who analysed marine sediment core MD03-2705 offshore Mauritania (Fig. 1) that includes the YD. They found no difference in ε_{Nd} values between the YD (−14.6) and glacial sediments (-14.7). Furthermore, *Grousset et al.* [1998] studied <30 μm sediment fractions from the Recent and the Last Glacial Maximum (LGM) offshore NW Africa and reported no significant changes in ε_{Nd} values between the surface samples and the LGM samples. Therefore, they proposed no significant change in the source area of sediments between the LGM and modern times.

To summarize, the variability in the ε_{Nd} values of sediment size fractions from NW Africa indicates that there are two major source areas. The northern core is influenced by the younger and more radiogenic material originating from the Atlas Mountains and a more southern source dominated by the very unradiogenic old basement rocks of the West African Craton. The minor change in the isotopic record suggests changes in the intensity of the different source areas but no major change in the geological source area since the YD.

4.3. Changes in chemical weathering regime during the Holocene

In marked contrast to the minor changes recorded by ε_{Nd} values, $^{87}Sr/^{86}Sr$ ratios preserve large variations within the different sediment cores (between 0.7107 and 0.7305). Since our study was performed on distinct grain-size fractions we minimized the influence of any grain-size and mineralogy control. In addition, the size separation allows the distinction between aeolian dust (10-40 μm) and fluvial input (0-10 μm). During times of enhanced chemical weathering more ^{87}Sr is eluted from the source material [*Blum and Erel,* 2003]. Hence, low Sr isotopic ratios are interpreted to reflect an increase in chemical weathering and vice versa during arid conditions the effect of chemical weathering is diminished and the Sr isotopic ratio is generally higher [*Blum and Erel,* 1997; 2003; *Jung et al.,* 2004]. Thus, along with other previous workers, we interpret the observed variations in $^{87}Sr/^{86}Sr$ as predominantly a consequence of changes in the evaporation/precipitation balance and the amount of chemical weathering [e.g. *Åberg et al.,* 1989; *Blum and Erel,* 1997; 2003; *Jung et*

al., 2004; *Capo et al.,* 1998; *Dasch,* 1969; *Derry and France-Lanord,* 1996]. The temporal variations in the isotopic record are illustrated in Figures 3 and 5. Since the evaporation/precipitation balance and hence the humidity over NW Africa is mainly influenced by the African rainbelt [e.g. *Mulitza et al.,* 2008], our data can be used as a proxy of north-south oscillation of this rainbelt during the last 12 ka. Fine fraction samples offshore Mauritania and Senegal have the highest $^{87}Sr/^{86}Sr$ ratios (~0.725) during the YD implying dry, desert-like conditions. Samples from the AHP are lower (~0.717) indicating increased humidity and enhanced chemical weathering. $^{87}Sr/^{86}Sr$ ratios of the REC fine fraction (~0.729) display a return to the modern arid conditions within the Sahara region. Similar temporal changes are observed in the coarse fraction. Sr isotope ratios of the coarse REC fraction are comparable to the dustfilter samples (~0.721; Table 1) and these data indicate that the recent sediments represent a true proxy of material eroded from NW Africa under modern dry conditions.

The fine sediment fractions of core GeoB 4223 record a different relationship compared to the southern cores, with lower $^{87}Sr/^{86}Sr$ values (0.7126), indicating wettest conditions during the YD. A higher $^{87}Sr/^{86}Sr$ ratio during the AHP (0.7137) suggests drier conditions during the AHP than within the YD. In recent times the fine fraction from the northern core is consistent with the current arid conditions in having the most radiogenic Sr isotope ratio of the three time intervals (0.7160). The coarse fraction of GeoB 4223 has a different signal compared to the fine fraction. The $^{87}Sr/^{86}Sr$ records comparable variations to the southern cores, with driest conditions during the YD (~0.721), wetter conditions during the AHP (~0.710) and a return to drier conditions in modern times (~0.716). Due to the complex isotopic variations recorded in the different fractions of core GeoB 4223, we propose that during the YD there was a seasonal influence of extra-tropical cool and humid west wind systems.

Variations in the atmospheric circulation over NW Africa and/or a shift in the latitudinal position of the African rainbelt are indicated by several studies [e.g. *Liu et al.,* 2007]. Potentially the northern front of the monsoon belt moved about 700 km to the north during the AHP. The opposite movement is implied during glacial times when the African rainbelt shifted equatorwards compared to modern times [e.g., *Hooghiemstra,* 1988]. As a consequence, the northernmost part of North Africa was influenced by the North Atlantic climate system. Measured Sr isotope ratios of the fine fraction of core GeoB 4223 are in agreement with this finding, they indicate most humid conditions during the YD. During the AHP the African rainbelt had a more northern position than today. While the general climate of NW Africa was more humid during the AHP, the northern part of the African continent was generally wet, but outside the influence of the extra-tropical wind systems [*Nicholson,* 2000]. Hence Sr isotope ratios of the northern core indicate drier conditions during the AHP than during the YD. A northward shift or an expansion of the African rainbelt

and the monsoon winds during the mid-Holocene explain the opposing climatic trends indicated by the northern and southern cores. A more quantitative way of examining the effect of weathering processes on the different size fractions is to calculated ratios between T_{BE} and T_{DM}. Given that REE fractionation by weathering processes is minimal [e.g., *Blum and Erel,* 2003], the T_{BE}/T_{DM} ratio is mainly dominated by fractionation in Rb/Sr [e.g. *Davies et al.,* 1985; *McDermott and Hawkesworth,* 1990]. During times of enhanced chemical weathering associated with a wetter environment more ^{87}Sr is released into solution from the source rocks due to the preferential breakdown of Rb-rich phases such as mica and k-feldspar. This leads to a greater fractionation of Rb-Sr isotope systematics during more humid periods and to a lower T_{BE}/T_{DM} ratio in the sediments produced. Such systematic can be observed in core GeoB 9508 where T_{BE} ages are lowest during the AHP period for both size fractions. Additionally, the lowest T_{BE}/T_{DM} ratios are found in the AHP period for fine and coarse fractions. Calculated T_{BE}/T_{DM} ratios for the other four cores do not show such consistency. T_{BE}/T_{DM} ratios are higher during the AHP than during the REC and YD in the coarse fraction. Within the fine fraction no clear temporal variations can be resolved. This observation suggests that the combination of grain-size control of Rb/Sr and different aeolian and fluvial inputs does not always yield coherent behaviour in the Rb-Sr system. Core GeoB 9508 with the coherent variations in T_{BE}/T_{DM} is located in the vicinity of the Senegal River. The generally humid environment at this latitude and the continuous supply of fluvial matter would be expected to cause a lower T_{BE}/T_{DM} ratio due to a greater abundance of Rb-rich phases in the fluvial material. In contrast, the other cores record more complex Sr and Nd isotope systematics probably influenced by variations in the input of aeolian and fluvial material.

5. Conclusions

The Sr-Nd isotope records from different marine sediment cores along the NW African coast are used to document a detailed provenance and weathering record since the YD. Nd isotope ratios record minimal changes over time, indicating little change in the input of the different source materials and no significant change in the geological source area since the YD. By contrast, major variations in Sr isotope ratios indicate large changes in the humidity and rate of chemical weathering during the Holocene. The combined Sr-Nd isotope data indicate a latitudinal shift or an expansion of the African rainbelt and the associated wind belts causing changes in the evaporation/precipitation balance over NW Africa. While hyperarid conditions prevail during the YD, more humid conditions and intensified monsoonal rainfall characterize the AHP. In late Holocene times the monsoonal circulation diminished causing a return to arid conditions in NW Africa. In addition, our data clearly demonstrate that the isotopic ratio of $^{87}Sr/^{86}Sr$ is strongly influenced by grain size and that the isotopic ratio is generally higher in the fine fraction. As a result, investigations of bulk-sediment samples without grain-

size separations are hard to interpret. We recommend that grain-size separation is utilised in all studies of the geochemical and isotopic variation in detrital sediments. A further detailed investigation incorporating grain-size measurements and isotope analyses on mineralogically well-constrained sediments is required to improve our understanding of the influence of variations in the amount of dust and fluvial matter on the isotopic fractionation.

Acknowledgments

We thank Bas van der Wagt for measuring Nd-samples on the Neptune and ICP-MS measurements. Martijn Klaver is thanked for providing help with TIMS measurements. We thank Richard Smeets for all the help in the clean-lab with chemical procedures. This research was funded by the Deutsche Forschungsgemeinschaft (DFG) through the European Graduate College EUROPROX and MARUM – Center for Marine Environmental Sciences with additional funding from Europlanet. We thank Nathalie Fagel and an anonymous reviewer for helpful comments.

Supplementary Information

Material

The study is based on five marine sediment cores offshore Morocco, Mauritania, Western Sahara and Senegal. Exact positions are reported in Table 1. Based on published age models of the individual cores and downcore grain-size measurements three different time slices (REC, AHP and YD) were selected. Timing of the different time slices were chosen on distinct maxima and minima within the median grain-size record (log_{10} median grain sizes are shown in Fig.2), since our manuscript is not focused on the exact timing of the different time slices, but instead study the expression of the paleo-environmental conditions in the marine sediment cores.

Table 1. Core locations and sampling details

Core	Longitude (°W)	Latitude (°N)	Water depth (m)	Sampling depth (cm)	Age	Location	References Age models
GeoB 4223-2	12°28 W	29°01 N	775	1 43 131	0.45 4.33 11.60	off Agadir Canyon	*Freudenthal et al,* 2002
GIK 12379-1	18°75 W	23°14 N	2136	1 46 116	1.58 5.04 13.20	off Cape Barbas	*Sarnthein et al*, 1994
GeoB 7920-2	18°34 W	20°45 N	2278	8 58 173	0.82 5.31 12.34	off Cape Blanc	*Tjallingii et al, 2008*
GIK 13588-3	17°15 W	19°38 N	1000	1 49 157	1.38 5.08 12.43	off Banc d'Arguin	*Diester-Haaβ*, 1981
GeoB 9508-5	17°57 W	15°30 N	2384	8 48 123	0.99 4.69 11.83	off Senegal	*Mulitza et al, 2008*

In Table 2 the latitudinal position of the collected atmospheric dust samples are shown.

Table 2. Position of dust filter samples

Dust filter	Start	End	Location	Cruise	Reference
D1	24°55'75" N/ 16°53'12" W	20°16'47" N/ 17°55'08" W	off Morocco	M41/1	
D2	20°11'72" N/ 17°54'91" W	19°16'40" N/ 17°54'80" W	off Mauritania	M41/1	*Schulz et al*, 1998
D3	16°22'72" N/ 17°54'95" W	15°37'01" N/ 17°54'93" W	off Mauritania	M41/1	
D4	14°57'11" N/ 17°55'16" W	14°26'28" N/ 17°55'08" W	off Senegal	M41/1	

Transition between prevailing climate systems in NW Africa since the Younger Dryas

Inka Meyer[1], Jan-Berend W. Stuut[1,2], Christoph Vogt[1,3], Gareth R. Davies[4] and Holger Kuhlmann[1]

[1] MARUM- Center for Marine Environmental Sciences, Bremen, Germany
[2] NIOZ, Royal Netherlands Institute For Sea Research, The Netherlands
[3] Crystallography/ZEKAM, Geosciences, University of Bremen, Germany
[4] Department of Petrology, VU University Amsterdam, The Netherlands

Submitted to *Aeolian Research*

At present, two different climate systems are dominating the environmental conditions in NW Africa; the Mediterranean climate, which is linked to the North Atlantic climate regime with winter rains in the north, and the NW African monsoonal climate with summer precipitation in the south. These two climate regimes are separated by the Saharan Desert. In order to gain information about the latitudinal position of the transition zone between the monsoonal and the North Atlantic climate system throughout the Holocene, we investigated the terrigenous fraction of four marine sediment cores retrieved offshore the NW African coast between 30°N and 20°N. Grain-size measurements, combined with end-member modeling, show variability in sediment-transport mechanisms, which are directly related to the climate over NW Africa. Across the entire NW African continent the Younger Dryas is characterized by arid conditions and intensified trade winds. The Younger Dryas period is followed by climate shifts to wetter conditions during the mid-Holocene, associated with an increase in dust supply in late Holocene times, and towards the present-day prevailing arid climate. Superposed on this general trend, the northern part of NW Africa experienced short-lived and abrupt wet-dry alternations, related to the North Atlantic rain-bearing Westerlies. The transition zone between the two dominant climate systems shifted latitudinally throughout the Holocene. The investigation of the radiogenic isotopes of strontium and neodymium corroborate these findings. Here, we interpret higher $^{87}Sr/^{86}Sr$ ratios during the Younger Dryas as caused by changes in the source area of the terrigenous fraction from areas with generally more humid conditions, like the northernmost parts of the North African Mediterranean coast. We propose that the influence of the North Atlantic climate system reached at least down to 26°N during the Younger Dryas. During mid-Holocene times the boundary between both climate systems gradually shifted further north, possibly reaching as far North as 29°N.

Keywords: Holocene, climate regimes, transition

1. Introduction

The modern climate of NW Africa is influenced by two different climate systems, which are separated by the Saharan Desert [*Nicholson*, 2000]. The northernmost part of the continent is influenced by the Mediterranean climate system, which is dominated by the North Atlantic climate regime, where the west-east migration of cyclones cause winter rain [*Nicholson and Flohn*, 1980]. South of 20-24°N the NW African monsoonal system provides precipitation during summer [*Knippertz et al.*, 2003]. The main climatic driver of the region is the tropical rainbelt, which shows a seasonal variability. During boreal winter the core of the rainbelt is positioned at 5°N, whereas during boreal summer it lies at 20°N, following the seasonal migration of maximum insolation [*Nicholson*, 2000]. Besides these seasonal fluctuations it has been shown that the latitudinal position of the tropical rainbelt has changed over geological time scales, either by latitudinal movements [*Gasse and Van Campo*, 1994; *Gasse et al.*, 1990] or through expansion and contraction of the rainbelt [*Collins et al.*; 2010] causing variations in the hydrological conditions on land.

The aim of this study is to investigate the latitudinal shift of the transition zone between the Mediterranean climate system in the north and the monsoonal climate system in the

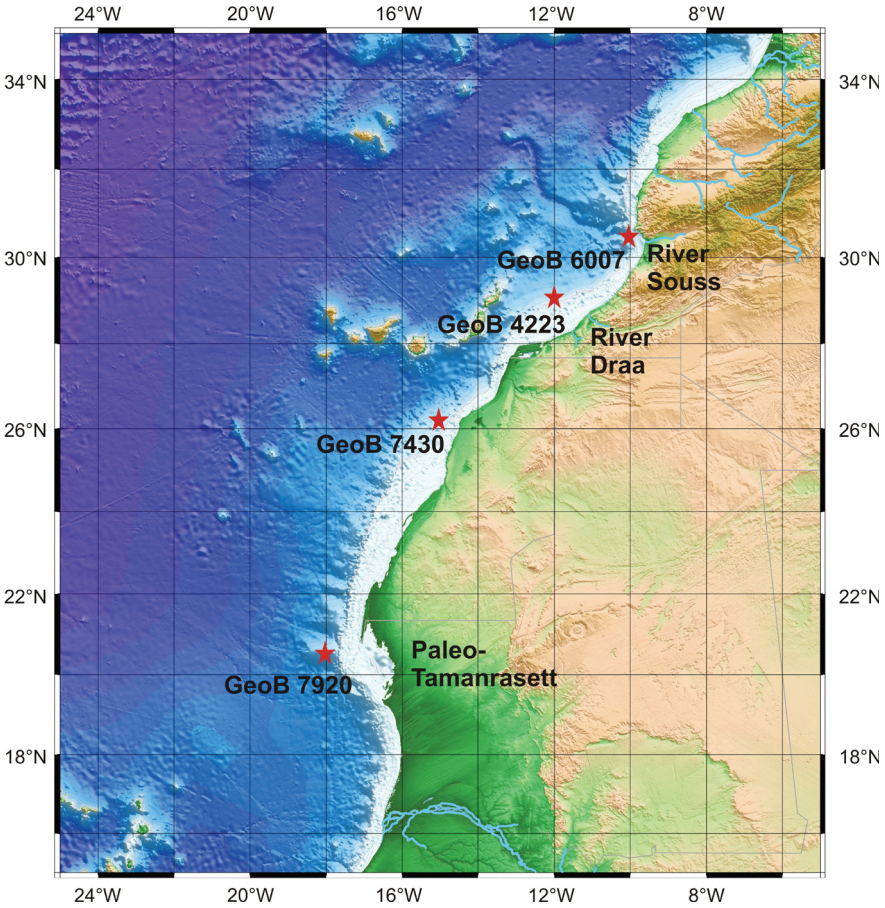

Fig.1.
Map with location of investigated deep-sea sediment cores offshore the NW African coast. Furthermore, several active river systems draining the Atlas Mountains as well as the Paleo-river system of the Tamanrasett are indicated.

south. For this purpose, four marine sediment cores offshore Morocco, Western Sahara and Mauritania, between 20°N and 30°N were studied (Fig.1). Grain-size measurements and end-member modeling were used to investigate the different sediment transport mechanisms, which are diagnostic of the input of land-derived sediments into the ocean and are related to environmental conditions in the sources of the sediments [*e.g. Stuut et al.*, 2002; *Prins and Weltje*, 1999; *Weltje and Prins*, 2003]. Furthermore, to investigate the provenance of the terrigenous fraction and to reconstruct the hydrological changes in the study area, the isotopic composition of $^{87}Sr/^{86}Sr$ and $^{143}Nd/^{144}Nd$ were analyzed on two different size fractions representing aeolian sediments (10-40 μm) and fluvial material (0-10 μm). These particular isotopes are indicative of chemical weathering, related to precipitation [Sr; e.g. *Jung et al.*, 2004; *Meyer et al.*, 2011/Chapter 5; *Weldeab et al.*, 2002], and geological origin [Nd; e.g. *Cole et al.*, 2009; *Jung et al.*, 2004], respectively. To verify differences in the mineralogical composition between both distinct size fractions, X-ray Diffraction (XRD) measurements were carried out. The combined investigation of these proxies allows conclusions about the latitudinal position of the different climate system within NW Africa during the Holocene and, in particular, the transition zone between these two dominant systems.

1.1. Terrigenous sedimentation offshore NW Africa

The terrigenous fraction deposited in marine sediments consists of a mixture of sediment populations derived from different sources and which are transported to the site of deposition by different sediment transport mechanisms [*Weltje and Prins*, 2003]. Offshore the Saharan Desert mainly two types of terrigenous matter can be found: first, and most dominant, aeolian input, and secondly fluvial supply. Today the Sahara is one of the most arid places in the world and therefore the most important source of mineral dust supplied to the Atlantic Ocean [e.g. *Harrison et al.*, 2001]. Approximately 50-70% of the global dust emission supplied to the world's oceans is derived from the Saharan Desert [*Goudie and Middleton*, 2001; *Mahowald et al.*, 2005]. The modern dust production rate of the Sahara is estimated to be around 700-900 x 10^6 tons aeolian dust per year [*Goudie and Middleton*, 2006]. The particle size of the transported dust is a function of the distance from source to sink and altitude at which the particles are transported [*Stuut et al.*, 2005]. Saharan dust samples collected in the Caribbean are less than 5 μm in size [*Talbot et al.*, 1986], and Saharan aerosols collected on Tenerife at 2000 m altitude likewise consists of particles <5 μm [*Torres-Padrón et al.*, 2002]. Contrary, proximal aeolian dust from the Cape Verde Islands contain grains up to 90 μm in diameter [*Glaccum and Prospero*, 1980]. *Stuut et al.* [2005] detected particle sizes generally larger than 10 μm in modern atmospheric dust samples collected off Senegal and Mauritania. Next to the aeolian input, terrigenous sediments are supplied by rivers into the Atlantic Ocean. The total discharge of suspended sediment by NW African rivers into the Atlantic Ocean is

estimated to be 110 × 10^6 tons/year in modern times, which represents a factor ten less than the aeolian dust supply in the area [*Hillier*, 1995]. The modern fluvial input in our study area is restricted to perennial river systems in Morocco, like the Sebou and the Souss Rivers, draining the Atlas Mountains [*Summerhayes et al.*, 1976; *Wynn et al.*, 2002]. South of ~29°N the fluvial supply is limited, most wadis reach the Atlantic only seasonally [e.g. *Wynn et al.*, 2002]. Although NW Africa is presently a dry region, several humid phases occurred in the geological past [e.g. *deMenocal et al.*, 2000a; *Tjallingii et al.*, 2008]. Paleo-river systems, like the Tamanrasett River system, were detected based on topographic patterns [*Vörösmarty et al.*, 2000]. This system must have carried vast amounts of fluvial sediments to the Atlantic Ocean, considering the reconstructed African humid periods [*deMenocal et al.*, 2000a; *Tjallingii et al.*, 2008]. Fluvial suspension load reaching offshore regions is generally much finer in particle size than proximal aeolian particles. Grain-size measurements of fluvially transported sediments offshore major rivers in different sedimentary basins showed that the suspended sediment load is generally smaller than 10 μm [*Weltje and Prins*, 2003]. Similar results were obtained by Gac and Kane [1986] who detected 95% of the suspended sediment load of the Senegal River to be smaller than 10 μm.

Grain-size measurements of the terrigenous fraction deposited in deep-sea sediments forms a powerful tool to investigate the hydrological and climatic changes on the continent at different temporal and spatial scales [*Sarnthein et al.*, 1982; *Stuut et al.*, 2002; *Tjallingii et al.*, 2008]. Downcore measurements of marine sediment cores from offshore NW Africa demonstrate a temporal change in the amount of fluvial and aeolian input, with an increase of fluvial supply during humid periods [e.g. *Tjallingii et al.*, 2008]. Conversely, during arid periods the amount of wind- blown material is higher than the fluvial supply [e.g. *Mulitza et al.*, 2008] and it was demonstrated that there is a linear relationship between precipitation in the source area and the dust flux from that source [*Mulitza et al.*, 2010]. The combination of grain-size analyses, end-member modeling and mineralogical investigations has been demonstrated to be able to distinguish between the different transport mechanisms of terrigenous sediments related to the environmental conditions in the source areas of the sediments [*Holz et al.*, 2004; *Nizou et al.*, 2010; *Prins and Weltje*, 1999; *Stuut and Lamy*, 2004; *Tjallingii et al.*, 2008; *Weltje and Prins*, 2003].

2. Material and methods

This study was performed on four deep-sea sediment cores collected on the NW African continental margin between 20°N and 30°N. Exact positions of the sediment cores can be found in Table 1. Sediment cores are located under the northern fringe of the modern Saharan dust plume and partly in the vicinity of (paleo-) river systems. The deep-sea sediment cores (water depth between -775 and -2278 m) were recovered during several cruises of the research vessels "*Meteor*" and "*Poseidon*" between 1996 and 2002.

Table 1. Core locations (in decimal) and references for age models

Core	Longitude	Latitude	Depth in m	Intervall	Locations	References for Age model
GeoB 6007-2	10°26´83 W	30°85´00 N	-900	LH AHP YD	off Cape Ghir	*Kuhlmann et al.,* 2004a
GeoB 4223-2	12°28´00 W	29°01´00 N	-775	LH AHP YD	off Agadir Canyon	*Freudenthal et al.,* 2002
GeoB 7430-3	15°15´00 W	26°38´33 N	-1165	LH AHP YD	off Cape Bojador	*Meggers et al.,* 2001
GeoB 7920-2	18°34´90 W	20°45´09 N	-2278	LH AHP YD	off Cape Blanc	*Tjallingii et al.,* 2008

2.1. Grain-size analyses and end-member modeling

To isolate the terrigenous fraction from the marine components, samples were pre-treated with different chemicals to remove organic material (H_2O_2), calcium carbonate (HCl) and biogenic silica (NaOH), respectively. To verify if all components were removed successfully, microscope analyses were carried out on randomly chosen single samples. For details of chemical pre-treatment steps see *Mulitza et al.*, [2008].

Continuous grain-size records were obtained for the entire Holocene since the Younger Dryas by sampling the four sediment cores in varying temporal resolutions. Cores GeoB 4223 and GeoB 7430 were sampled every cm, core GeoB 6007 every two cm and core GeoB 7920 every 5 cm. Grain-size distributions were determined with the Laser Diffraction Particle Size Analyser (Beckman Coulter) LS200 resulting in 92 size classes from 0.4-2000 µm. To avoid the potential disturbance of particle-size analyses by gas bubbles, measurements were done using demineralised and degassed water. All pre-treatments and the grain-size measurements were carried out in the laboratories at MARUM, Bremen.

In order to recognize distinct sediment sub-populations within the grain-size distributions, the numerical-statistical end-member algorithm EMMA was applied [*Weltje*, 1997]. The end members were chosen based on the goodness-of-fit statistics by calculating the coefficient of determination (r^2). This coefficient describes the proportion of the variance of each grain-size class that can be replicated by the estimated data. Hence, the eventual outcome of the model is a statistically unique solution with end members that represent real particle-size distributions. For more details of the application of the model to particle-size distributions, see [*Weltje and Prins*, 2003].

2.2. Isotope analysis

The ratio between ^{87}Sr (produced by the radioactive decay of ^{87}Rb in rocks or minerals) and ^{86}Sr (not formed by radioactive decay and constant over time) can be used to identify

changes in the evaporation/precipitation balance as well as in the intensity of chemical weathering in the sediment source [e.g. *Cole et al.*, 2009; *Jung et al.*, 2004]. The ratio between ^{143}Nd (produced by the radioactive decay of ^{147}Sm) and the stabile isotope ^{144}Nd can be used as an indicator of the geological origin of the sediment [*Blum and Erel*, 2003; *Fagel et al.*, 2002; *Goldstein and O'Nions*, 1981]. It has been shown that the isotopic composition of $^{87}Sr/^{86}Sr$ varies with grain size [*Dasch*, 1969; *Feng et al.*, 2010; *Meyer et al.*, 2011/Chapter 5], resulting in an increase of $^{87}Sr/^{86}Sr$ with decreasing grain size. Contrary, Nd isotope ratios are hardly affected by sorting and more accurately reflect the average age of the continental sources [*Goldstein et al.*, 1984]. As a result, investigations of bulk sediment samples without grain-size separations are hard to interpret in terms of environmental conditions in the source area of the sediments. To overcome this grain-size problem, isotopic investigations were done on two distinct size fractions. Based on the prevailing sediment-transport mechanisms and published end-member modeling studies [*Tjallingii et al.*, 2008] we separated our terrigenous fraction into two size classes. The fine fraction (0-10 μm) is interpreted to represent fluvial input, and the coarse fraction (10-40 μm) is interpreted to be dominated by aeolian material. Grain-size separation was performed at the Atterberg laboratory (University of Bremen) in settling tubes using Stoke's Law.

Isotopic analyses were done on three time slices of contrasting climate conditions within NW Africa: I) late Holocene = LH, II) African Humid Period = AHP and III) Younger Dryas = YD. We recognize that the reduction of each time period to only one sample per time slice is a considerable simplification. However, each of these samples has been chosen carefully using the individual age models (see Table 1) as well as minima and maxima observed in the grain-size measurements and end-member modeling results.

Sample preparations for isotopic measurements were performed in a "class-100" clean laboratory at the VU University Amsterdam. In order to dissolve all authigenic, biogenic carbonate, and absorbed marine Sr-Nd signals, all samples were leached with 1*N* HCl and the dissolved fraction discarded before digestion. Subsequently, samples were dissolved in a mixture of HF-HNO_3-HCl. In order to dissolve any possible refractory phases e.g. zircon, the coarser fraction (> 10 μm) were dissolved in Teflon-lined acid digestion bombs. Two international standards (BHVO-2 and MAG-1, USGS) were also included in the process. Values for standard BHVO-2 gave a value of 0.703488 ± 0.000007 (2σ; n=5) for $^{87}Sr/^{86}Sr$ and 0.512987 ± 0.000005 (2σ; n=3) for $^{143}Nd/^{144}Nd$. Standard MAG-1 gave a value of 0.722638 ± 0.000009 (2σ; n=3) for $^{87}Sr/^{86}Sr$ and 0.512070 ± 0.000008 (2σ; n=2) for $^{143}Nd/^{144}Nd$.

An aliquot of the residue fractions from each sample was used for the investigation of Sr isotope ratios. Sr was isolated using SrSpec resin (Eichrom, USA). $^{87}Sr/^{86}Sr$ ratios were determined using a MAT 262 Thermal Ionisation Mass Spectrometer (TIMS) at the VU Amsterdam. Samples were loaded onto single rhenium filaments and measured in static mode. $^{87}Sr/^{86}Sr$ ratios were corrected for

mass fractionation by normalizing to $^{86}Sr/^{88}Sr$ = 0.1194. Measured values for international standard NBS 987 gave average values of $^{87}Sr/^{86}Sr$ = 0.710241 ± 0.000007 (2σ, n=8). Blanks analyzed along with the samples yield < 200 pg so that blank contribution to the analysis can be neglected.

Nd was extracted using TRU resin and HDEHP-columns. Nd isotopic compositions were obtained using a ThermoFinnigan Neptune multiple-collector inductively-coupled-plasma magnetic-sector mass-spectrometer (MC-ICP-MS). The international standard CIGO was used to monitor the performance of the Neptune. Measured CIGO gave average values of $^{143}Nd/^{144}Nd$ = 0.511342 ± 0.000004 (2σ, n=10). Results are expressed as the ratio of $^{143}Nd/^{144}Nd$ and as ε_{Nd} (0) = (($^{143}Nd/^{144}Nd$/0.512636)-1) × 10^4 using the present-day "chondritic uniform reservoir" (CHUR) value = 0.512636 [*Jacobsen and Wasserburg*, 1980; *Weldeab et al.*, 2002]. Concentrations of trace elements of each sediment size-fraction were measured by a Quadrupole Thermo X-Series II inductively coupled plasma mass spectrometer (ICP-MS).

2.3 Mineralogical analyses

Single size fractions of all time slices were finely grounded and analyzed for their mineralogical compositions on a Philips X'Pert Pro multipurpose diffractometer with Cu radiation and fixed divergence slit (1/4°) at the Crystallography Department of Geosciences, University of Bremen. Samples were prepared with the standardized Philips/Panalytical backloading system, which

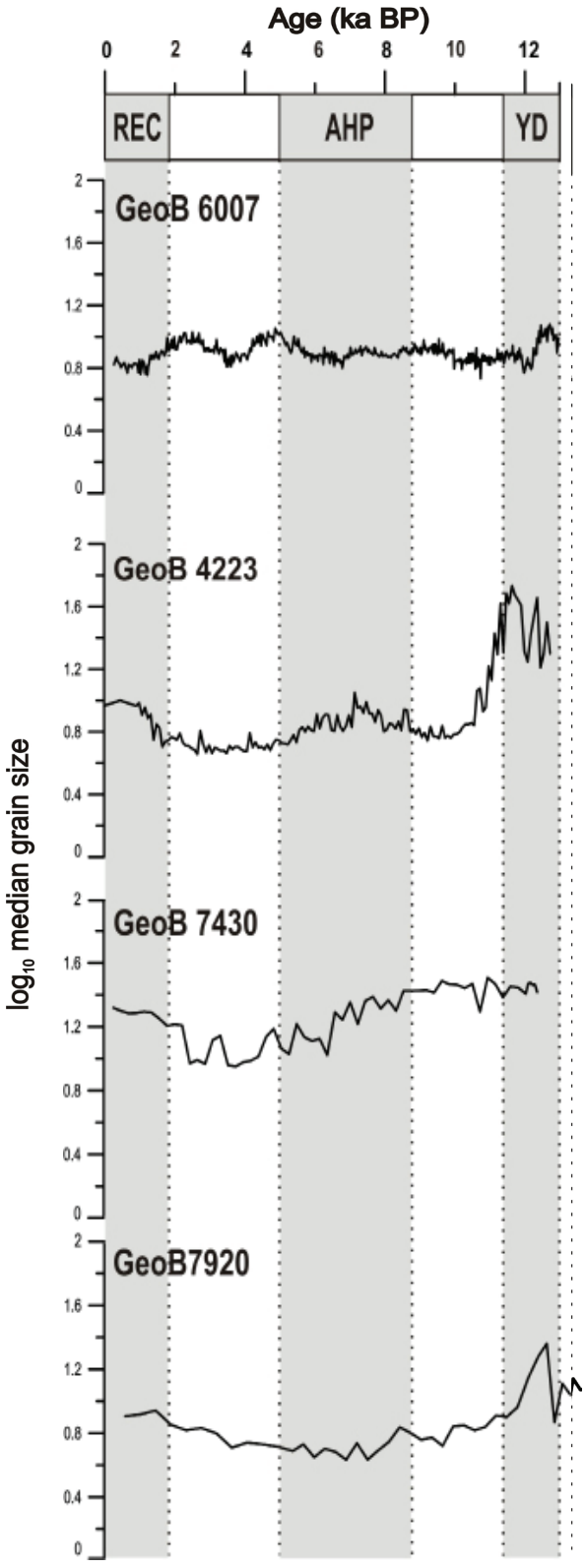

Fig.2. Log-ratios of the median grain sizes of studied cores are calculated relative to a basis of 10 (log_{10}) and plotted against sedimentary age. Grey bars are defined time slices of the late Holocene (LH), the African Humid Period (AHP) and Younger Dryas (YD).

provides an almost random distribution of the particles. Mineral identification was done using the full pattern method (QUAX) [*Vogt et al.*, 2002].

3. Results

3.1. Grain-size distributions and end-member modeling

Due to a huge variability in grain-size distributions between single cores, $\log_{10}$ ratios were used for the comparison of sediment cores GeoB 6007, GeoB 4223, GeoB 7430 and GeoB 7920 (Fig.2) Hence, differences are a lot smaller than plotting the median grain size. However, there is a clear contrast between the periodic variations in the median grain size of core GeoB 6007 compared to the three other cores. This can only partly be attributed to the higher frequency at which this core was sampled and the higher average sedimentation rates, of ~85 cm per thousand years, observed at this site. In all three cores the YD yield coarsest grain sizes (~53 µm for GeoB 4223, ~20 µm for GeoB 7430 and ~14 µm for GeoB 7920). During the AHP finest grain sizes are found (~6 µm for GeoB 4223, ~10 µm for GeoB 7430 and ~5 µm for GeoB 7920). The LH period yields coarser material again (~10 µm for GeoB 4223, ~20 µm for GeoB 7430 and ~8 µm for GeoB 7920).

Since the terrigenous fraction in marine sediments can be provided by different transport mechanisms and supplied from various sources, the grain-size distribution may show a polymodal shape. Therefore, the end-member-modeling algorithm (EMMA) was used to split-up the grain-size distributions in discrete size populations [*Weltje*, 1997]. The statistically evident end-members were calculated for each sediment core. Each end member represents a group of particles of a similar sediment production and/or transport processes [e.g. *Tjallingii et al.*, 2008; *Weltje*, 1997; *Weltje and Prins*, 2003]. Calculated end-member proportions for each core are shown in Fig.3. For each core the coefficient of determination (r^2) is computed to identify the minimal number of end-members necessary for a good statistical interpretation. For all cores an end-member model with three independent sub-populations was chosen to represent the optimal balance between statistical description of the variance in the data set and complexity of mixture composition. Using the three end-member model, the mean coefficient of determination (r^2_{mean}) is at least 0.7 for each core (GeoB 6007= 0.7; GeoB 4223= 0.9; GeoB 7430= 0.8; GeoB 7920= 0.9) which means that on average at least 70% of the variance in each grain-size class can be reproduced. EM3 is the coarsest end member in all cores. The modal size of EM3 is ~50 µm for core GeoB 6007, ~53 µm for GeoB 4223; ~24 µm for GeoB 7430 and ~55 µm for core GeoB 7920. EM2 is the mid-size end member and yields a mode of ~12 µm for core GeoB 6007, ~25 µm for GeoB 4223, ~14 µm for GeoB 7430 and ~ 38 µm fore core GeoB 7920. EM1 is the finest end member in all cores, with ~4 µm for GeoB 6007, ~4 µm in core 4223, ~6 µm in core GeoB 7430 and ~5 µm in GeoB 7920.

Table 2. Isotopic ratios of strontium, neodymium and mineralogical composition of investigated samples. Isotopic values for GeoB 4223 and GeoB 7920 were obtained from Meyer et al., 2011.

Core	Period	Fraction	$^{143}Nd/^{144}Nd$ ($\pm$ 2σ x 10^{-6})	ε_{Nd}	$^{87}Sr/^{86}Sr$ ($\pm$ 2σ x 10^{-6})	quartz (%)	plagioclase (%)	k-feldspar (%)	montm. & smec.	illit & micas
GeoB 6007	LH	0-10 µm	0.512052 (11)	-11.3	0.723989 (09)	13.7	4.9	1.6	7.7	37.8
GeoB 6007	AHP	0-10 µm	0.512044 (08)	-11.5	0.719899 (10)	13.6	7.1	1.4	5.7	41.7
GeoB 6007	YD	0-10 µm	0.512072 (12)	-11.0	0.719643 (10)	13.6	3.3	1.0	4.3	39.9
GeoB 6007	LH	10-40 µm	0.511983 (10)	-12.7	0.720010 (18)	44.0	20.9	4.7	1.0	15.0
GeoB 6007	AHP	10-40 µm	0.512032 (14)	-11.8	0.716788 (09)	42.1	27.8	8.4	0.9	9.6
GeoB 6007	YD	10-40 µm	0.512988 (12)	-12.6	0.719078 (09)	45.2	18.9	8.4	0.0	21.0
GeoB 4223	LH	0-10 µm	0.512058 (12)	-11.3	0.716003 (09)	- -	- -	- -	- -	- -
GeoB 4223	AHP	0-10 µm	0.512042 (12)	-11.6	0.713654 (07)	- -	- -	- -	- -	- -
GeoB 4223	YD	0-10 µm	0.512028 (12)	-11.9	0.712549 (12)	- -	- -	- -	- -	- -
GeoB 4223	LH	10-40 µm	0.512071 (14)	-11.0	0.716460 (09)	- -	- -	- -	- -	- -
GeoB 4223	AHP	10-40 µm	0.512053 (08)	-11.4	0.710725 (08)	- -	- -	- -	- -	- -
GeoB 4223	YD	10-40 µm	0.511993 (11)	-12.6	0.721564 (10)	- -	- -	- -	- -	- -
GeoB 7430	LH	0-10 µm	0.512060 (10)	-11.2	0.715154 (08)	12.2	5.2	2.8	7.6	41.5
GeoB 7430	AHP	0-10 µm	0.512024 (09)	-11.9	0.712560 (07)	12.9	5.4	2.6	7.4	40.7
GeoB 7430	YD	0-10 µm	0.512031 (12)	-11.8	0.711401 (13)	13.1	4.0	2.4	8.2	40.7
GeoB 7430	LH	10-40 µm	0.512186 (09)	-8.8	0.720221 (09)	53.7	18.2	5.7	1.1	5.1
GeoB 7430	AHP	10-40 µm	0.512015 (06)	-12.2	0.714433 (07)	47.2	21.7	9.0	2.4	7.0
GeoB 7430	YD	10-40 µm	0.511964 (08)	-13.1	0.713909 (08)	55.0	17.2	12.8	0.8	2.8
GeoB 7920	LH	0-10 µm	0.511876 (14)	-14.8	0.729342 (08)	12.7	5.0	1.7	8.9	37.4
GeoB 7920	AHP	0-10 µm	0.511925 (09)	-13.9	0.723640 (08)	12.2	5.3	1.8	8.6	42.8
GeoB 7920	YD	0-10 µm	0.511869 (10)	-15.0	0.729979 (10)	11.7	4.4	3.8	9.9	33.7
GeoB 7920	LH	10-40 µm	0.511942 (08)	-13.5	0.718066 (09)	44.9	16.4	2.6	0.0	18.7
GeoB 7920	AHP	10-40 µm	0.511843 (09)	-15.4	0.717148 (10)	38.6	26.7	4.2	0.0	10.7
GeoB 7920	YD	10-40 µm	0.511795 (08)	-16.4	0.727354 (09)	53.7	19.4	4.4	1.0	3.0

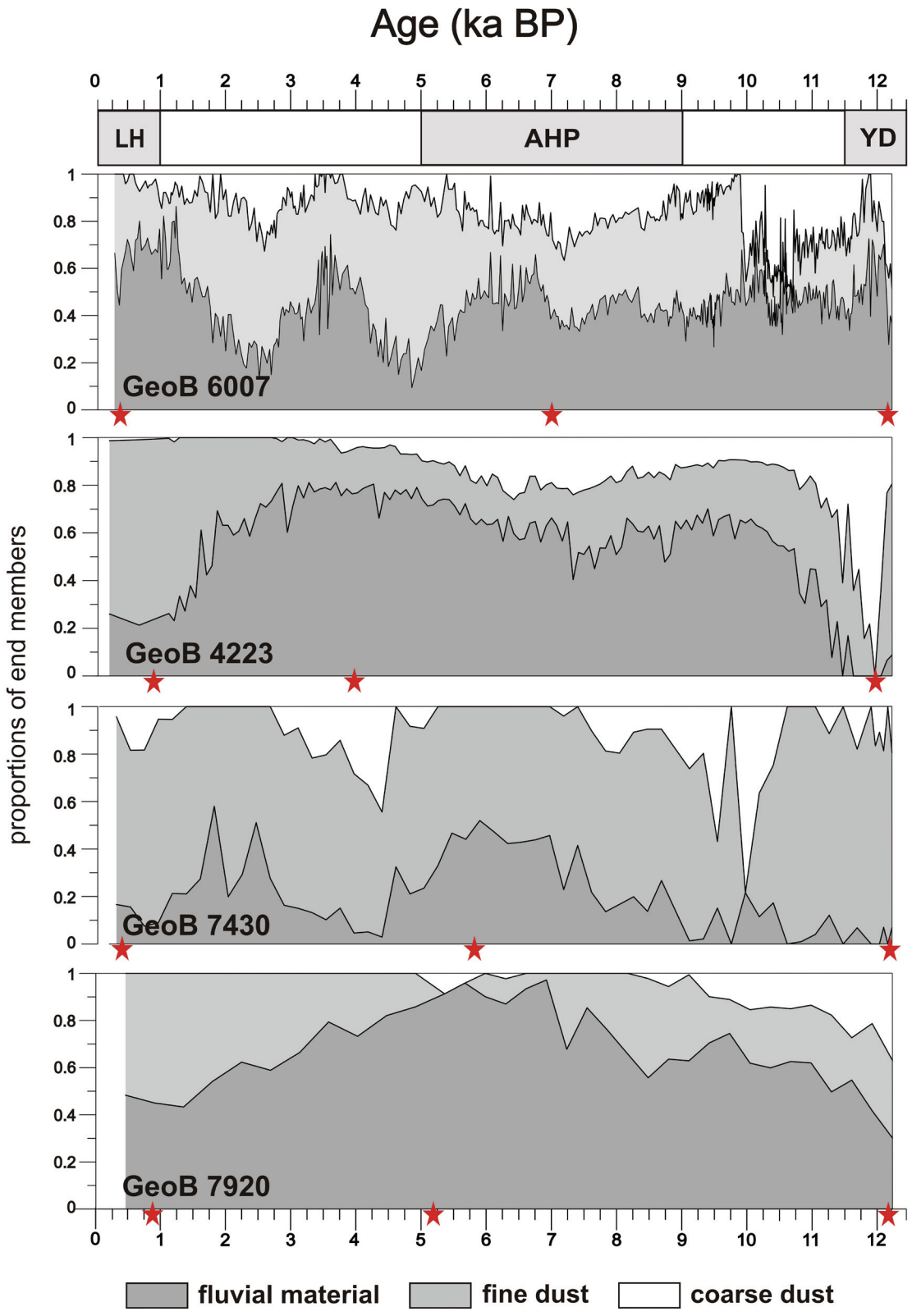

Fig.3.
End-member proportions for all investigated sediment cores, plotted against sedimentary age. Red stars display sample depth for measurements of strontium and neodymium. Note that sample depth for isotopic analysis are not predominantly chosen based on the age models but on the minima and maxima of grain-size measurements and end-member modeling results.

3.2. Isotopes

All measured isotopic values are reported in Table 2 and Fig 4. Analyzed values of Nd range between ε_{Nd} -8.8 and -16.4 in total. In the three northern cores GeoB 6007 (30°N), GeoB 4223 (29°N) and GeoB 7430 (26°N) ε_{Nd} values are similar (ε_{Nd}~ -11.8). The only exception is the coarse LH value in core GeoB 7430 (ε_{Nd} -8.8). Contrary, ε_{Nd} ratios for core GeoB 7920 are lower with ε_{Nd}~ -14.8. $^{87}Sr/^{86}Sr$ ratios show more variability (see Table 2). In the three northern cores GeoB 6007, GeoB 4223 and GeoB 7430 $^{87}Sr/^{86}Sr$ ratios for the fine fraction yield lowest values during the YD. Isotopic values for the LH period are highest and values for the AHP are in between them. In the more southerly core GeoB 7920 (21°N), lowest values are indicated for the AHP, followed by the LH value and with highest $^{87}Sr/^{86}Sr$ ratios during the YD. $^{87}Sr/^{86}Sr$ ratios for the coarse fraction are more complex. Core GeoB 7430 has lowest values for the YD, followed by the AHP and LH. In cores GeoB 6007, GeoB 4223 and GeoB 7920 lowest values are found in the AHP. In core GeoB 4223 and GeoB 7920 the YD has highest values, whereas in GeoB 6007 highest values occur during the LH.

3.3. Mineralogical analyses

XRD measurements on the single size fractions indicate a general difference between samples of the coarse fraction (10-40 µm) and samples from the fine fraction (0-10 µm) as shown in Table 2. The most important minerals in the 10-40 µm fraction are quartz (~47 %), plagioclase (~21%) and k-feldspars (~7%). Only smaller amounts of montmorillonite and smectite (~1 %) as well as illite and micas (~9 %) are detected. Contrary, samples from the 0-10 µm fraction are dominated by illite and micas (~42 %). Further important minerals in the fine fraction are quartz (~18 %), montmorillonite and smectite (~8 %), plagioclase (~7 %) and k-feldspar (~2 %).

4. Interpretation and discussion

4.1. Grain size data

Sediment cores GeoB 4223, GeoB 7430 and GeoB 7920 reveal a similar trend in median grain size variations over the last ~12 ka, with coarsest particle sizes during the YD. We interpret the increase in median grain size during the YD to represent higher wind speed and/or less vegetation cover within NW Africa. After the termination of the YD a decrease in median grain size can be observed in the three cores. The decrease in median grain size is caused by the deposition of finer material, which points to changes in the hydrological conditions in the source area and/or changes in vegetation cover. In late Holocene times (LH) the median grain size increases considerably in all three cores. This is interpreted as a transition to modern arid conditions prevailing within NW Africa. Thus, the variations in the median grain sizes of the terrigenous fraction of marine sediments offshore NW Africa can be used as a proxy for the climate variations during the Holocene. Contrary to the described grain-size variations found in the three southern cores, between 20° and 27°N, the median grain size of the northernmost core

GeoB 6007 (30°N) is characterized by a high-frequency oscillation. This oscillation cannot be explained by the same climatic changes causing the variations in the median grain size of the other cores.

4.2. End-member modeling

Using the end-member modeling algorithm (EMMA) we are able to distinguish between the dominant transport mechanisms at every single core location and to verify changes in the amount of fluvial transported versus wind-blown material. In all end-member models EM3 represents the coarsest end member, followed by the mid-sized EM2. Both coarser end members of the three end-member models are interpreted to represent aeolian dust, where EM3 is composed of 'coarse' aeolian dust, and EM2 represents the 'fine' aeolian particles. Our interpretation is supported by different studies detecting aeolian particles larger than 10 µm [e.g.,*Stuut et al.*, 2005]. EM1 is significantly finer in all cores. We suggest that the finest end member is dominated by the fluvial sediment fraction. Again, our interpretation is in line with other studies on grain sizes of fluvial material [*Gac and Kane*, 1986; *Holz et al.*, 2004; *Weltje and Prins*, 2003]. However, large differences between the sizes of the end members are detected. Those variations can be caused by a number of facts, like e.g. differences in the distance between the continent and each core location, differences in source material or topographic features.

Core GeoB 6007 is located under the edge of the prevailing dust plume, transporting aeolian particles from the African continent to the Atlantic Ocean. Furthermore, the core is located near the Souss River which drains the Atlas Mountains year-round but with highest intensities during boreal winter [*Summerhayes et al.*, 1976; *Wynn et al.*, 2002]. As indicated in the median grain-size record of GeoB 6007 clear millennial-scale variations are observable. This millennial-scale oscillation is also represented in the end-member record (Fig. 3). The most important end member is the fluvial fraction, supplied by the Souss River. During the YD the amount of coarse and fine dust is slightly increased (28% in total), although fluvial material is still the dominating end member (72%). In the course of the Holocene the fluvial fraction displays regular oscillations with highest values at 6 ka, 3 ka and 0.7 ka.

The interpretation of the end-member record for core GeoB 4223 is very different. Near the core location the River Draa and several wadis fed by the Atlas Mountains reach the Atlantic Ocean only seasonally under modern arid conditions [*Summerhayes et al.*, 1976]. During the YD the dust end-member increases up to 98%, but decreases considerably after its termination. During the mid-Holocene the record is clearly dominated by the fluvial end-member. Possibly a denser vegetation cover diminished the aeolian transport during the mid-Holocene. Since the last 2 ka a constant decrease in the fluvial end member, down to only 2%, and at the same time an increase to in the fine dust 74% is observed, reflecting the modern dry conditions.

In core GeoB 7430 the interpretation of the end members is not as straightforward. First of all, the median grain sizes are smaller than in

the other cores. Despite this, there is obviously a dominance of fine dust (83%) during the YD and only little riverine input at the same time (5%). The fluvial material increases with the beginning of the early Holocene reaching 50% during the AHP. This observation corroborates the hypothesis of humid conditions and an increase in vegetation cover in NW Africa during early to mid-Holocene. Due to the fact that no river system is detectable within the vicinity of the core location, the amount of the fluvial portion is limited compared to the other cores. The record is interrupted by several abrupt peaks in the coarse dust fraction at around 10 ka, 9.5 ka and 4.5 ka, which possibly reflect short-term dry spells or other sedimentary processes. During the late Holocene a decrease of the fluvial end-member and a contemporaneous increase in the fine dust fraction up to 72% is visible in the core. This is interpreted as a return to more arid conditions within NW Africa, and is in line with the other cores.

The trend of higher amounts of coarse dust during the YD, an increase in fluvial supply during the AHP and a dominance of fine dust during present-day conditions is detected in core GeoB 7920 as well. This sediment record is again governed by a fluvial sediment fraction, making 76% of the sediment during the AHP. Although presently there is no river system located next to the core site, a huge paleo-river structure, the Tamanrasett River system, was reconstructed based on topographic patterns [*Vörösmarty et al.*, 2000]. This huge paleo-river-system most likely also created the Timiris Canyon [*Krastel et al.*, 2004]. The coarse dust fraction is only visible during the YD with an amount of 33%. During the LH the fine dust portion is dominating (53%).

4.3 Isotope data

The isotopic values for ε_{Nd} and $^{87}Sr/^{86}Sr$ are plotted in Fig. 4. Since the isotopic composition of Nd is largely unaffected by weathering processes and sedimentary sorting [*Frank*, 2002; *Goldstein et al.*, 1984] we use ε_{Nd} as a provenancing tool for the terrigenous fraction found in the marine sediment cores from the NW African continental margin, between 20° and 30° N. A distinctly higher value is observed in the coarse LH sample of core GeoB 7430 with a value of ε_{Nd} -8.8. This value is most likely caused by a volcanic imprint from the Canary Island. The Canary Archipelago (27-29° N and 13-18° W) is a group of young volcanic islands 600 km off the NW African coast. Most of the islands are still active and several volcanic eruptions occurred within the last 5000 years [*Schmincke*, 1982]. *Hoernle et al.* [1991] studied the isotopic composition of Nd in several lava flows and dikes. Due to the young volcanic material they found very high Nd isotopic ratios of ε_{Nd} between +1.2 and +6.7. Since the Canary Current flows offshore the NW African coast in an equatorward direction it is possible that material derived from the volcanic islands is transported southward to the core site of GeoB 7430. A mixture between volcanic matter with material from the African continent can explain the value of ε_{Nd} -8.8 in the coarse LH sample of core GeoB 7430.

Furthermore, a shift from higher ε_{Nd} values in the northern cores to lower ε_{Nd} values in the

southern core GeoB 7920 is shown. Regarding the possible sources of the sediment (Fig. 4), it becomes clear that a substantial amount of the sediment must originate from the Atlas Mountains which were formed in several phases of earth's history [e.g. *Ennih and Liegeois*, 2008]. The last period of tectonic deformation occurred during the Late Cretaceous-Cenozoic (~65 Ma) when Africa and Eurasia started colliding [*Wright et al.*, 1985]. In contrast, the unradiogenic ε_{Nd} values of core GeoB 7920 point to the very old Archaean basement rocks of the West African Craton [~2.0 Ga; *Lecorche et al.*, 1991; *Potrel et al.*, 1996]. In general, measured ε_{Nd} values fit well with the ε_{Nd} zonal distribution maps of Grousset et al [1998], who demonstrated only minor changes in the ε_{Nd} distribution maps of Last Glacial Maximum compared to modern values, supporting our interpretation of minimal changes in provenance throughout the Holocene.

Variations in the isotopic ratio of $^{87}Sr/^{86}Sr$ were used to gain information about the hydrological conditions in the study area since the YD. Since our study is done on two distinct size fractions a possible fractionation in the $^{87}Sr/^{86}Sr$ isotopic ratios was eliminated. Surprisingly, $^{87}Sr/^{86}Sr$ isotopes of the fine fraction yield lower values during the YD, indicating a more humid signal in the three northernmost cores GeoB 6007, GeoB 4223 and GeoB 7430 compared to the AHP or the LH. In all three northern cores the AHP is slightly drier than the YD and driest conditions can be found during the late Holocene time slice (LH). Contrary to the three northern cores the southernmost core GeoB 7920 shows an opposite trend. Wettest conditions occurred during the AHP, followed by a drier

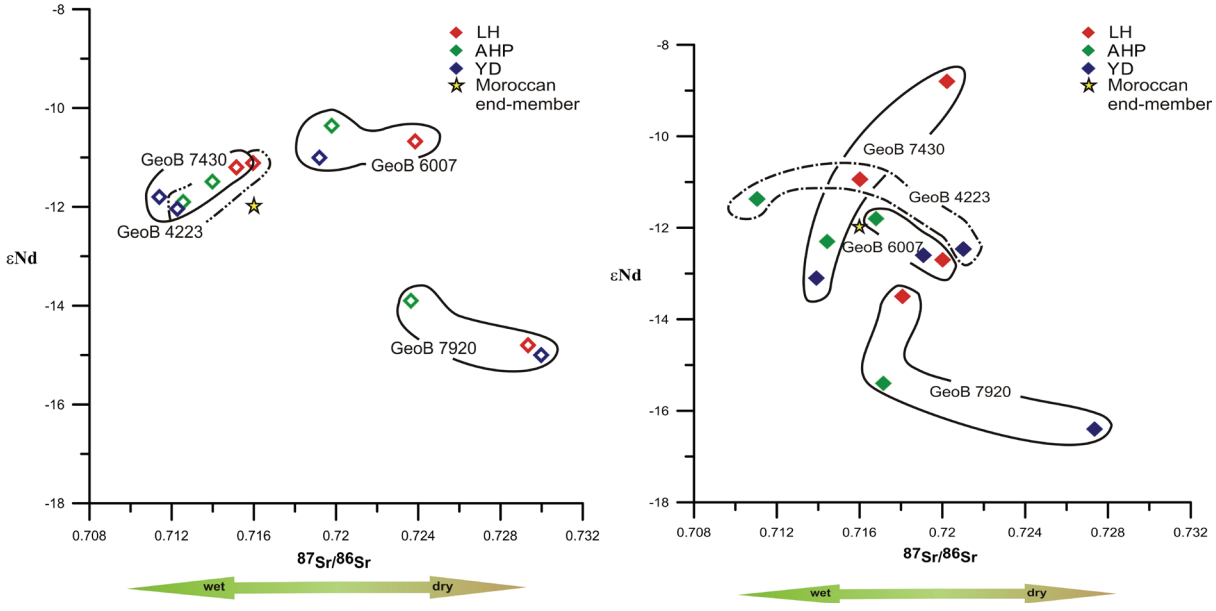

Fig.4.
A comparison between the isotopic compositions of $^{87}Sr/^{86}Sr$ and ε_{Nd} for the fine (left) and the coarse fraction (right). The figure shows the distinctions between the two geological source regions, the Atlas Mountains and the old West African Craton. Sr isotopes of the fine fraction of the three northern cores indicate more humid conditions during the YD, in contrast to the core GeoB 7920. To define possible end members, data from dust source regions on land are included (see *Grousset et al*, [1998]).

environment during the LH and a most arid environment during the YD. The systematic of the southern core was found in a previous study of marine sediment cores offshore Mauritania and Senegal as well [*Meyer et al.*, 2011/Chapter 5], and is explained in terms of zonal movements of the northern boundary of the tropical rainbelt throughout the Holocene [e.g. *Mulitza et al.*, 2008, *Collins et al.*, 2010]

4.4. Mineralogical composition

The mineralogy shows grain-size dependence between both fractions. The coarse fraction is generally enriched in quartz and plagioclase whereas the fine fraction is enriched in clay minerals and micas. This fits well with other publications defining aeolian dust as predominantly composed of quartz, plagioclase and k-feldspars [e.g. *Glaccum and Prospero*, 1980; *Nizou et al.*, 2010]. Furthermore, this observation demonstrates once more the strength of our approach of separating the sediments into two size fractions; bulk analyses would have led to dampened changes that would predominantly caused by variations in mixing proportions of the two size fractions rather than environmental or provenance changes [*Meyer et al.*, 2011/Chapter 5]. In the coarse fraction the YD samples contains highest amounts of quartz and k-feldspar, supporting our hypothesis of stronger winds during the YD. In contrast, AHP samples contain less quartz in the coarse fraction. The mineral composition of the fine fraction is relatively stable, no clear trend is evident.

4.5. Combined interpretation of the proxies

Median grain-size measurements and end member modeling results indicate an enhanced deposition of wind-blown material during the YD in core GeoB 4223, GeoB 7430 and GeoB 7920. We interpret the coarse material found during the YD to represent higher wind speed and/or less vegetation cover within NW Africa. A further support of this interpretation is found in the higher amounts of quartz and k-feldspar in the dust fraction in all cores during the YD (see Table 2). Several studies demonstrated a general increase in dust flux during glacial stages [*deMenocal et al.*, 2000b; *Grousset et al.*, 1988] corroborating our results. Furthermore, several proxy-based investigations detected the YD as a period of dry conditions with increased NE trade winds in NW Africa [*Gasse et al.*, 1990; *Lancaster*, 2002; *Marret and Turon*, 1994; *Street-Perrott and Perrott*, 1990].

Changes in the end-member model and the median grain size of the northernmost core GeoB 6007 varies at a different pacing than the inferred changes in the monsoonal system. Since the core is located at 30°N we hypothesize that the deposition of terrigenous material is linked to the North Atlantic climate system. This suggestion is fostered by a proxy-based comparison between the potassium record of GeoB 6007 with the $\delta^{18}O$ record of the GISP2 ice core from Greenland [*Kuhlmann et al.*, 2004b]. They detected a periodicity of around 900 years throughout the last 9000 years and a higher frequency of 410 years from 4 to 2.5 ka, which are possibly caused by changes in

insolation [*Loutre et al.*, 1992] or by internal feedback mechanisms [*Schulz and Paul*, 2002]. A further comparison between the terrigenous fraction of the core with a drift-ice record from the sub-polar North Atlantic supports the idea that the terrigenous fraction of GeoB 6007 is linked with the North Atlantic climate system [*Holz et al.*, 2007].

Measured ε_{Nd} isotope values indicate no major change in the geological source area of the terrigenous fraction during the YD. However, $^{87}Sr/^{86}Sr$ isotopic ratios in the three northern cores indicate wetter conditions during the YD. This finding is contrary to our general interpretation of the climatic evolution of NW Africa during the Holocene suggested by the measured median grain sizes and end-member modeling in this study. We assume that the $^{87}Sr/^{86}Sr$ isotopic ratios reflect a change in the source area of the terrigenous material during the YD. Enhanced wind intensities and a southward shift of atmospheric circulation patterns are able to transport material from more distal sources with a different weathering regime to the core sites. This interpretation finds support in the mineralogy of the fine fraction with a higher amount of illit and micas during the YD, possibly causing higher $^{87}Sr/^{86}Sr$ values. Contrary to the general interpretation, the YD fine fraction is not interpreted as a pure fluvial end member but a mixture with fine distal dust reaching the core locations only under changed atmospheric circulation patterns during the YD. Possible sources of the distal dust areas could be the North African Mediterranean coast with a generally wetter climate but similar ε_{Nd} values [*Juteau et al.*, 1986]. A reduced vegetation cover which might be linked to dried up lakes in the area can create short term dust sources. The "wetter" isotopic composition is only visible in the three northern cores, which were in the influence of the North Atlantic Climate regime during the YD. Core GeoB 7920 yields lower amounts of illit and mica and isotopic values are in line with our interpretation of the end members.

The decrease in median grain size during the mid-Holocene points to changes in the transport mechanisms and/or changes in the hydrological conditions in the source area. As mentioned above, terrigenous material transported by rivers are distinctly finer than proximal material transported by wind [*Weltje and Prins*, 2003]. Results from end-member modeling support this hypothesis, and an increase of the fluvial end member during the AHP is visible in all cores, especially in the northern cores. Further support can be found in $^{87}Sr/^{86}Sr$ isotopic measurements. $^{87}Sr/^{86}Sr$ isotopic ratios for all cores show lower values and hence more humid conditions prevailed during the AHP than during the late Holocene. The decrease in the amount of quartz in the coarse sample fraction points to a decline in wind speeds during the AHP. Our results are corroborated by other proxy and modeling studies, where the AHP is shown as a period of enhanced precipitation and river runoff as well as an increased vegetation cover within NW Africa [e.g. *Gasse*, 2002; *Hillaire-Marcel et al.*, 1983; *Neumann*, 1993; *Tjallingii et al.*, 2008]. Due to the wetter environment the aeolian dust supply was diminished by 47% during the AHP [*deMenocal et al.*, 2000a]. The proxy-

based assumptions are also in agreement with modeling studies [e.g. *Kutzbach et al.*, 1996]. Changes in the earth's orbital parameters and an increase in summer insolation caused an intensification and northward displacement of the African monsoonal system during this time [*Berger and Loutre*, 1991; *Webster*, 1987]. A northward shift or northward expansion of the monsoonal rainbelt accompanied with an increase in precipitation and a northward displacement of the vegetation zones are also confirmed by several proxy [e.g. *Hoelzmann et al.*, 2004; *Lézine*, 1989; *Salzmann*, 2000] and modeling studies [*Claussen et al.*, 2003; *Kutzbach and Street-Perrott*, 1985].

Within the late Holocene (LH) we interpret the increase in the median grain size as well as an increase of the fine dust end member as a transition to modern arid conditions, which are reported for several sites in NW Africa [e.g. *Gasse and Van Campo*, 1994; *Lamb and van der Kaars*, 1995; *Renssen et al.*, 2006; *Swezey*, 2001]. A higher amount of quartz than during the AHP in the coarse fraction indicates dry but less windy conditions than during the YD. $^{87}Sr/^{86}Sr$ isotopic measurements are in line with the interpretation of drier conditions compared to the AHP. In the three northern cores the LH time slice yields driest conditions throughout the Holocene. Only in the southern core GeoB 7920 the YD is slightly drier.

In summary, measured median grain sizes, end-member modeling, mineralogical investigations and isotopic measurements suggests the fact that the YD was arid and characterized by a change and an intensification of the atmospheric circulation over NW Africa. Therefore, we conclude that during the Holocene NW African climate systems shifted latitudinally. Our data imply that during the YD the terrigenous signal and the isotopic values at the core sites are dominated by two different climatic systems. Whereas south of 26°N the NW African monsoonal climate is the only climate system influencing the core site, north of 26°N the core locations are influenced by both the monsoonal climate and the North Atlantic climate regimes. During the AHP sediments of cores GeoB 7920, GeoB 7430 and GeoB 4223 are predominantly influenced by the NW African monsoonal climate, only the northern core GeoB 6007 shows a clear imprint of the North Atlantic climate system. Therefore, our data fits well with other studies indicating a northward shift of the zonal climatic boundaries during the AHP, probably up to ~ 29°N. After the termination of the AHP climate systems shifted south again down to the modern position. Furthermore our data indicate that modern NW African climate is dry again, but apparently far less windy than the YD.

Conclusions

In order to gain information about the latitudinal position of the different climatic systems throughout the Holocene we studied four marine sediment cores offshore NW Africa between 20°N and 30°N. The combined interpretation of the measured grain-size distributions, end-member modeling, mineralogical investigations combined with isotopic measurements of Sr and Nd allows us

to hypothesize that the YD was characterized by enhanced atmospheric circulation with NE trade winds penetrating far into NW Africa. Our data suggest that the influence of the North Atlantic climate system reached at least down to 26°N during the YD. During the mid Holocene the boundary between both climate systems was located further north, possibly over almost 3° latitude. During LH these boundaries moved southward again (~1° latitude) towards the present position.

Acknowledgments

We thank Bas van der Wagt (VUA) for measuring Nd-samples on the Neptune and ICP-MS measurements. Martijn Klaver (VUA) is thanked for providing help with TIMS measurements. We thank Richard Smeets (VUA) for all the help in the clean-lab with chemical procedures. Sincere thanks are given to Wolfgang Bevern (MARUM) for technical support. Gert-Jan Weltje is acknowledged for making the end-member modeling algorithm available. This research was funded by the Deutsche Forschungsgemeinschaft (DFG) through the European Graduate College EUROPROX and MARUM – Center for Marine Environmental Sciences with additional funding from Europlanet. The data presented in this paper will be archived in the Pangaea database (www.pangaea.de).

Sensitivity of the deep-marine sediment archive offshore NW Africa to local climate changes during the Holocene

Inka Meyer[1] and Jan-Berend W. Stuut[1,2]

[1] MARUM - Center for Marine Environmental Sciences, Bremen, Germany
[2] NIOZ - Royal Netherlands Institute for Sea Research, The Netherlands

In preparation for publication in *Sedimentology*

An investigation of the terrigenous fraction found in a transect of seven marine sediment cores downwind of the Saharan Desert was used to demonstrate how environmental changes on the continent are registered in deep-marine sediments. Variations in the grain-size distributions were attributed to different transport mechanisms of terrigenous sediments carried into the marine realm. End-member modeling of the grain-size distributions clearly demonstrates three different size sub-populations, which are interpreted as predominantly as fine and coarse aeolian dust and fluvial material. Downcore relative contributions of the proportions of these sediment-transport processes are interpreted in terms of contributions Saharan dust versus fluvial material, which are used to make inferences about continental humidity and aridity within NW Africa during the Holocene. Our data show that general patterns in the input of terrigenous material and the characteristics of both the aeolian and the fluvial fraction can be observed along the transect from ~15° - 31°N. However, besides the comparable general patterns there are also large differences between nearby core locations, probably due to local effects of sediment generation on land, transport from source to sink, as well as registration in the marine sediment archive. Hence, climate reconstructions for entire NW Africa based on the observations of single sediment cores are potentially dominated by such local effects, and great care should be taken in the use of single sediment cores for general paleoclimatic reconstructions of large regions. Furthermore, our results show that great care should be taken with the interpretation of the end-member model. Due to differences in the parent material, end members with similar attributes could be delivered by different transport processes and could hence potentially reflect a different climatic history. Therefore, the end-member approach should always be compared with additional independent proxy data.

Keywords: Aeolian dust, deep-sea sediments, end-member modeling, grain size

Introduction

Huge quantities of mineral dust are carried from the Saharan Desert over and into the Atlantic Ocean every year and obviously all this dust [700-900 x 10^6 tons/year; e.g., *Goudie and Middleton,* 2006] has a dominant impact on marine sedimentation processes along the continental margins of NW Africa [e.g., *Harrison et al.,* 2001]. Presently, the Sahara generates around 50-70% of the global dust emission supplied to the world's oceans, more than any other dust source in the world [*Goudie and Middleton,* 2001; *Mahowald et al.,* 2005]. The dust laden air can travel immense distances across the Atlantic: Saharan dust particles were detected in the Caribbean and in Amazonia [*Ott et al.,* 1991; *Prospero et al.,* 1981]. Furthermore, Saharan dust was identified in the Mediterranean realm [*Stuut et al.,* 2009] and even in northern Sweden and Finland [*Franzen et al.,* 1994]. However, most aeolian dust carried from the Sahara is deposited in the Atlantic Ocean and therefore the aeolian fraction is a major component in marine sediments offshore NW Africa, where significant amounts of dust can be observed as far as the mid-Atlantic Ridge [*Holz et al.,* 2004; *Koopmann,* 1981; *Sarnthein et al.,* 1982]. Based on differences in grain size, the distance between origin and deposition of the dust as well as the altitude at which the particles are transported can be determined [*Stuut et al.,* 2005]. Far-travelled Saharan dust deposited in the Caribbean was shown to be generally smaller than 5 µm in size [*Talbot et al.,* 1986], similar to Saharan dust samples collected on Tenerife at 2000 m altitude [*Torres-Padron et al.,* 2002]. In contrast, proximal low-level aeolian dust samples yield grain sizes generally larger than 10 µm and up to 90 µm in diameter [*Glaccum and Prospero,* 1980; *Stuut et al.,* 2005].

Although NW Africa is presently an arid region, terrigenous sedimentation offshore the Saharan desert is also influenced by river discharge. Terrigenous material transported by rivers is shown to be finer in particle size than proximal aeolian dust. Grain-size measurements of fluvially transported sediments offshore major rivers in different sedimentary basins were found to be commonly smaller than 10 µm [*Weltje and Prins,* 2003]. Similar results were obtained by *Gac and Kane* [1986] who detected 95% of the suspended sediment load of the Senegal River to be smaller than 10 µm. Consequently, as was demonstrated already in many studies [e.g., *Holz et al.,* 2004, *Meyer et al.,* 2011; see also Chapter 5; *Tjallingii et al.,* 2008] we expect to be able to distinguish between proximal Saharan dust and fluvial sediments offshore NW Africa, solely based on the grain-size distributions of the terrigenous sediment fraction.

The Holocene climate is considered as fairly constant compared to the glacial-interglacial changes during the Pleistocene [*Dansgaard et al.,* 1993]. However, evidence of climatic variability on (sub-) millennial timescales in NW Africa is provided by several proxy- and model based studies. One of the most recent examples of abrupt short-term climate changes is the African Humid Period (AHP), between ~9 ka and 5 ka [*deMenocal et al.,* 2000a;

Ritchie et al., 1985]. Several paleoclimatic studies show that NW African climate shifted to warmer and more humid conditions during mid-Holocene times, triggered by changes in earth's orbital parameters [*deMenocal et al.,* 1993; 2000b; *Gasse,* 2000; *Nicholson and Flohn,* 1980; *Tjallingii et al.,* 2008]. An intensification of the NW African monsoonal circulation during that period, resulting in 25-30% higher precipitation values compared to modern times, was simulated by *Kutzbach and Street-Perrott* [1985]. As a result of the increased precipitation, most of the Sahara and Sahel region was covered by denser and more diverse vegetation, many lakes and swamps existed within NW Africa, limiting the aeolian supply to the Atlantic [*Gasse et al.,* 2000; *Lézine and Casanova,* 1989; *Lézine,* 1988; *Kuper and Kröpelin,* 2006]. While the existence of the AHP is generally accepted, the exact timing and abruptness of the AHP is still a matter of heated debate. While some studies support the theory of an abrupt start and end of the AHP [e.g., *Adkins et al.,* 2006; *deMenocal et al.,* 2000a; *Cole et al.,* 2009] other studies argue for a more gradual transition [*Fabre and Petit-Maire,* 1988; *Itambi et al.,* 2009; *Jung et al.,* 2004, *Kröpelin et al.,* 2008; *Lézine et al.,* 1990].

In order to provide a better understanding of the spatial and temporal variability of the AHP within NW Africa we present grain-size data and end-member modeling results of seven marine sediment cores building a transect along the NW African coast, between 15°N and 31°N and covering at least the last 12 ka (Table1). The combination of grain-size analyses and end-member modeling has been demonstrated to be able to distinguish between the different transport mechanisms of terrigenous sediments related to the environmental conditions in the source areas of the sediments [*Holz et al.,* 2004; *Stuut and Lamy,* 2004, *Tjallingii et al.,* 2008; *Prins and Weltje,* 1999].

Regional setting

The study area (Fig.1) is located on the continental margin of Morocco, Western Sahara, Mauritania and Senegal. The shallow continental shelf of NW Africa (< 150 m) is cut by several channel systems and canyons, e.g., the Western Sahara Canyon System or the Timiris Canyon [*Krastel et al.,* 2004; *Wynn et al.,* 2000]. The major surface water current in the area is the southward flowing Canary Current [*Mittelstaedt,* 1991]. Trade wind driven upwelling of nutrient-rich water occurs near the coast [*Mittelstaedt,* 1991].

The present-day climate conditions over NW Africa are governed by two different climate systems, which are separated by the Saharan desert belt [*Nicholson,* 2000]. The northern part is influenced by the Mediterranean regime, while the southern part of the study area is influenced by the latitudinal shifts of the Intertropical Convergence Zone (ITCZ). Modern observations display seasonal variability in precipitation and humidity over NW Africa: during boreal summer the ITCZ is located around 20°N resulting in an advance of humid air masses far north. In boreal winter, the movement of the ITCZ down to ~ 5°N generates a southward displacement of the humid air [*Nicholson,* 2000].

Dust is transported from the Saharan Desert to the area of investigation by two prevailing wind systems. In the northwest, the shallow NE trade wind layer, including the Harmattan wind system (500 to 1500 m height), transports dust from the north-western Sahara in south-western direction parallel to the coast [*Sarnthein et al.,* 1981]. The trade winds carry dust to the Atlantic Ocean year-round, but with highest intensities during boreal winter [*Stuut et al.,* 2005]. Dust from the southeastern Sahara and the bordering Sahel zone is transported directly westward with the higher Saharan Air Layer (SAL), coupled to the African Easterly Jet (AEJ) at higher altitudes (1000 to 5000 m) mainly during boreal summer [*Koopmann,* 1981; *Prospero and Carlson,* 1972; *Sarnthein et al.,* 1982].

Present-day river discharge within the study area is restricted to some permanent river systems in Morocco draining the Atlas Mountains, mainly during boreal winter

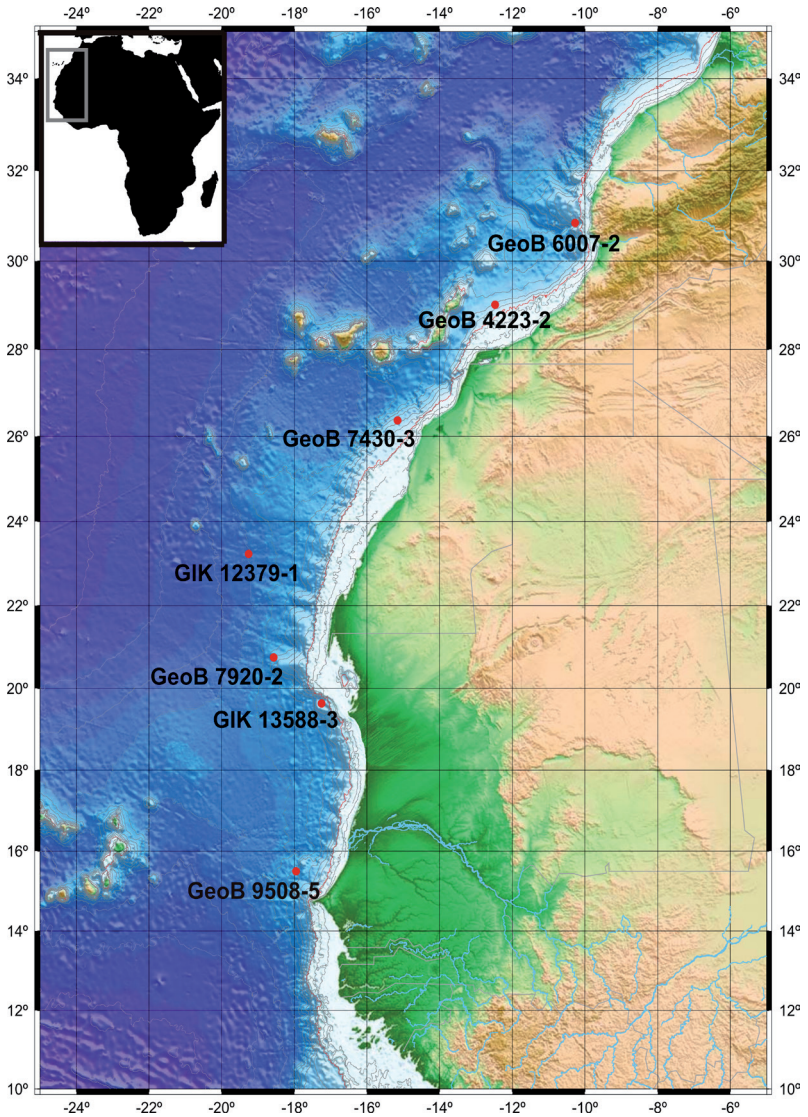

Fig.1
Map of study area offshore NW Africa. Shown are the locations of the seven marine sediment cores investigated in this study.

[*Summerhayes et al*., 1976; *Wynn et al.,* 2000]. South of ~29°N the fluvial supply is limited, most wadis reach the Atlantic only seasonally [e.g. *Wynn et al.,* 2002]. The largest continuous source of fluvial sediments in the region is the Senegal River at ~ 16°N. The sediment load delivered to the Atlantic Ocean is estimated to be around 2 x 10^6 tons per year [*Gac and Kane,* 1986].

Methods

For grain-size measurements the terrigenous sediment fraction was isolated from the marine components by using different chemicals to remove organic matter (H_2O_2), calcium carbonate (HCl), and biogenic silica (NaOH) in three different chemical treatments steps, respectively. To verify that all components were removed successfully, microscope analyses were carried out on single samples. For details of chemical pre-treatment steps see *Mulitza et al* [2008].

Grain-size measurements were established with a Laser Diffraction Particle Size Analyser (Beckman Coulter) LS200 resulting in 92 size classes from 0.4-2000 µm. To avoid that gas bubbles influence the quality of the analyses, measurements were done using demineralised and degassed water. All pre-treatments and the grain-size measurements were carried out in the laboratories at MARUM, Bremen.

For a better interpretation of the grain-size data and to identify distinct sediment sub-populations within each deep-sea sediment core, the numerical-statistical end-member algorithm EMMA was applied [*Weltje,* 1997]. The algorithm tries to ascribe the observed variance in the total data set to a number of subpopulations. These "end members" are chosen from the goodness-of-fit statistics by calculating the coefficient of determination (r^2). The result of the modeling approach is a statistically unique solution with end members that represent real particle-size distributions [*Welje*, 1997; *Weltje and Prins,* 2003].

Table 1. Geographical location and further sampling details of investigated marine sediment core between 15°N and 30°N.

Core	Longitude (°W)	Latitude (°N)	Water depth (m)	Sampling res. (cm)	Location	References Age models
GeoB 6007-2	10°16 W	30°51 N	900	2	Off Cape Ghir	[*Kuhlmann et al.,* 2004a]
GeoB 4223-2	12°28 W	29°01 N	775	1	Agadir Canyon	[*Freudenthal et al.*, 2002]
GeoB 7430-3	15°09 W	26°22 N	1165	1	off Cape Bojador	[*Kuhlmann,* unpubl.data]
GIK 12379-1	18°75 W	23°14 N	2136	1	off Cape Barbas	[*Sarnthein et al.,* 1994]
GeoB 7920-2	18°34 W	20°45 N	2278	5	off Cape Blanc	[*Tjallingii et al.,* 2008]
GIK 13588-3	17° 15 W	19°38 N	1000	1	Off Banc d'Arguin	[*DiesterHaaß,* 1981]
GeoB 9508-5	17°57 W	15°30 N	2384	5	off Senegal	[*Mulitza et al.,* 2008]

Sedimentation rates

Based on the published age models of the seven cores (see Table 1) we calculated sedimentation rates of all sediment cores. The northernmost core GeoB 6007 clearly stands out with extremely high sedimentation rates of almost 10 m sediment in the studied time interval of 12 ka. Variability in the other seven cores is less extreme and varies from about 55 to 170 cm in the same time period. Clear differences can be observed when the stratigraphy is subdivided into three time slices 0-2 ka, 5-9 ka, and 10-12 ka (see Table 2). These periods were chosen as representative for the known extreme environmental conditions in NW Africa: present-day (warm and dry), African Humid Period (warm and wet), and Younger Dryas (cold and dry). The sedimentation rates hardly differ between the YD and the AHP, although a slight increase in sedimentation rates occurs during the AHP. Except for core GeoB 7430, which has a lower overall sedimentation rate, all sedimentation rates are in the order of 10-15 cm/kyr during both the YD and AHP and considerably less during the most recent time slice in all cores except the northernmost and southernmost ones.

End-member model

The end-member algorithm EMMA [*Weltje,* 1997] was demonstrated to be a valuable tool to unmix the different components of grain-size distributions of terrigenous material found in marine sediments [e.g., *Stuut and Lamy,* 2004; *Stuut et al.,* 2002; *Prins and Weltje,* 1999; *Weltje and Prins,* 2003]. The minimum number of end members necessary for a satisfactory approximation of the data can be determined from the goodness-of-fit statistics, represented by the coefficients of determination (r^2). The goodness-of-fit statistics of marine sediment core GeoB 4223, investigated within this study, is shown in Fig.2, as an example of the modeling process that we carried out for each individual sediment core. In Fig. 2a the coefficient of determination is plotted against grain size in μm for models with two to ten

Table 2. Total Holocene sediment accumulation rate as well as calculated for time slices: 0-2 ka, 5-9 ka and 10-12 ka.

Core	Total stratigraphy (cm)	Total sed rate (cm/kyr)	Sed rate 0-2 (cm/kyr)	Sed rate 5-9 (cm/kyr)	Sed rate 10-12 (cm/kyr)
GeoB 6007-2	990	83	57	60	143
GeoB 4223-2	135	11	11	13	12
GeoB 7430-3	55	5	5	5	5
GIK 12379-1	86	7	1	11	10
GeoB 7920-2	170	14	10	16	15
GIK 13588-3	150	13	5	13	18
GeoB 9508-5	120	10	10	10	10

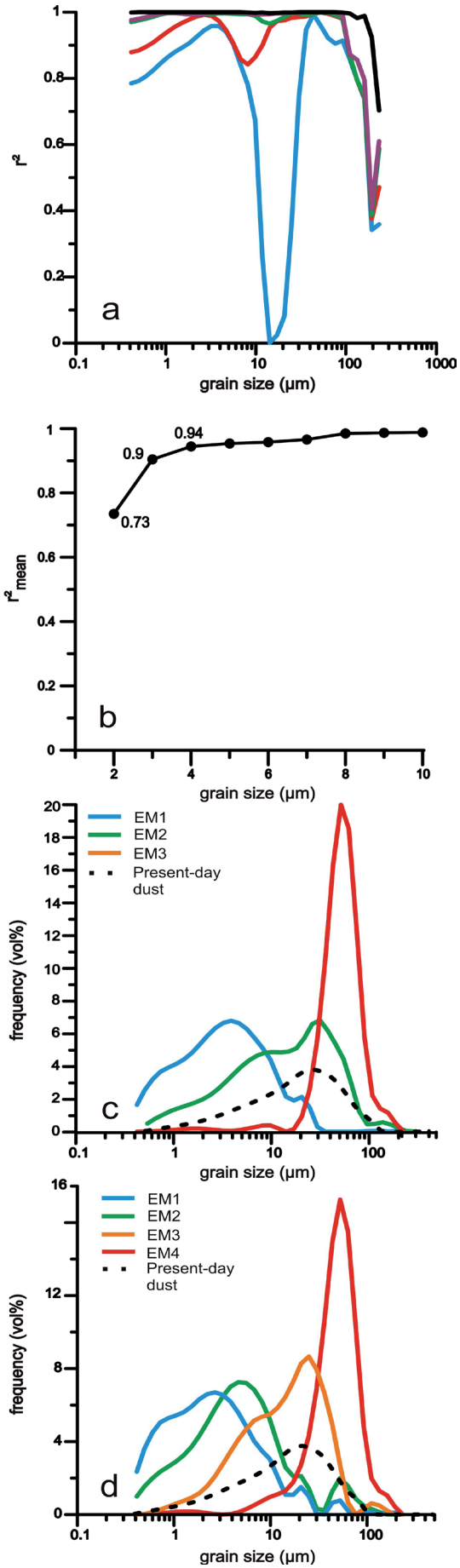

end-members. It is obvious in Fig. 2a, that within the two end-member model (blue line) grain sizes between 10 and 15 µm are only poorly represented. Within the three end-member model (red line) only the grain sizes at ~8 µm are not well reproduced. The plot shows, that the higher the number of end-members, the better all grain-size classes are represented. This is shown in Fig. 2b as well. Here, the mean coefficients of determination (r^2_{mean}) are plotted for each of the ten end-member models. The two end-member solution represents a mean coefficient of determination of $r^2_{mean} = 0.73$, whereas for the three end-member model a mean coefficient of determination of 0.90 is calculated, which means that 90% of the variance in each grain-size class can be reproduced by the model (Fig. 2c). The r^2_{mean} increases only slightly to 0.94 in the four end-member model. Furthermore, the grain-size distributions of the four end-member model show a bi- or even polymodal character (Fig. 2d). Here, the algorithm tries to model the noise in the data, resulting in complex end members, which are unrealistic in terms of sediment population as the result of a sediment-transport process. Hence, the three end-member model was chosen to provide the best balance between minimum number of end members and maximum r^2. In the three end-member model, the end members have a

Fig. 2.
End-member modeling results for sediment core GeoB 4223- 2 (12°W/29°N). **2a**) Coefficient of determination (r^2) for each size class of the two to ten end-member models; **2b**) Mean coefficient of determination (r^2_{mean}) for the different end-member solutions; **2c**) Modeled three end-member solution and the grain-size distribution of a present-day aeolian dust sample offshore NW Africa obtained by *Stuut et al.* [2005].

clearly defined dominant mode. End-member EM1 has a modal grain size of ~ 4 µm, EM2 of approximately 25 µm, and end-member EM3 has a modal grain size of about 53 µm. Within the three end-member model both coarser end members are interpreted as aeolian dust. In detail, we interpret the coarsest two end members as the beginning and end process of aeolian deposition where EM3 is composed of 'coarse' aeolian dust, and EM2 represents the 'fine' aeolian particles. The coarsest end-member (EM3) has a clearly defined modal grain size of ~ 53 µm, whereas EM2 has a mode of ~ 25 µm. This is consistent with present-day aeolian dust collected along a transect off the NW African coast between ~ 33°N and ~ 12°S, which was shown to vary between 8 and 48 µm [*Stuut et al.,* 2005]. The grain-size distribution of a present-day dust sample collected during *R/V Meteor* cruise 41/1 was plotted with the end members of the three- and four end-member solutions in Figures 2c and d [*Stuut et al.,* 2005]. The fine-dust end member compares very well with the present-day dust sample (Fig. 2c).

For all seven sediment cores we calculated individual end-member models, all with three end members. The grain-size distributions of the different end-member models are so different that it was not possible to establish one single model for all cores. Modeled end members and the mean coefficient of determination (r^2_{mean}) for all cores are shown in Fig. 3. EM1 is significantly finer grained in all cores, with a mean modal grain size of 4 to 7 µm. EM2 has a mean modal grain size of 12 to 38 µm, and EM3 has a mean modal grain size of 24 to 63 µm.

Following the shown procedure we modeled the grain-size distributions of the terrigenous sediment fraction of all seven deep-sea sediment cores. Based on the calculated r^2_{mean} values the three end-member model was chosen as the optimal balance between statistical description of the variance in the data set and complexity of mixture composition in all cores.

Discussion

Although all marine sediment cores investigated during this study are located on the continental slope offshore NW Africa, at about the same distance from the source of the wind-blown particles, large variations between the particle size of the calculated end members can be observed. EM1, which is interpreted as fluvial sediment, shows the smallest amount of variability between the sediment cores, ranging between 4 µm and 7 µm. Due to the proximal position of the investigated sediment cores to the African dust sources, aeolian sediments are generally characterized by coarser grain sizes than sediments supplied by rivers. Therefore, we interpret the finest end member as predominantly the result of fluvial transport. This interpretation is in line with other studies on grain sizes of fluvial sediments [*Gac and Kane,* 1986; *Holz et al.,* 2004; *Weltje and Prins,* 2003]. With respect to the core location in the vicinity of several small river systems and wadis, a stronger imprint of fluvial material might be expected, both in the proportions of the fluvial sediments as well as in the total sedimentation rates observed in the seven cores. However, the sedimentation rates

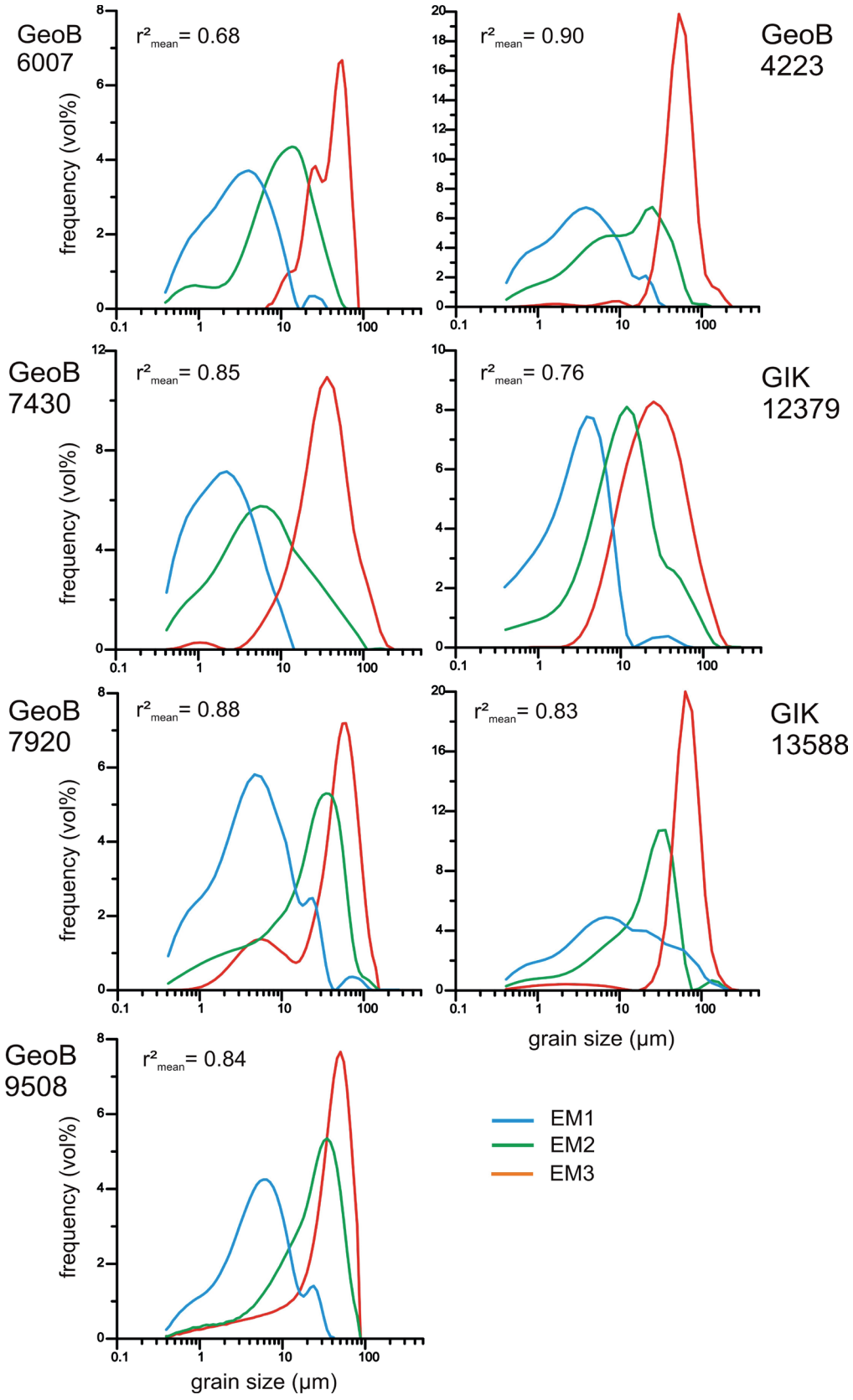

Fig. 3.
Modeled end members and calculated coefficients of determination (r^2) for the three end-member solutions of the seven marine sediment cores investigated within this study. Please note the differences in grain size and frequency of the single end-members between the different cores.

in Table 2 are *bulk* sedimentation rates, i.e., including the biogenic fraction. Taking into account that during the YD the trade winds were much stronger, and hence upwelling and primary productivity were increased [e.g., *Filipsson et al.,* 2011, in press], it seems very logical that the bulk sedimentation rates are high, as a result of large amounts of planktic foraminifera, diatoms, and benthic foraminifera. The fact that during the AHP the bulk sedimentation rates are as high as during the YD or even slightly higher (Table 2), although the amounts of organic matter and biogenic opal and calcium carbonate decreased dramatically during the AHP [*Filipsson et al., 2011,* in press], can only be explained by a substantial increase in terrigenous sediments, most likely delivered by rivers and wadis as a result of increased precipitation on land.

The mid-sized end member EM2 varies between 12 μm and 38 μm between the seven sediment records. This end member shows mostly a clear mean modal distribution, but grain sizes of the end member are again very different between the cores. EM3, interpreted as the coarse-dust end member, demonstrates a clear unimodal distribution, although grain sizes within EM3 vary between 24 μm and 63 μm among the seven cores. Assuming that the interpretation of the three end-member model is correct, the large differences between the single end members need to be explained. The end-member model is used to calculate the different components of grain-size distributions of bulk terrigenous material. Obviously, Saharan dust that is blown in from the NW African continent is strongly influenced by the parent material from which it is derived. As an example, sand dunes as well as dried lake beds are known to be important sources of dust [e.g., *Stuut et al.,* 2009] but obviously, they yield different grain-size distributions from sand to clay size fractions, as a result of the dust-production mechanism [e.g., *Smalley and Vita-Finzi,* 1968; *Pye and Tsoar,* 2009]. Furthermore, differences in prevailing wind systems and wind intensities are important for aeolian sediment supply, with a major influence on the size distribution of the transported sediments.

The end-member proportions of the marine sediment cores GeoB 4223 (the second northernmost core; Figs. 1 and 4) and GeoB 9508 (the southernmost core; Figs. 1 and 4) are used as an example to show and explain downcore variations within the end-member records. Sediment core GeoB 4223 is retrieved from the continental slope offshore Morocco, at 29°N (Fig. 1). Variations within the end-member proportions of core GeoB 4223 are shown in Fig. 4 (upper panel). During the YD, the most dominant sediment fraction is the fine dust with 79%, reflecting continental aridity. Furthermore, there is a clear increase in the coarse-dust fraction at the end of the YD up to 24 % of the total terrigenous sediment budget. The higher proportion of this fraction is interpreted as the result of stronger trade-wind intensities during the YD as suggested by several investigations [e.g., *Marret and Turon,* 1994]. Only 7% of the sediment fraction during the YD is ascribed to fluvial material, indicating dry conditions on the continent. After the termination of the YD, the proportions of both dust end members decrease

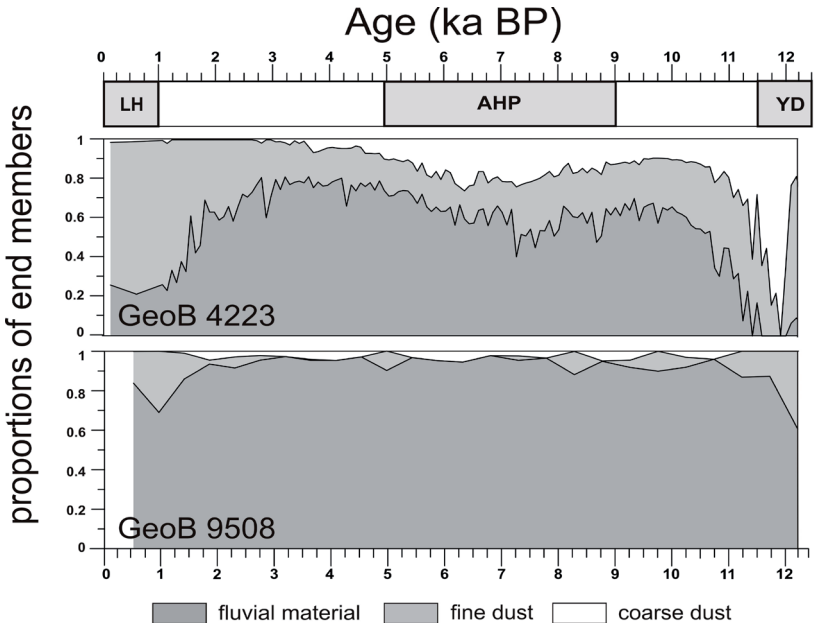

Fig. 4.
Comparison of downcore end-member proportions since ~12 ka. As representatives of the whole transect core GeoB 4223 and GeoB 9508 were chosen.

considerably towards the mid Holocene. During mid-Holocene times, the amount of coarse dust ranges around 13%, the fine dust around 26%. At ~ 8 ka the fluvial fraction is the most dominant sediment fraction, forming 60% of the total terrigenous sediment budget. Possibly as a result of increased precipitation and a denser vegetation cover, the aeolian transport was reduced during the mid-Holocene, whereas the fluvial input increased. Since the last 2 ka a constant decrease in the fluvial end member (down to 2%) and at the same time an increase in the fine dust (up to 74%) can be observed, reflecting the modern dry conditions. Near the core location the River Draa and several wadis fed by melt water and runoff from the Atlas Mountains reach the Atlantic Ocean only seasonally under modern arid conditions [*Summerhayes et al.,* 1976]. The amount of the coarse dust fraction during the latest Holocene is insignificant, pointing to arid but less windy conditions compared to the YD.

Sediment core GeoB 9508 (Fig. 4; lower panel) was recovered from the NW African continental margin at 15°N (Fig.1). The core is located just outside the Senegal-River mud belt, offshore the biggest source of fluvial sediments that are discharged along the NW African coast. Within the end-member proportions during the Holocene there is a clear dominance of the fluvial sediment fraction, varying from 49% during the YD to 95% during the mid-Holocene. Without a doubt the clear dominance of the riverine component in GeoB 9508 can be explained by the core location being so close to the Senegal-River mouth. The dominance of the riverine input during mid-Holocene times, the AHP, is in line with numerous proxy- and model based studies, suggesting more humid conditions during this period [e.g., *Gasse,* 2002; *Kuper and Kröpelin,* 2006]. In late-Holocene times, a slight decrease in the fluvial fraction can

be observed, but the fluvial fraction is with 79% still the dominant sediment fraction. The decrease in the riverine sediment fraction during recent times is interpreted as the result of a gradual drying up of NW Africa towards the latest Holocene, potentially strengthened toward the top of the core by anthropogenic imprints like land use, as recently presented by *Mulitza et al* [2010/Chapter 8]. Next to the fluvial fraction a fine dust fraction is visible in the record. The amount of the fine aeolian component is generally lower than the fluvial fraction and has highest values during the YD (39%). During mid-Holocene times, only 3% of the terrigenous sediment is composed of fine aeolian dust. Towards the late Holocene, the amount increases again, up to 20%. The coarse dust fraction is by far the least relevant component in the core, with highest amounts during the YD (13%) and very low proportions during the mid- and late Holocene (2% and 1%, respectively).

As is evident from these two records, the general paleo-environmental interpretations are the same, and in accordance with previously published studies. However, there are clear differences between the amounts and the grain-size characteristics of the single end members. In both cores the fluvial sediment fraction is the most important component due to the locations of the cores next to river systems. As indicated by the end-member record of core GeoB 9508, the Senegal River was constantly active during the Holocene. In contrast, the River Draa shows much more extreme variations in discharge during the Holocene, although discharging large amounts of sediments. The comparison of the two records illustrates that the amounts of riverine transported sediments in GeoB 4223 are not as high as from the Senegal River, recorded by core GeoB 9508, and that therefore, the environmental conditions in NW Africa can be much clearer observed. During the YD, no riverine material is visible in the northern record, pointing to dry conditions and clearly diminished river discharge. Enhanced trade-wind intensities during the YD were able to transport very coarse material to the core site. This fraction is far less clearly visible in core GeoB 9508, possibly only the finer fractions were deposited at the core location due to the greater distance that the trade winds travelled between the dust source(s) and the core location.

Since the southern- and northernmost (excluding core GeoB 6007 as it is clearly completely different, see also *Meyer et al.*, sub./Chapter 6) sediment records were chosen to investigate the NW African climate since the YD and the general climate trends were similar, one could expect similarities in the records of the other sediment cores, that are in between, as well. However, our data show that the downcore end-member proportions vary extremely along the transect of seven cores (Fig.5). In core GeoB 7430 (26°N) there is obviously a dominance of dust during the YD (96%) and only little riverine input at that time. However, the total dust is mainly composed of fine dust during the YD (83%). The quantity of fluvial material increases constantly with the beginning of the early Holocene but is still below 20% during the mid Holocene. The fine dust fraction is still the most important component. The generally

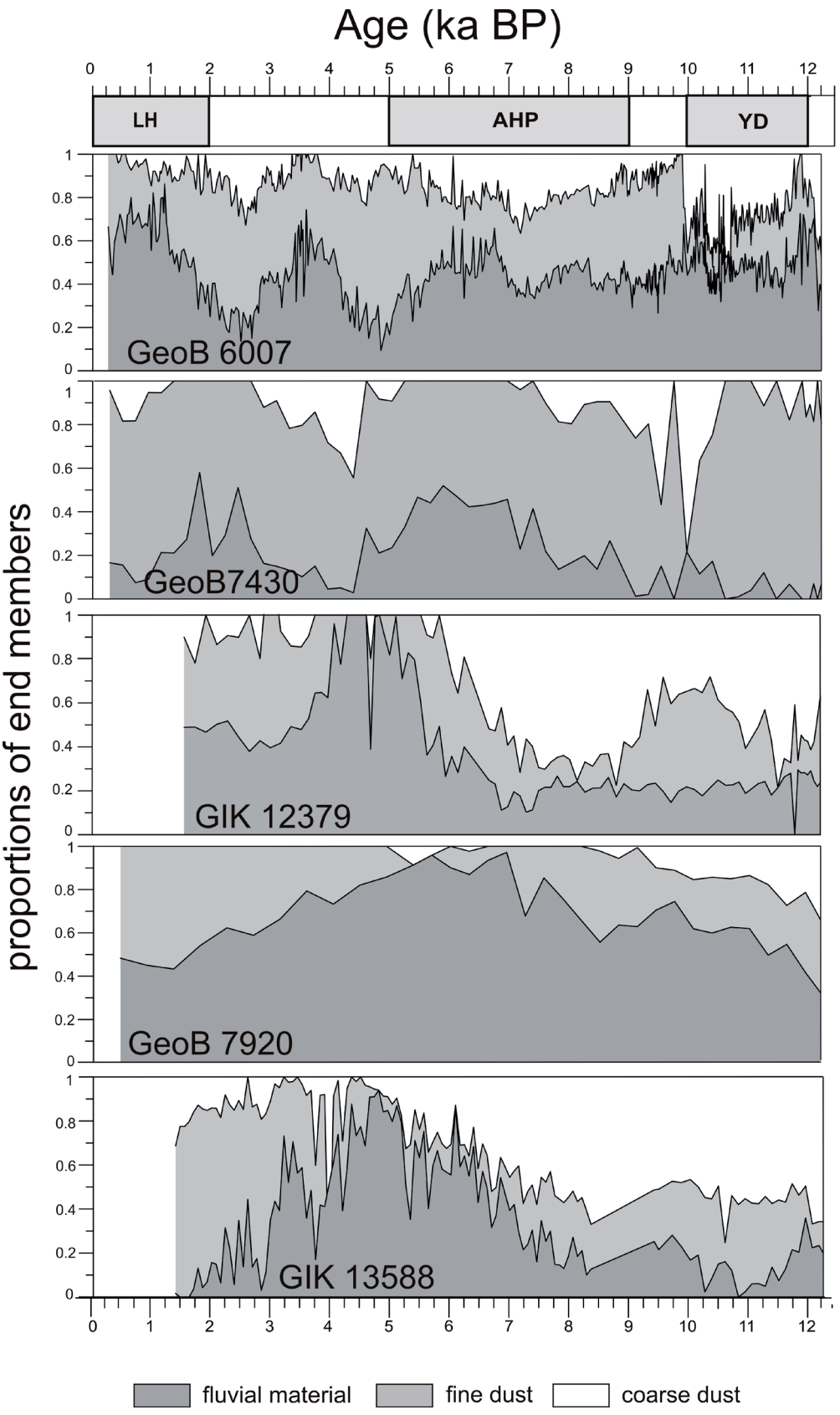

Fig. 5.
Downcore end-member proportions of single sediment cores offshore NW Africa since ~12 ka.

small input of material transported by rivers is caused by the absence of any active river system near the core location during modern times. However, due to the more humid conditions during the mid Holocene, smaller coastal rivers (which are clearly visible in the modern topography, see Fig. 1) possibly discharged fluvial sediments near the core location as well. The record is interrupted by several abrupt increases in the coarse dust fraction, which possibly reflect short-term dry spells. Unfortunately, gravity-driven sediment transport could not be excluded within the area [*Wynn et al.,* 2002]. Therefore, the two distinct intervals between 10 ka and 9.5 ka which are dominated by a huge amount of coarse material might reflect mass-wasting events. During the late Holocene, a decrease of the fluvial end member and a contemporaneous increase in the fine dust fraction is visible in the core. This is interpreted as a return to more arid conditions within NW Africa, and is in line with the other cores.

In the older parts of the downcore record of GIK 12379 the dominance of the coarse dust end member is obvious. This portion clearly dominates the record between 12.5 to 7 ka with 60% of the total terrigenous sediment fraction. The proportion abruptly decreases after 7 ka whereas the fine dust end member increases simultaneously. There is only a minor abundance of fluvial matter within the records, until around 6 ka (~20%). A significant and abrupt increase in the fluvial fraction is shown between 6 to 4 ka, possibly a (delayed) AHP signal. Unfortunately, the top of GIK 12379 was dated to be ~ 1.5 ka, therefore, no observations for the late Holocene can be done. The general trend with a higher amount of coarse dust during the YD, an increase in fluvial supply during the AHP, and a dominance of fine dust towards the end of the record can also be observed in core GeoB 7920 (20°N). Although presently there are no rivers located next to the core site, a huge paleo-river system, the Tamanrasett River, was reconstructed based on topographic patterns [*Vörösmarty et al.,* 2000]. GIK 13588 shows a similar downcore pattern of end-member proportions as GIK 12379. Until 7 ka a clear dominance of the coarse dust fraction is visible (~85%). Between 6 and 4 ka the fluvial input clearly dominates, again possibly a delayed AHP. The termination of this event is as abrupt as its beginning and the fine dust end member dominates in late-Holocene times. Similar to GIK 12379 due to a missing core top no observations during the late Holocene are possible.

Contrary to all sediment cores along the transect core GeoB 6007 (30°N) is characterized by high-frequency oscillation. This observation was made in other studies as well [e.g. *Kuhlmann et al*. 2004a; *Holz et al.,* 2007; *Meyer et al.*, sub./Chapter 6]. The core is positioned near the Souss River which drains the Atlas Mountains year-round under modern conditions [*Summerhayes et al.,* 1976; *Wynn et al.,* 2002]. The downcore end-member proportions show clear millennial-scale variations. Due to the close locality next to the Souss River the fluvial fraction is the dominant end member within the core. During the YD period the sum of coarse and fine dust is increased but builds only 28% of the sediment, fluvial material is still the

most abundant sediment component (72%). Within the Holocene the fluvial portion displays regular oscillations with highest values at 6 ka, 3 ka and 0.7 ka. The high-frequency oscillations of sediment core GeoB 6007 are not linked with the NW African monsoonal system. As suggested in former studies the terrigenous fraction of GeoB 6007 is predominantly influenced by the North Atlantic climate system [*Holz et al.,* 2007; *Meyer et al.,* sub./Chapter 6].

The comparison of downcore proportions of the different sediment cores clearly reveals immense differences between the individual core locations. Differences between the end-member proportions of the different cores are caused by numerous facts. As apparent in Table 1 sediment cores were sampled at different sampling resolutions. Logically, records from sediment cores with a higher sampling resolution provide more details. Moreover, sedimentation rates at each core site vary in the order of few millimeters to several centimeters per 100 years as shown in Table 2. Thus, each analyzed sample represents at least several years and a huge number of dust-transport or rain events, which have been mixed up thoroughly. Therefore, short term events are most likely completely obscured within the sediments. Another influencing factor is the applied dating technique and age-model construction at each study site. Variation in the methods used for dating or differences in the amount of tie points strongly influences the accuracy of the age models.

Even if the interpretation of the three end-member solution is true for some cores, e.g. GeoB 4223 and GeoB 9508, some other cores might need an alternative interpretation. As mentioned above, one source of mismatch between the end members could be the origin/production mechanism of the wind-blown particles. Large dune fields are known to be located near the coast in Western Sahara and Mauritania [e.g., *Lancaster et al.,* 2002]. Sand delivered by these dune fields could cause the high amounts of coarse dust within GIK 12379 and GIK 13588, especially during times of enhanced wind speeds and hence higher transport capacity of the winds, like during the YD. Furthermore, it is possible that the finest sediment fraction, originally interpreted as fluvial mud, in both cores is not solely a fluvial fraction since no river system is in the vicinity of the core locations. An alternative interpretation could be a second finer dust end member from more distal sources, mixed up with fluvial sediments of the same grain size.

Conclusion

This study shows that end-member modeling is a powerful tool to reveal insights into past climate variability and changes in hydrological conditions within NW Africa since the YD. By applying the end-member model to the grain-size distributions of the terrigenous sediment fraction, we are able to distinguish between sediment populations derived by different sediment transport mechanisms. The downcore proportions of the different end members throughout the Holocene clearly reflect short-term climate changes like the YD and the AHP. The abruptness of the start and termination of the AHP could not be defined

within the sediment cores along the transect, due to large differences in the temporal resolution of the age models of the various records. This problem can only be solved by applying consistent dating techniques on the individual cores in the transect. Our data imply that the input of terrigenous material and the characteristics of both the aeolian fractions and fluvial material are strongly influenced by local features such as former river systems, gravity driven sediment transport, or differences in the dust-production mechanism. Climate reconstructions based on the investigation of single sediment cores are potentially dominated by such local imprints, and therefore, great care should be taken with the interpretation of such records. Furthermore, care should be taken with the interpretation of the end-member model. Due to differences in the parent material, end members with the same attributes could be delivered by different transport processes and therefore potentially carry a signal caused by different paleo-environmental conditions.

Acknowlegements

Gert-Jan Weltje is acknowledged for making the end-member modeling algorithm available. Rik Tjallingii is thanked for providing help with the GMT mapping tool. This research was funded by the Deutsche Forschungsgemeinschaft (DFG) through the European Graduate College EUROPROX and MARUM – Center for Marine Environmental Sciences.

Increase in African dust flux at the onset of commercial agriculture in the Sahel region

Stefan Mulitza[1], David Heslop[1], Daniela Pittauerova[2], Helmut W. Fischer[2], Inka Meyer[1], Jan-Berend Stuut[1,3], Matthias Zabel[1], Gesine Mollenhauer[1,4], James A. Collins[1], Henning Kuhnert[1] & Michael Schulz[1]

[1] MARUM- Center for Marine Environmental Sciences, Bremen, Germany,
[2] Institute for Environmental Physics, University of Bremen, Germany
[3] NIOZ, Royal Netherlands Institute For Sea Research, The Netherlands
[4] Alfred Wegener Institute for Polar and Marine Research, Bremerhaven, Germany

Published in *Nature*

The Sahara Desert is the largest source of mineral dust in the world [*Engelstaedter et al.,* 2006]. Emissions of African dust increased sharply in the early 1970s [*Prospero and Lamb,* 2003], a change that has been attributed mainly to drought in the Sahara/Sahel region [*Prospero and Lamb,* 2003] caused by changes in the global distribution of sea surface temperature [*Folland et al.,* 1986; *Giannini et al.,* 2003]. The human contribution to land degradation and dust mobilization in this region remains poorly understood [*Hein and De Ridder,* 2006; *Mahowald et al.,* 2002; *Nicholson et al.,* 1998; *Prince et al.,* 2007; *Prospero et al.,* 2002; *Tegen and Fung,* 1995; *Webb,* 1995], owing to the paucity of data that would allow the identification of long-term trends in desertification [*Brooks et al.,* 2005]. Direct measurements of airborne African dust concentrations only became available in the mid-1960s from a station on Barbados [*Prospero and Lamb,* 2003] and subsequently from satellite imagery since the late 1970s: they do not cover the onset of commercial agriculture in the Sahel region 170 years ago [*Austin,* 2009; *Mbow et al.,* 2008; *Webb,* 1995]. Here we construct a 3,200-year record of dust deposition off northwest Africa by investigating the chemistry and grain-size distribution of terrigenous sediments deposited at a marine site located directly under the West African dust plume. With the help of our dust record and a proxy record for West African precipitation [*Shanahan* et al., 2009] we find that, on the century scale, dust deposition is related to precipitation in tropical West Africa until the seventeenth century. At the beginning of the nineteenth century, a sharp increase in dust deposition parallels the advent of commercial agriculture in the Sahel region. Our findings suggest that human-induced dust emissions from the Sahel region have contributed to the atmospheric dust load for about 200 years.

Keywords: Sahel, precipitation, land degradation, dust emission

This chapter is based on: doi:10.1038/nature09213

We have constructed a long-term record of African dust deposition extending far beyond the instrumental record by investigating the chemistry and grain-size distribution of terrigenous sediments deposited at marine site GeoB9501 (16° 50′ N, 16° 44′ W), located on a shallow terrace on the northern flank of the Mauritania canyon at a water depth of 323 m. Today this location receives terrigenous sediments in the form of atmospheric dust and Senegal River suspension [*Koopmann,* 1981] (Fig. 1). The geochemical signatures of these two sources are very different (Supplementary Fig. 3). The Senegal River drains the western part of Guinea [*Kattan et al.,* 1987] and transports suspended matter derived from deeply weathered soils formed under tropical conditions far south of the modern river mouth. These lateritic soils, and hence the Senegal River suspension, are rich in aluminium and iron [*Gac and Kane,* 1986]. Approximately 95% of the particles delivered by the Senegal River are smaller than 10 µm [*Gac and Kane,* 1986]. In contrast, coarse dust with particle

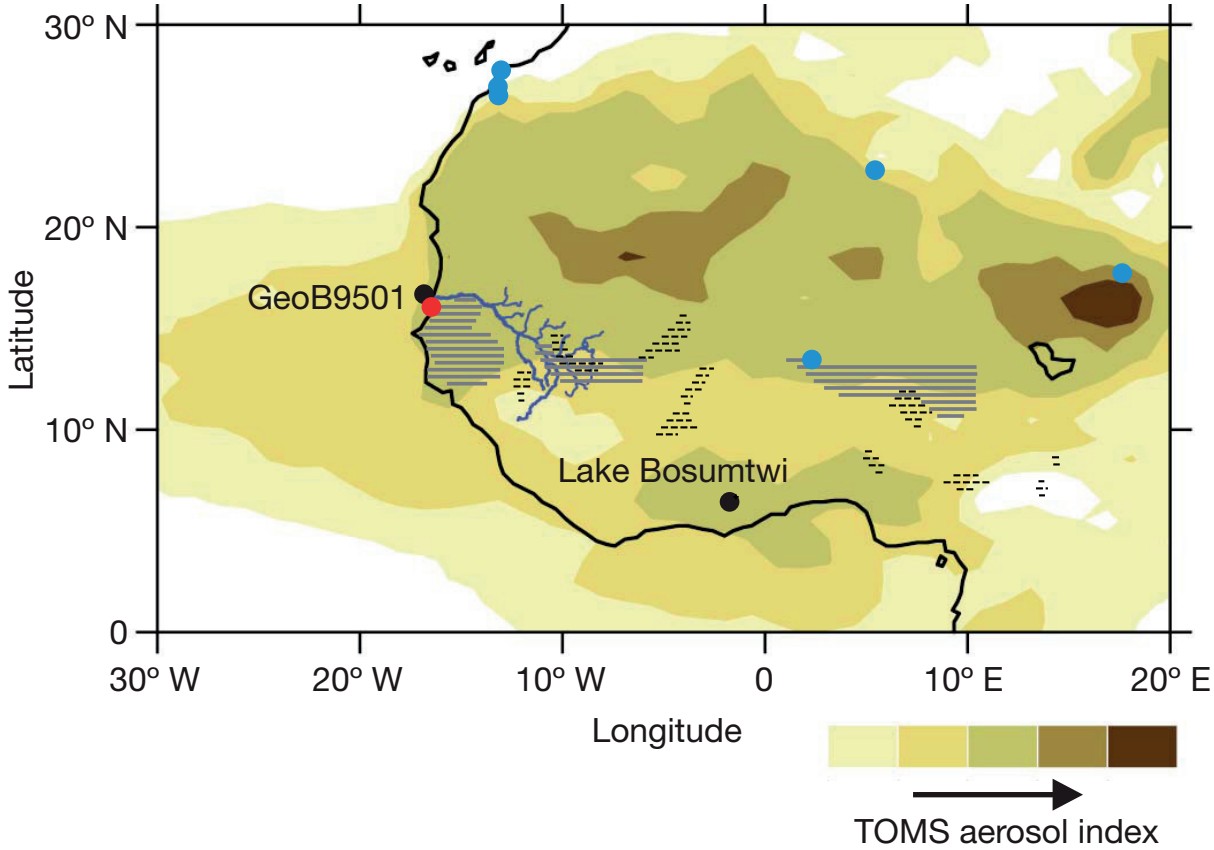

Figure 1. Locations of site GeoB9501 and Lake Bosumtwi.
The Senegal River and tributaries are shown in blue and the averaged Total Ozone Mapping Spectrometer (TOMS) aerosol index for the years 1997–2005, highlighting the Sahara-Sahel Dust Corridor, is shaded in yellow to brown. (TOMS data are available at http://toms.gsfc.nasa.gov/.) Black dots show the locations of site GeoB9501 and Lake Bosumtwi. Also shown are the locations of dust/soil samples [*Moreno et al.,* 2006] (blue dots) and fluvial suspension samples [*Gac and Kane,* 1986] (red dot) used to construct the end-member model. Horizontal hatching indicates areas of commercial groundnut (solid) and cotton (dashed) production in 1914 AD [*Austin,* 2009].

sizes up to 200 µm [*Stuut et al.,* 2005] that is relatively rich in silicon [*Moreno et al.,* 2006] is mobilized in the Sahel and the western Sahara [*Prospero et al.,* 2002] from where it is transported to site GeoB9501 primarily by trade winds and within the Saharan Air Layer [*Prospero and Carlson,* 1980]. Instrumental data indicate that dust input and fluvial runoff are inversely related (Fig. 2b). Any change in continental precipitation should alter the relative proportions of atmospheric dust and river suspension deposited on the continental margin off Senegal and Mauritania and hence should modify the grain-size distribution and geochemistry of the bulk sediments. The record of site GeoB9501 has been derived from a 0.43-m-long multicore, documenting the most recent phase of sedimentation and a 5.32-m-long gravity core spanning the past 3,200 years (Fig. 2a). The age model for both cores is based on a combination of radiocarbon dating of planktonic foraminifera and $^{210}Pb/^{137}Cs$ dating (Supplementary Methods and Supplementary Fig. 1). To quantify the relative proportions of atmospheric dust and Senegal suspension, we measured the downcore bulk concentration of Al, Si, Ca, K and Ti (Supplementary Methods). Representative dust and fluvial endmember compositions were constructed by bootstrapping the elemental concentration data of nine modern aeolian samples from the Sahara–Sahel Dust Corridor [*Moreno et al.,* 2006] and ten samples of suspended material from the Senegal River [*Gac and Kane,* 1986]. The relative abundances of the dust and fluvial end-members, along with a theoretical marine end-member (Supplementary Methods), were then determined by constrained non-negative least-squares applied throughout the sediment core. To determine mass accumulation rates, the relative contributions of the three end-members were multiplied by the product of dry bulk density and sedimentation rate (Supplementary Methods).

The $^{210}Pb/^{137}Cs$ dated part of our record overlaps with the instrumental record and shows clearly that the increase of African dust emission observed from Barbados after 1968 [*Prospero and Lamb,* 2003] was associated with an increase in dust deposition flux at site GeoB9501 (Fig. 2b). The distribution and deposition of African dust is variable in space and time [*Engelstaedter et al.,* 2006]. Moreover, Barbados receives most of its dust during the summer [*Prospero et al.,* 2002], whereas the dust deposition flux at the African coast is highest during the winter months [*Orange and Gac,* 1990]. This seasonal and spatial heterogeneity is a plausible explanation for slight differences between the Barbados dust concentration and the dust deposition flux at site GeoB9501.

The evolution of the bulk geochemical and grain-size signature at site GeoB9501 indeed indicates pronounced changes in the source of terrigenous sediments over the past ~ 3,200 years (Fig. 2a). The oldest part of the record from about 1200 BC to about 200 AD is dominated (>78%) by fine-grained fluvial sediments. The next 700 years are characterized by a gradual increase in dust deposition and grain size, stabilizing around 900 AD. From the fourteenth century onwards,

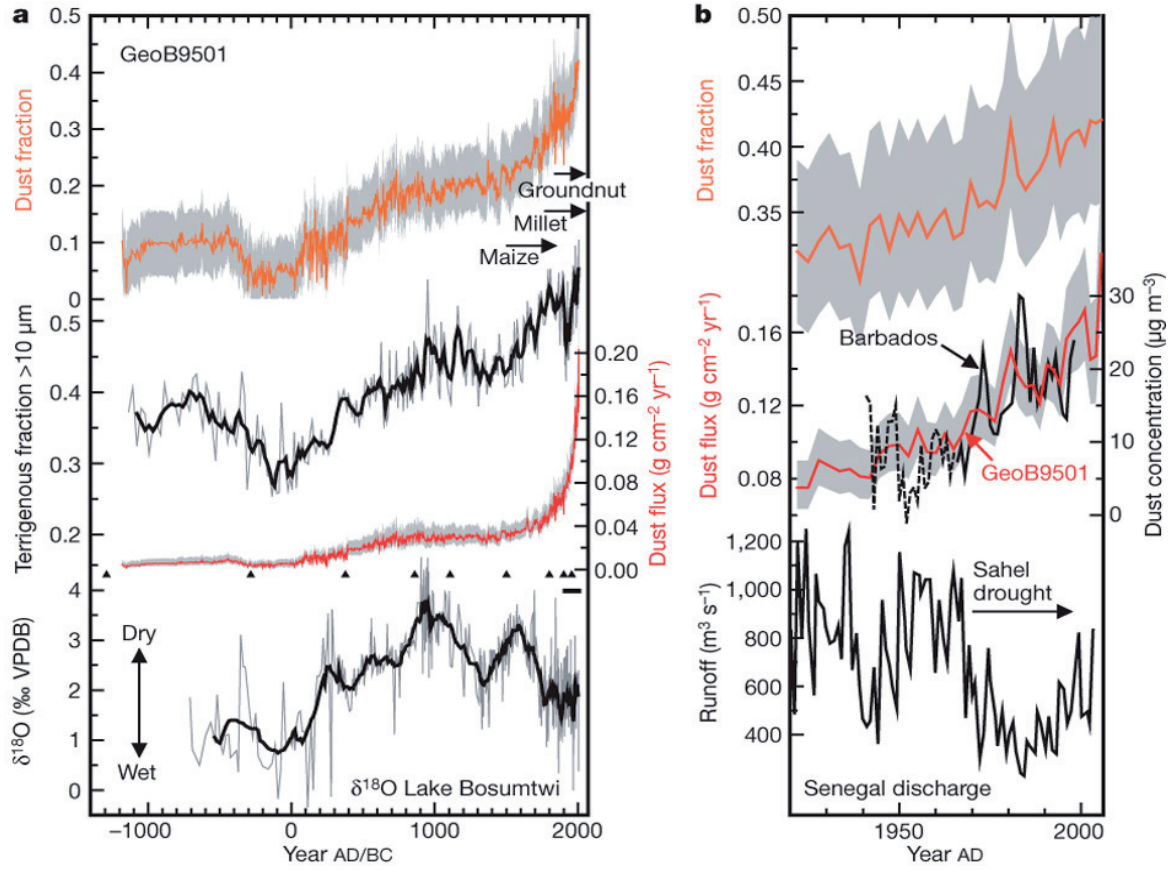

Figure 2. Comparison of dust deposition and precipitation records for the late Holocene.
a, The mean dust fraction (orange line) with grey shading showing the derived uncertainty envelope described in the Supplementary Methods, terrigenous grain-size fraction. 10 µm (black line, smoothed with a five-point moving average), and dust deposition flux (red line with shaded 95% confidence interval) are shown for site GeoB9501 (top three traces). The $\delta^{18}O$ of authigenic carbonates from Lake Bosumtwi [*Shanahan et al.,* 2009] is shown as the bottom trace (grey raw data smoothed with a black 13-pointmoving average).VPDB, Vienna Pee-Dee Belemnite reference. Triangles indicate radiometric age-control points (Supplementary Table 1). The short horizontal black bar indicates the range of $^{210}Pb/^{137}Cs$ dating. Horizontal arrows indicate the times at which maize, millet and groundnut agriculture became dominant. **b**, Shown are the mean dust fraction (orange line) with grey shading showing the derived uncertainty envelope, dust deposition flux (red line with shaded 95% confidence interval) at site GeoB9501 and instrumental records of atmospheric dust concentrations at Barbados [*Prospero and Lamb,* 2003] (black line) and the Senegal runoff (black bottom trace; redrawn from *Isupova and Mikhailov* [2008]). The horizontal arrow indicates the onset of Sahel drought in 1968. Barbados dust concentrations before 1966 (dashed black line) have been estimated [*Prospero and Lamb,* 2003] from regression with Sahel precipitation.

dust deposition rises again with the steepest increase of the entire record occurring after the early nineteenth century (Supplementary Fig. 4). Sedimentation rates increase along with the amount of dust deposition (Supplementary Fig. 2). Components of marine origin constitute only a minor proportion of the sediment (Supplementary Fig. 2), so the total sediment accumulation must therefore be primarily controlled by the lithogenic flux and not by

marine production (Supplementary Notes). Evidence that much of the natural variability in dust supply to site GeoB9501 is driven by continental precipitation comes from the oxygen isotope record of Lake Bosumtwi in Ghana [*Shanahan et al.,* 2009]. The $\delta^{18}O$ record from this lake is representative for precipitation in the Sahel [*Shanahan et al.,* 2009] and close to the tropical source region of the Senegal River (Fig. 1). During the period from 100 AD to 900 AD a clear drying trend is visible in Lake Bosumtwi along with an increase in dust deposition at site GeoB9501. During the next 400 years precipitation on land increases and dust input stabilizes. Dust deposition increases again with the onset of another long-lasting drought between 1400 and 1700 AD. The correlation between dust-deposition flux and Bosumtwi $\delta^{18}O$ is statistically significant for the period from 700 BC to 1700 AD (taking into account long-term trends and serial dependence, Pearson's $r = 0.4$ within a 95% confidence interval [0.19; 0.6]; see Supplementary Notes). Our calculation of robust Mahalanobis distances, based on the dust, fluvial and marine mass accumulation rates separated into century bins, indicates that the uppermost two time intervals (1800– 1900 AD and 1900–2000 AD) are outlying with respect to the robust covariance structure of the GeoB9501 fluxes (see Supplementary Notes). In addition, from the eighteenth century onwards, the observed relation between continental precipitation and dust deposition breaks down as the two processes appear to become, at least partially, decoupled (Fig. 3).

Modern dust generation in the Sahel has been related to continental precipitation [*Prospero and Lamb,* 2003] and human activity [*Mahowald et al.,* 2002]. The degree of human-induced dust mobilization in the Sahel is, however, controversial. Our data support the dominant role of continental precipitation for the period from 600 BC to 1700 AD. The increase in dust accumulation after about 1700 AD cannot be interpreted exclusively by a decrease in precipitation over West Africa. After about 1700 AD precipitation increases to intermediate levels again, whereas the dust deposition continues to increase towards the present, at rates unprecedented during the preceding three millennia. Although the drought in the 1970s and 1980s was devastating and substantially contributed to increased atmospheric dust concentrations in the last decades [*Prospero and Lamb,* 2003], it did not reach the magnitude of past multicentury-long droughts [*Shanahan et al.,* 2009], which resulted in the water level of Lake Bosumtwi dropping by more than 30 m.

The departure of the dust deposition from its long-term relation to precipitation coincides with a marked change in the agricultural regime in the western Sahel. Maize, introduced by the Portuguese, was a dominant crop of the early eighteenth century and was gradually replaced by the low-yielding millet and sorghum in the mid- eighteenth century [*Webb,* 1995] (Fig. 2a). The steepest increase in dust deposition, however, parallels the advent of commercial agriculture in Senegal, Nigeria and Gambia in the mid nineteenth century, the so-called ''cash crop revolution'' [*Austin,* 2009; *Webb*, 1995]. Groundnuts were introduced to

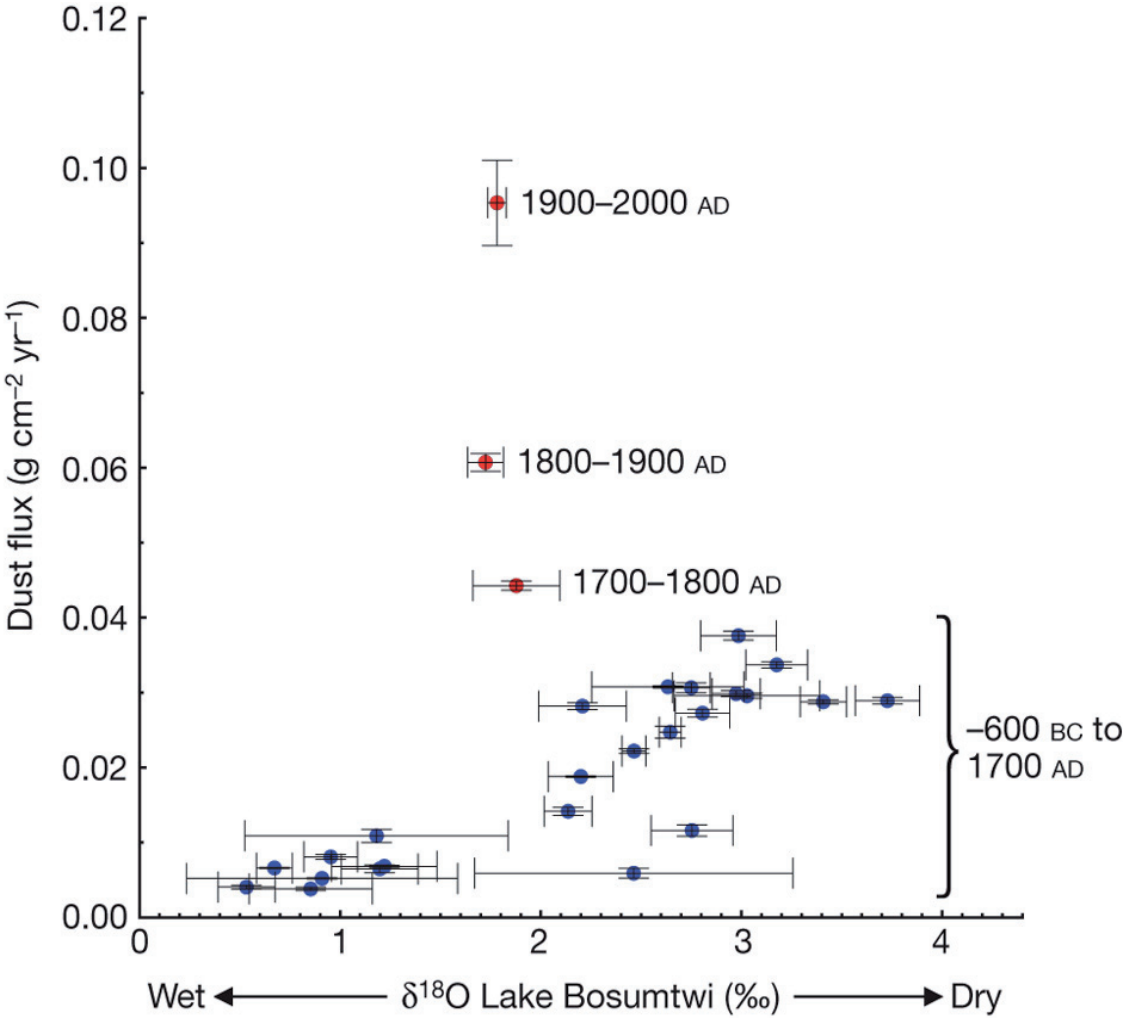

Figure 3. Relationship between δ^{18}O of authigenic carbonates from Lake Bosumtwi [*Shanahan et al.*, 2009] and dust deposition flux at site GeoB9501.
Low δ^{18}O values denote wet conditions over West Africa. The positions of the 100-year interval bins refer to their median values, while the displayed error bars represent the standard errors on the medians. For the unbinned data a significant linear correlation exists between dust flux and δ^{18}O between 700 BC and 1700 AD (blue dots represent this time interval in the binned data; see Supplementary Notes). Based on the calculation of robust Mahalanobis distances from the GeoB9501 flux data, the bins spanning 1800–1900 AD and 1900–2000 AD do not follow the robust pattern of the dust, fluvial and marine mass accumulation rates and can be deemed to be outlying (Supplementary Notes). In terms of their relationship to conditions over West Africa, the two youngest bins are characterized by apparently high dust production for the given level of precipitation.

Senegal in 1840 and caused a rapid expansion of agricultural lands, encroachment on forests and woodlands and exposure of the soil to wind erosion [*Mbow et al.*, 2008; *Sterk,* 2003]. In the early twentieth century, agricultural export economies were common in the West African Sahel [*Austin,* 2009], a few hundred kilometres to the south of the modern centres of dust production (Fig. 1) and consistent with a southward shift of the economic centres of export production [*Webb,* 1995]. It is plausible that the increased human-induced dust production also contributed to locally drier conditions in the Sahel by reducing the

monsoonal rainfall via a direct cooling of the surface [*Solmon et al.,* 2008; *Yoshioka et al.,* 2007]. This process could enhance the observed decoupling of the precipitation in tropical West Africa and Sahelian dust generation that has prevailed since the eighteenth century (Fig. 2a) and which would explain the continuous desertification trend in the Sahel over the past four centuries, reported in historical sources [*Webb,* 1995].

Satellite data suggest no systematic trend in desertification [*Tucker et al.,* 1991] and human dust mobilization from 1980 to the present. Our data show that a considerable increase in African dust emissions occurred with the onset of agricultural irrigation of Sahelian soils about two centuries ago and therefore too early for instrumental detection.

Supplementary Information is linked to the online version of the paper at www.nature.com/nature.

Acknowledgements

Radiocarbon datings were performed at the Leibniz-Laboratory for Radiometric Dating and Stable Isotope Research in Kiel and at the Poznan Radiocarbon Laboratory. This work was funded through the DFG Research Center/Cluster of Excellence ‘‘The Ocean in the Earth System’’. We thank M. Prange for plotting the TOMS data in Fig. 1 and U. Röhl, K. Enneking, V. Lukies and M. Klann for technical support.

Supplementary Methods

Age control of GeoB9501-4/5

The age model for multicore GeoB9501-4 and gravity core GeoB9501-5 was developed using a combination of two independent radiometric methods, i.e., $^{210}Pb_{xs}$- and ^{137}Cs-measurements applying the constant rate of supply (CRS) model [*Appleby and Oldfield,* 1978], and AMS radiocarbon dating of planktic foraminifera (Supplementary Table 1). The details of the $^{210}Pb_{xs}$ and ^{137}Cs gamma spectroscopic measurements are described elsewhere [*McGregor et al.,* 2007; *Pittauerová et al.,* 2009]. Additionally, the self attenuation correction for low-energy ^{210}Pb (45.6 keV, Iγ 4.25%) for the multicore GeoB9501-4, necessary due to varying sample size, was calculated using a modification of the method described in *Hurtado et al.* [2007], combining both experimental measurements and mathematical Monte Carlo (MC) simulations. In this study, the full-energy peak efficiencies for samples with zero density with different sample heights were generated using the MC based LabSOCS Genie 2000 calibration tool [*Bronson,* 2003]. ^{210}Pb and ^{137}Cs were also measured for the associated gravity core GeoB9501-5. Here, due to constant geometry of the samples, no individual self-absorbtion correction was applied for ^{210}Pb. Depth matching of the gravity core and the multicore was performed using the corresponding $^{210}Pb_{xs}$ and ^{137}Cs profiles. The onset of ^{137}Cs corresponds to a depth of 29.5 cm in multicore GeoB9501-4 and to a depth of 8 cm in gravity corer GeoB9501-5. Hence, about 21.5 cm of sediment material was lost during gravity coring (Supplementary Figure 1).

The availability of a $^{210}Pb_{xs}$-based age model for the multicore spanning the time period between 1915 and 2005 CE allowed the estimation of the local radiocarbon reservoir age using the AMS ^{14}C-date of a foraminifera sample from the bottom of a parallel core (45.5 cm) from the same multicorer cast. From the $^{210}Pb_{xs}$-based age model, we estimate that this core depth corresponds to about 1907 CE. The AMS-measurement for sample KIA35172 performed in 2008 yielded a fMC value of 0.9235 ±0.0036, which was converted to $\Delta\,^{14}C$= -82.956‰ using:

$$(1) \qquad \Delta^{14}C\ (‰) = (fMC / e^{(t-1950/8267)} -1) * 1000$$

where t is the year of measurement. Subsequently, the radiocarbon concentration of the sample at the time of deposition (initial $\Delta^{14}C$) was determined using:

$$(2) \qquad \Delta^{14}{}_{Cinitial}\ (‰) = ((\Delta^{14}C/1000+1)*e^{(\lambda\Delta t)}-1)*1000$$

where λ is the decay constant (ln(2)/5730 yr) and Δt is the time elapsed between the year of deposition and the year of measurement in years. This initial radiocarbon concentration can be converted into the reservoir age (R) using a rearrangement of (1) given as:

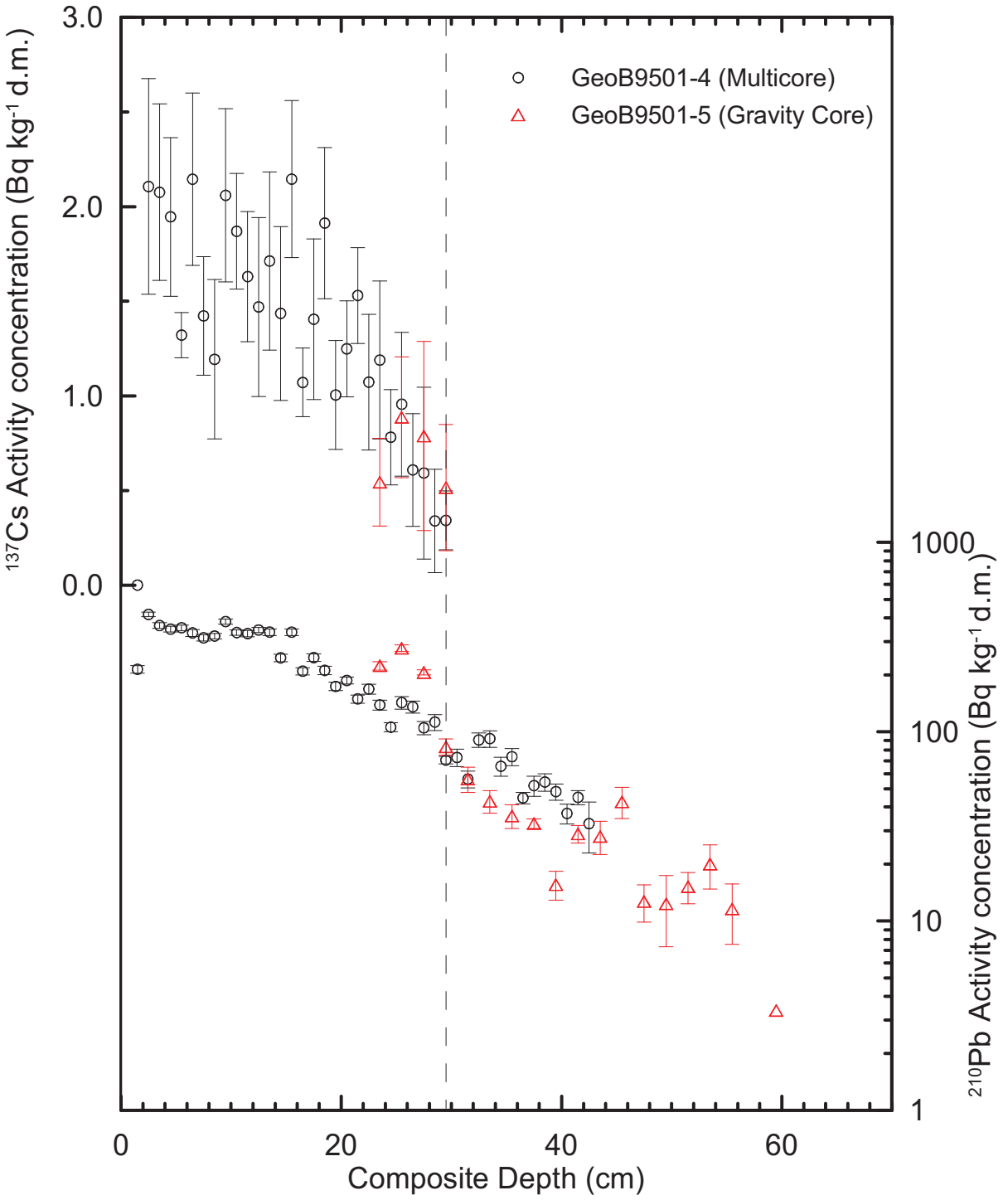

Supplementary Figure S1
Matched multicore (circles) and gravity core (triangles) depth profiles of activity concentrations of ^{137}Cs and $^{210}Pb_{xs}$ (log_{10} scale) in sediment dry mass (d.m.). About 21.5 cm of sediment have been lost during coring. All sampling depths in gravity core GeoB9501 have been corrected by +21.5 cm.

(3) $fMC = (\Delta^{14}C_{initial}/1000+1) * e^{(t-1950/8267)}$

and

(4) $R = -8033 * \ln(fMC)$.

For GeoB9501-4 we thus determined a reservoir age for the early 20th century of R = 541 yr. This reservoir age (ΔR=140 years) was used for calibration of the AMS radiocarbon dates of gravity core GeoB9501-4. We assumed a constant reservoir age throughout the time period covered by the sediment record. Radiocarbon ages were converted into calibrated 2σ calendar age ranges using the online calibration tool Calib 5.0.2 (http://radiocarbon.pa.qub.ac.uk/calib/calib.html) with the MARINE04 calibration curve and an additional local reservoir effect of 140 (± 100) years. Two radiocarbon ages were not included in the final age model because of questions concerning their fidelity. The radiocarbon age at 52 cm stems from the Little Ice Age for which models suggest a considerably higher reservoir effect for the core location (see *Franke et al.,* [2008] and http://www.reservoirage.uni-bremen.de) and where a plateau in the calibration curve produces ambiguous results. The age at the base of the gravity core at 530 cm (not plotted in Supplementary Figure 2) was not included because of possible disturbance and potential inclusion of older material from the core catcher.

To construct a continuous depth-age model for the multicore and gravity core, a weighted fourth-order polynomial function was fitted to the pooled $^{210}Pb_{xs}$ and calibrated radiocarbon ages in a least-squares sense. Each point was weighted by σ^{-2}, where σ represents the standard deviation of the point's age distribution. Assigning *d* to represent the composite core depth in centimeters the function to calculate the age *A* in yrs CE is given by:

$A = -8.625 \times 10^{-8} d^4 + 7.715 \times 10^{-5} d^3 - 0.0249 d^2 - 1.379 d + 2.008 \times 10^3$

The uncertainties on the individual ages were transformed into errors on the weighted polynomial coefficients [*Gubbins,* 2004; *Teanby,* 2007]. To determine a continuous sedimentation rate the reciprocal of the derivative of the weighted polynomial was calculated by a linear transform applied to the polynomial coefficients [*Teanby,* 2007]. The same transform also allowed the errors on the polynomial coefficients to be mapped to provide a ± 2σ error envelope on the sedimentation rate (Supplementary Figure 2).

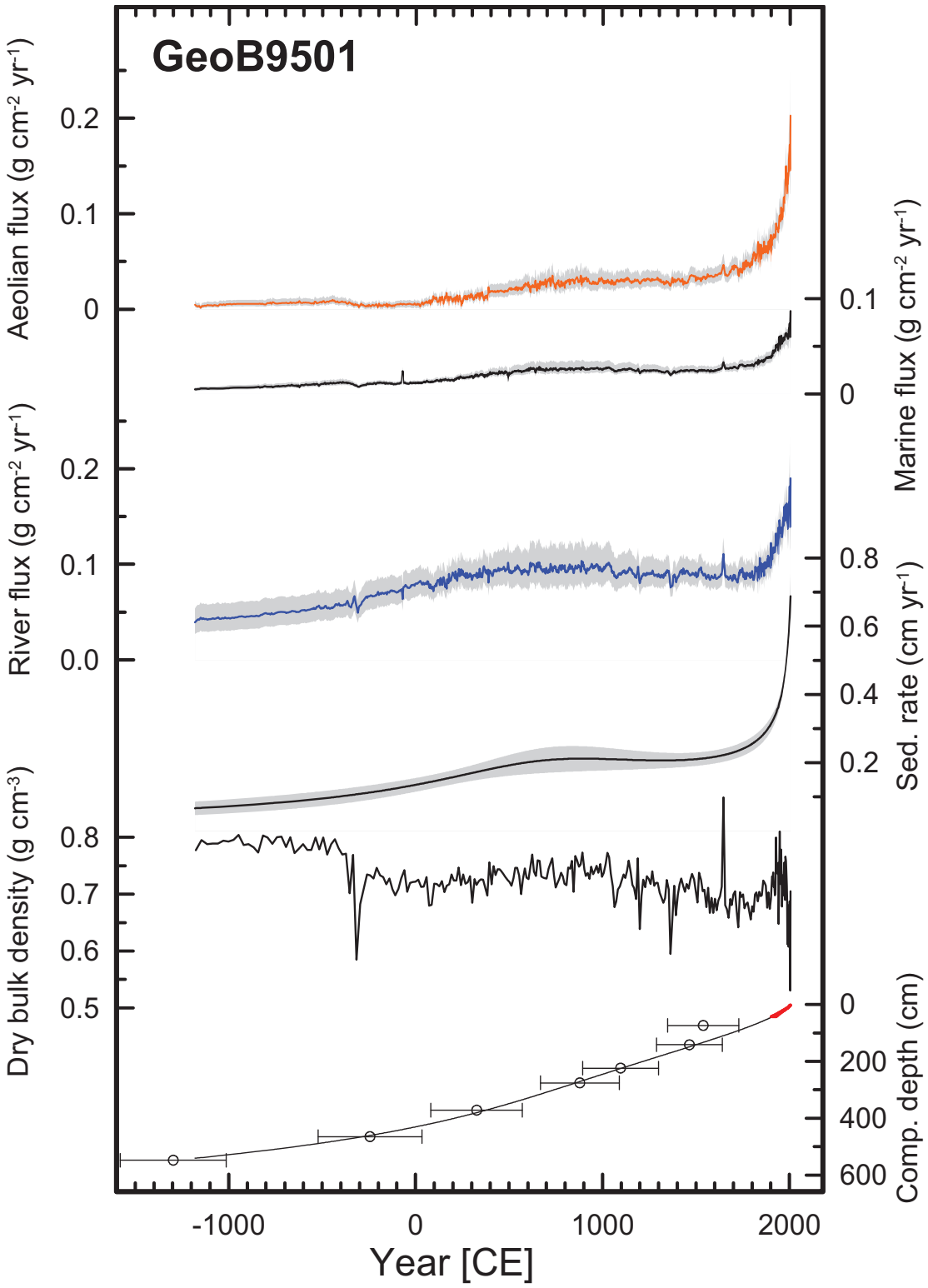

Supplementary Figure S2
Accumulation rates of aeolian, riverine and marine material in addition to total sedimentation rate, dry bulk density and modelled age-depth relation for Site GeoB9501. Grey shading indicates 95% nonparametric error envelope for flux estimations and 2σ error envelope for sedimentation rate. Error bars indicate 2σ age range for the conversion of radiocarbon ages into calibrated calendar years. Red line indicates 2σ error envelope of $^{210}Pb_{xs}$-based age model.

Supplementary Table S1: Radiocarbon age control points at site GeoB9501. Samples given with single depths denote depth intervals sampled with cut syringes of about 1.5 cm diameter centred over the given depth.

Depth (cm)	Core (GeoB)	Lab Code	Conv. Age (yr BP)	Age Range (2σ, CE)		
45-46	9501-4	KIA 35172*	640 ± 30 BP		-	
4-5	9501-5	KIA 32642**	-30 ± 70 BP		-	
52	9501-5	Poz-31132***	910 ± 40 BP	1348	–	1730
120	9501-5	KIA 3743	1040 ± 30 BP	1289	–	1640
202	9501-5	KIA 3744	1440 ± 30 BP	894	–	1299
254	9501-5	KIA 3745	1655 ± 30 BP	668	–	1089
350	9501-5	KIA 3746	2195 ± 30 BP	82	–	571
443	9501-5	KIA 3747	2675 ± 35 BP	-522	–	33
524-528	9501-5	KIA 32641	3540 ± 45 BP	-1581	–	-1013
530	9501-5	KIA 3748****	4130 ± 40 BP		-	

* Radiocarbon age from base of parallel core from multicore GeoB9501-4 used to derive reservoir age

** Radiocarbon age from 4-5 cm depth in gravity core GeoB9501-5 biased by bomb radiocarbon

*** Not included into the age model because of a larger reservoir age during the Little Ice Age (see text Age Control of GeoB9501-4/5)

**** Not included into the age model because of disturbance and potential inclusion of older material around the core catcher

Supplementary Table S2: Opal content for selected depths in core GeoB9501 measured by automated

Depth (cm)	Core (GeoB)	Opal Content (wt %)
2-3	9501-4	1.30
20-21	9501-4	1.75
40-41	9501-4	0.50
76	9501-5	1.18
102	9501-5	1.71
134	9501-5	0.55
186	9501-5	1.76
254	9501-5	4.70
304	9501-5	1.89
344	9501-5	0.69
432	9501-5	0.78
456	9501-5	0.84
508	9501-5	2.37

leaching [*Müller and Schneider,* 1993]. Single depths denote depth intervals sampled with cut syringes of about 1.5 cm diameter centred over the given depth.

Determination of grain size and bulk elemental concentrations

Grain size on the terrigenous fraction was determined with a Coulter Laser Particle Sizer LS200 every 2 cm downcore in the gravity core GeoB9501-5 and every cm in multicore GeoB9501-4. The pre-treatment steps to remove different biogenic constituents are described elsewhere [*Mulitza et al.,* 2008].

Element concentrations were determined on 53 sediment samples from gravity core GeoB9501-5 and on 42 sediment samples from multicore GeoB9501-4 (Supplementary Figure 3).

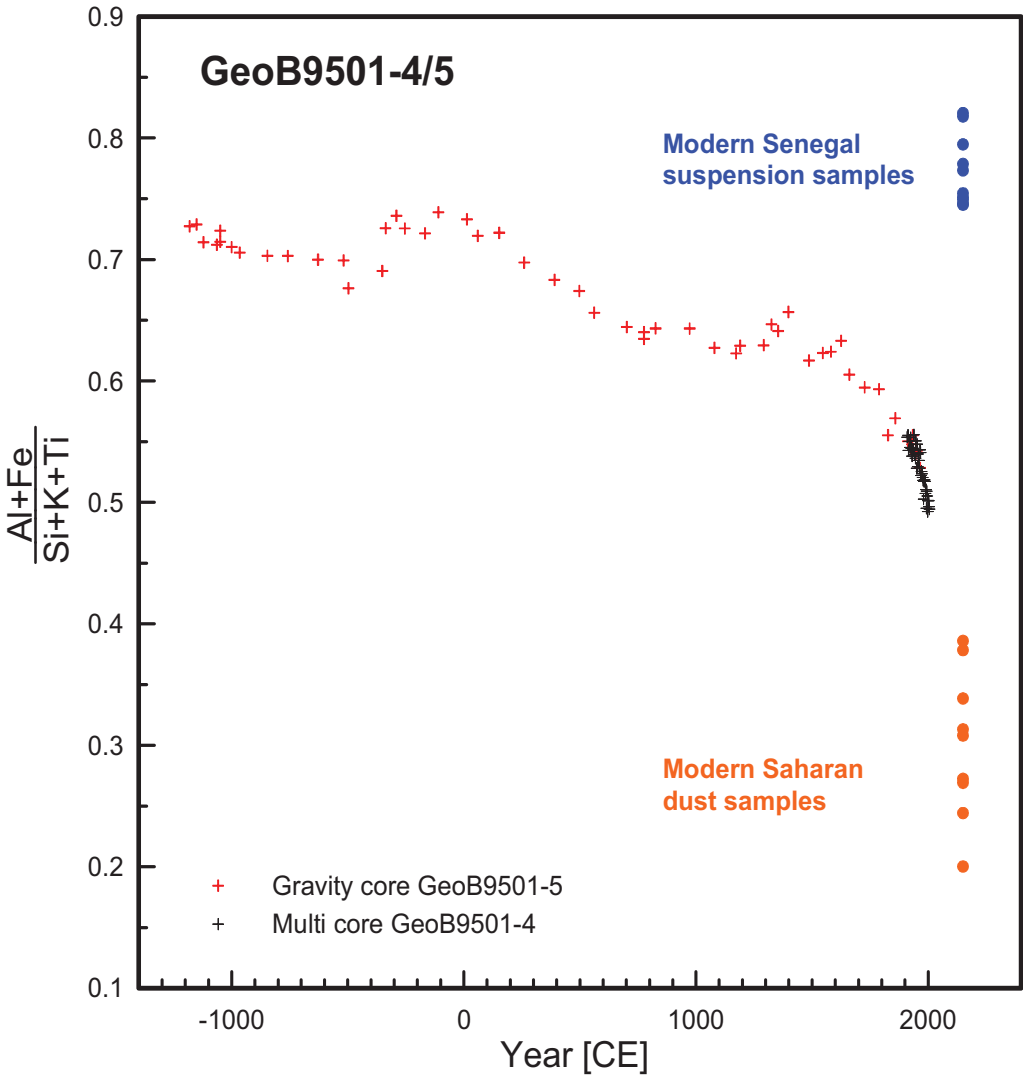

Supplementary Figure S3

Downcore variation of the ratio (Al+Fe)/(Si+K+Ti), measured on powdered bulk sediment samples of multi corer GeoB9501-4 (black crosses) and gravity corer GeoB9501-5 (red crosses). Bulk samples have been used to calibrate XRF scanner measurements. (Al+Fe)/(Si+K+Ti) ratios of nine modern aeolian samples47 (orange dots) and ten Senegal suspension samples 48 (blue dots) have been used to constrain the modern endmember compositions of atmospheric dust and riverborne sediments.

Bulk samples were freeze-dried, powdered and homogenised. Single element concentrations were determined on 4g of dry subsamples by energy-dispersive polarisation X-ray fluorescence (EDP-XRF) spectroscopy using a Spectro Xepos instrument [*Wien et al.,* 2005]. The instrument was operated by means of the software Spectro X-Lab Pro, Version 2.4, using the Turboquant method [*Schramm and Heckel,* 1998]. Analytical quality was assessed by repeated analyses of the certified standard reference material MAG-1 [*Govindaraju,* 1994]. The measured values were within 1% of the accepted value for Si, Al, K, Ca and Fe and within 2% for Ti. The standard deviation of replicates was less than 2%.

Calibration of the Avaatech XRF core scanner data

Element intensities were measured on gravity core GeoB9501-5 with an Avaatech XRF core scanner every 0.5 cm downcore as previously described [*Tjallingii et al.*, 2007]. Data from the XRF core scanner were calibrated by comparison to the element concentrations of the 53 powdered sediment samples taken along the length of the GeoB9501-5 core. In the original calibration method [*Weltje and Tjallingii,* 2008] a set of calibration equations are determined in log-ratio space by examining the regression relationships between the compositions obtained for powder samples measured on a calibrated XRF instrument and the XRF spectra measured on the scanner. The derived calibration equations are then applied to the scanner data across the entire core to yield elemental concentrations which take into account changes in specimen effects (including variable water content) and matrix effects. A detailed investigation revealed that such a global calibration was inappropriate in the case of core GeoB9501-5, thus an alternative local model was adopted. Calibration equations, typically spanning ~40 cm, were determined and applied in a piecewise manner through the core (the exact local domain size depending on the spacing of the reference samples). In order to compensate for slight depth mismatches between the scanner and powder measurement data sets, the scanner data were smoothed using a moving average filter in log-ratio space with a span of 5 cm. The final calibration, however, was applied to the unsmoothed scanner data.

Determination of dust, riverine and marine mass accumulation rates

In order to evaluate the relative abundances of aeolian, fluvial and marine material in the GeoB9501 sediments an end-member unmixing analysis was performed [*Ehrlich and Full,* 1987]. *End-member analysis* aims to provide a simplified low-rank approximation of a data set in terms of invariant parts. For this study, which involves a collection of sediment elemental compositions, end-members represent a small number of fixed compositions that when mixed together in various proportions can reproduce the measured data set.

To construct the mixing model four different matrices must be defined, ***X, A, S*** and ***ε***. The measured data can be placed in a matrix ***X***, which is composed of **n** rows, one for each sediment sample, and ***l*** columns spanning the suite of elements to be included in the analysis. The compositions of the end-members are based on measured data (see below) and define the matrix ***S***, which has ***m*** rows, one for each end-member and ***l*** columns spanning the elements as the data in ***X***. It is important that each row of ***X*** and ***S*** is normalized to sum to one, this does not imply that the studied sediments and end-members contain no other elements than those selected in the analysis, but instead it creates a consistent normalized data structure where the relative abundances of the elements in a given sample are preserved. The unknown relative abundances of the end-members are held in the matrix, ***A***, again with *n* rows (one for each of the measured samples) and ***m*** columns (one for each end-member). Finally, there will always be differences between the measured and modelled data, these "errors" can be held in the matrix ***ε*** which will have the same size as ***X***, ***n*** by ***l***. Given these definitions the linear mixing model can be represented in matrix notation as:

$$\boldsymbol{X} = \boldsymbol{AS} + \boldsymbol{\varepsilon}$$

This mixing model acts to link one set of observations, the input end-members in ***S***, to the measured samples under investigation in ***X***. In the case of the above mixing equation, this linking model is ***A***, the relative abundances of the end-members in each sample, which can be found simply by solving a constrained least squares problem (see below).

Candidate dust and fluvial end-members were constructed using the normalized relative abundances of Si, Al, Ti, K and Ca from modern aeolian [*Moreno et al.,* 2006] (nine samples) and riverborne [*Gac and Kane,* 1986] material (ten samples). Note that although it was included in the elemental calibration procedure, Fe was not included in the unmixing analysis because of concerns over its possible mobility resulting from redox processes. As an example of the method, to construct one realization of the *dust* end-member a combination of nine samples was selected from the aeolian data set by a bootstrap with replacement routine (where "replacement" indicates that a given sample can be selected more than once in any single realization). The *dust* end-member was then represented by the central composition of the nine selected samples, determined using the additive log-ratio approach [*Aitchison,* 1989]. The composition of the *marine* end-member was based on measurements of opal at selected points in the GeoB9501 record to assess the biogenic Si content (Supplementary Table 2) and the assumption across the five selected elements that biogenic Ca would be by far the most abundant whilst the content of Al, Ti and K would be effectively zero [*Schulz and Zabel,* 2006]. On this basis the *marine* end-member was constructed as having a normalized relative composition of 2% Si and 98% Ca. To reiterate the ideas discussed above, this composition does not imply that the marine

component will be composed solely of Si and Ca, because organic carbon, for example, could be expected to make a contribution. Instead the 2% Si and 98% Ca represents the normalized relative composition across the suite of five elements (Si, Al, Ti, K and Ca) included in the unmixing model. Numerical experiments showed that long-term evolution of the record was insensitive to small changes in the assumed *marine* end-member composition, with less than a 0.5% average change in the calculated abundance of the *marine* end-member when the Si contribution was changed from 0 to 5%.

The construction of end-members in the above manner assumes that their composition was approximately constant during the investigated period. It is however important to consider possible violations to this assumption, for example, the primary source area of the aeolian material may have shifted through time. By taking into consideration the composition of aeolian and riverine material over a wide geographical region and constructing spectra of end-member compositions via bootstrapping we aim to incorporate variability due to the possibility of shifting source areas into the uncertainty of the unmixing results. In turn, this uncertainty can subsequently be propagated into the calculation of mass accumulation rates.

Given bootstrapped realizations of the *dust* and *fluvial* end-members and the constructed *marine* end-member, their relative abundance in the sediment was determined using non-negative least squares applied to each calibrated XRF core scanner composition to provide an estimate of $\boldsymbol{A}$ via the presented mixing equation. This analysis was performed using the SeDuMi optimization package [*Sturm,* 1999] with the additional constraints that each contribution must be non-negative and the combined contributions of the *dust*, *fluvial* and *marine* end-members must sum to 100%. The supervised unmixing procedure was repeated with 500 different realizations of the end-members. The mean end-member relative contributions were calculated as a function of age using the additive log-ratio approach [*Gac and Kane,* 1986] which takes into account the relative and constrained nature of the data. In order to provide an appreciation of the variability introduced into the unmixing procedure by the bootstrapping, the minimum and maximum relative contributions obtained over the assemblage of 500 unmixing models were used to define an uncertainty envelope as a function of age.

Dry bulk density was determined by weighing wet samples and subsequently freeze-drying and re-weighing samples every 2 cm downcore in gravity core GeoB9501-5 and every cm in multicore GeoB9501-4. To determine the mass accumulation rates (expressed in g cm^{-2} yr^{-1}) of the three end-members their mean relative contributions were multiplied by the product of the sedimentation rate and the dry bulk density interpolated at the sample depths. An error envelope was constructed by repeating this procedure for the relative contributions obtained for all 500 unmixing models and propagating in the 2σ error for the sedimentation rate. From the

distribution of results at each given depth interval the 2.5th and 97.5th percentiles were defined to provide a 95% nonparametric error envelope (shaded regions in Supplementary Figure 2).

Supplementary Notes

Determination of mass accumulation rate derivatives

Cubic smoothing splines [*de Boor,* 1978] were employed to approximate each of the *dust*, *riverine* and *marine* mass accumulation rate curves. The level of smoothing was selected to capture the long-term evolution of the record whilst removing the higher frequency variability. The derivative of each spline was calculated directly from its coefficients (Supplementary Figure 4).

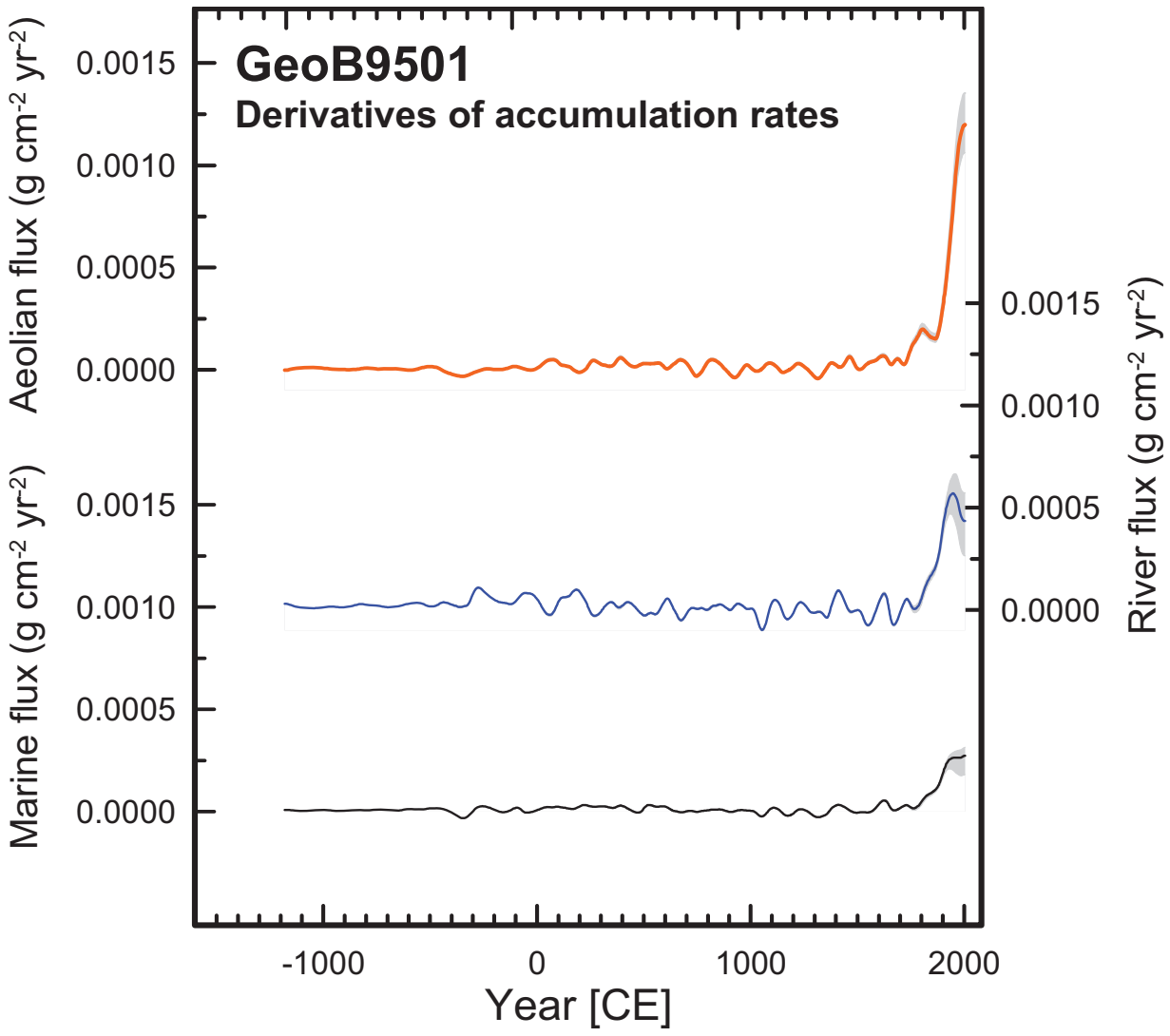

Supplementary Figure S4
Derivatives of deposition flux rates of aeolian, riverine and marine matter.

An error envelope was constructed by repeating this procedure for the mass accumulation rates obtained from all 500 realizations of the unmixing procedure. The 2.5th and 97.5th percentiles were determined from the distribution of derivative curves for each component at each time interval to provide a 95% nonparametric error envelope.

Outlier analysis of the mass accumulation rate data

According to their ages, data from the dust, riverine and marine mass accumulation rates were assigned to bins 100 years in width. The median value of the data within each bin was determined and the standard error on the median was estimated [*Sachs,* 2002]. To test for a changing relationship between the dust, riverine and marine mass accumulation rates the robust Mahalanobis distance [*Maronna et al.,* 2006] of each age interval was determined with respect to the group of all age intervals on the basis of the estimated covariance structure of

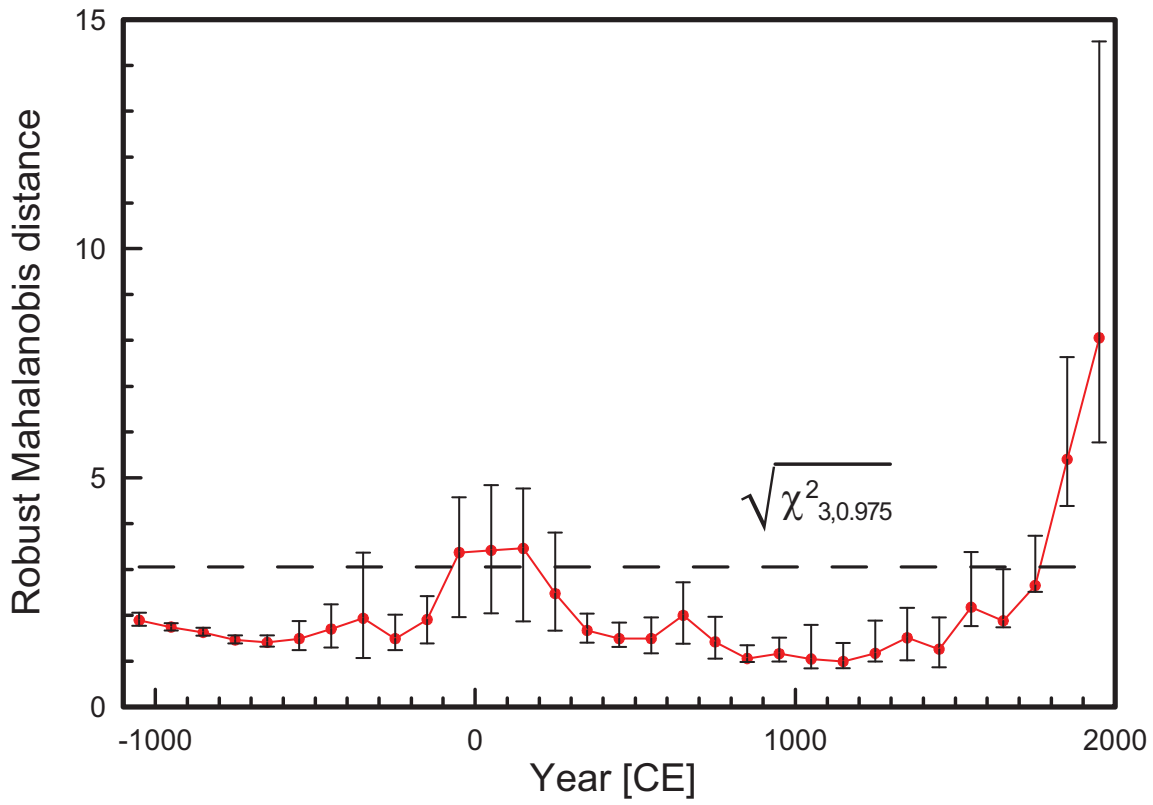

Supplementary Figure S5
The robust Mahalanobis distances of the binned GeoB9501 mass accumulation rate data. A cut-off value (dashed line) with which to define outlying points was obtained from a chi-squared distribution at the 97.5% quantile with three degrees of freedom. The error bars on the individual time points represent the 95% error envelope obtained by numerical propagation of the standard errors on the bins into the distance calculation. The two youngest bins, positioned at 1850 and 1950 CE, can be deemed to be outlying.

the binned data [*Filzmoser and Hron,* 2008] (Supplementary Figure 5). Thus, the Mahalanobis distance considers the covariance of the data, taking into account correlations whilst being scale invariant. Outlying bins were defined by a cut-off value representing the 97.5% tolerance level obtained from a chi-squared distribution with three degrees of freedom [*Rousseeuw and van Zomeren,* 1990]. Bins with distances greater than the cut-off limit of $\sqrt{\chi^2_{3,0.975}}$ can be said to demonstrate atypical behaviour with respect to the robust covariance structure of the data. A 95% error envelope for the robust Mahalanobis distances was determined by numerical propagation of the standard error on the median of each bin. Based on the cut-off value, the 2 youngest bins (centred at 1850 and 1950 CE) can be deemed to be outlying. It is thus apparent that the relationship between the dust, riverine and marine mass accumulation rates at the core location changed fundamentally at some time around 1750-1850 CE.

Correlation between mass accumulation rates and Lake Bosumtwi $\delta^{18}O$

To investigate the relationship between the reconstructed mass accumulation rates and the Lake Bosumtwi $\delta^{18}O$ record a correlation analysis was performed using the software PearsonT [*Mudelsee,* 2003] which takes into account the serial dependence and non-normal distribution of the signals. For this purpose we resampled the higher-resolution mass accumulation rate records at the ages of the lower-resolution Lake Bosumtwi $\delta^{18}O$ time series using linear interpolation and then detrended each record (including Lake Bosumtwi) linearly. For the time interval 700 BCE to 1700 CE (n=291) Pearson's ***r*** is 0.40 with a 95% confidence interval [0.19; 0.60] for $\delta^{18}O$ vs. aeaolian flux, 0.39 [0.25; 0.52] for $\delta^{18}O$ vs. riverine flux and 0.51 [0.26; 0.61] for $\delta^{18}O$ vs. marine flux.

Comparison of dust fluxes at Site GeoB9501 to sediment trap data

Sediment trap studies off NW Africa show that the seasonal dust input is reflected in the lithogenic flux in the water column [*Bory and Newton,* 2000]. The observed dust flux in those traps is around 0.0022 g cm^{-2} yr^{-1} and hence by a about factor 50 to 70 lower than observed for the years 1984 to 1988 at Site GeoB9501. However, we have to take into account that the dust flux strongly decreases with increasing distance from the coast [*Goudie and Middleton,* 2001]. The nearest sediment trap site is about 500 km west of the African coast (Eumeli Site, [*Bory and Newton,* 2000]). Site GeoB9501 is located about 30 km to the west of Mauritania and in close proximity to dust sources on land. Dust fluxes at observatories in Dakar [*Orange and Gac,* 1990] and Malé [*Gassani et al.,* 2005] are about 0.021g cm^{-2} yr^{-1} (mean flux 1984-1988) and 0.031g cm^{-2} yr^{-1} (based on measurements in the time from 01.07.2005 to 30.09.2005) and hence still a factor of 3-5 lower than at site GeoB9501. Recently, however, it has been shown [*Goossens and Rajot,* 2008] that the catch efficiency of the CAPYR (capteur pyramidal) dust

sampler used in the studies [*Orange and Gac,* 1990; *Gassani et al.,* 2005] mentioned above underestimates the dust deposition by a factor of about 2-5 with respect to other techniques and further with respect to deposition on a water surface, where no resuspension is possible. We thus conclude that the relatively high dust fluxes recorded at Site GeoB9501 are not inconsistent with available dust-flux measurements at the nearest observatories in Africa in Dakar and Malé.

Note on River Fluxes

Although Senegal sediment discharge generally increases with water discharge [*Kattan et al.,* 1987] it is very likely that human influence and vegetation cover along the Senegal River also had a considerable influence on the total sediment load of the Senegal River due to erosional processes along the river. An increasing amount of water erosion structures (i.e., backward erosion, gullying, bank erosion) due to anthropogenic pressure on the vegetation cover has actually been observed along the Senegal River [*Niang et al.,* 2008] during the past 10 years. This explains why the accumulation rate of fluvial material also increased along with the increased land use (Supplementary Figure 2).

Note on Marine Fluxes

The reconstructed marine flux increases along with the dust flux increase during the past 300 years (Supplementary Figure 2). A covariation of biogenic and lithogenic fluxes has also been observed in sediment trap studies. For example in the Cape Blanc area, the flux of lithogenic components is tightly related to marine components [*Fischer et al.,* 2009] as organic carbon, carbonate and opal. This covariation can be explained by the Ballast-Effect [*Armstrong et al.,* 2009], the increase of the excess density of settling particles through lithogenic material which causes a faster and more efficient transfer of marine components to the sea floor.

Conclusions

The primary aims of this thesis were the investigations of short-term climate variations of the NW African continent over the last ~ 12 ka. The results of this study demonstrate that several short term climate variations occurred within the investigated time period, resulting in changes in the amount of fluvial versus aeolian sediment deposition as well as variations in isotopic ratios.
The outcome of this thesis will be discussed below in the light of the major scientific objectives (see Chapter 1):

> Is the investigation of terrigenous material found in marine sediment cores a reliable source of information to reconstruct paleoclimatic changes on decadal to millennial scale?

All key studies within this thesis are based on investigations of the terrigenous fraction, both fluvial and aeolian material, found in marine sediment cores offshore the presently largest desert in the world: the Sahara Desert. The results demonstrate that marine sediment cores along the NW African coast record the variations of terrigenous input from the African continent and therefore yields a detailed source of paleoclimatic information's, even on short-term scales. However, the data clearly show that care should be taken when using single sediment cores to reconstruct environmental conditions on land. Results from this study shows that the amounts and characteristics of the terrigenous fractions, and hence results of end-member models, yields huge variations between marine sediment cores from the same area.

> How do the terrigenous sediment supply and its distribution vary during the Holocene on a spatial and temporal scale?

The terrigenous sediment fraction of deep-sea sediments downwind of the Saharan Desert is characterized by a mixture of aeolian dust, delivered from the Sahara by different wind systems, and a fluvial component, delivered from either perennial rivers like the Senegal River, or ephemeral rivers and wadis. As shown by end-member modeling results the input of these two terrigenous components varies as a function of climate change on the NW African continent. During the YD a coarser median grain size, as well as an increase of the coarse dust end member, found at all core locations, point to arid conditions and an increased atmospheric circulation. In contrast, sediment transport by rivers was only moderate during the YD. Within mid-Holocene times, a decrease in median grain sizes and the dominance of the fluvial end member point to wetter conditions on land, enhanced sediment supply via rivers along the NW African coast and/or a denser vegetation cover in the source area. In late-Holocene times, a trend to coarser

median grain sizes and an increase of the fine dust end member indicates a transition to modern arid conditions, but an apparently far less windier environment than during the YD.

How did the atmospheric circulation and the prevailing climate regimes vary during the Holocene?

Results from the present study suggest that the transition between the North Atlantic climate system and the NW African monsoonal regime have not been constant throughout the Holocene, but moved latitudinally, resulting in variations in the amount of aeolian vs. fluvial sediment supply to the Atlantic Ocean. During the YD the entire NW African continent was characterized by arid conditions and intensified trade winds, resulting in the deposition of higher amounts of aeolian dust and coarser grain sizes in the investigated deep-sea sediments. Strontium isotopic measurements indicate a change in the source area of the terrigenous material north of 26°N during the YD. Enhanced wind intensities and a southward shift of atmospheric circulation patterns are able to transport material from more distal sources to the core sites. Contrary to the general interpretation, the YD fine fraction is not interpreted as a fluvial end member but a finer distal dust end member reaching the core locations only under changed atmospheric circulation patterns. This finding leads to the interpretation that the influence of the North Atlantic climate system reached as far south as 26°N during the YD. After the termination of the YD, NW African climate shifts to wetter conditions during the mid Holocene, characterized by an increase of the fluvial end member and a decrease in dust deposition in the marine sediments. Isotopic measurements from all cores south of 30°N confirm more humid conditions prevailed during the AHP than during recent times. Hence, during mid-Holocene times the boundary between both climate systems gradually shifted further north, possibly up to ~ 29°N. Within the late Holocene, an increase in dust reflects present-day arid climate. Isotopic measurements are in line with this interpretation, revealing dryer conditions compared to mid-Holocene times.

Is it possible to identify and quantify the source areas, using the terrigenous fraction?

Based on the isotopic composition of Sr and Nd, a number of differences in the sediment cores can be discerned, which line up according to latitude. Results of ε_{Nd} measurements indicate mainly two different source areas delivering terrigenous sediments to the Atlantic Ocean, the Atlas Mountains region in the North and the southern Sahara/Sahel region. Due to differences in their geological age and their lithology these two source areas yield different isotopic signatures, which is reflected in the marine sediment archive offshore NW Africa. Material derived from the Atlas Mountains (~ 65 Ma) results in more radiogenic ε_{Nd} values than material obtained from the Archaean and early to mid- Proterozoic crystalline basement rocks of the West African Craton (~ 2.0 Ga).

How do source regions of land-derived material change due to changes in the atmospheric circulation?

The minor change in the ε_{Nd} isotopic record for the period of investigation suggests changes in the intensity of the different sources but no major change in the geological source areas since the YD. Dominating geological source areas are the Atlas Mountains, with more radiogenic ε_{Nd} values, and the very old basement rocks of the West African Craton, with very unradiogenic ε_{Nd} values. However, low $^{87}Sr/^{86}Sr$ isotope ratios north of 26° N indicate a slight change in sediment source area during the YD. Due to an enhanced atmospheric circulation and higher wind speeds, material from more distal source areas with a different isotopic signal were transported to the study sites. This relatively complicated interpretation is based on the huge alterations within the Sr isotopic signal. After the termination of the YD no material from the distal source areas reaches the investigated core locations any longer due to weakened atmospheric circulation and hence weakened trade winds.

Is it possible to reconstruct the hydrological evolution within NW Africa by using isotopic fingerprinting?

Within this study it is demonstrated, that the isotopic composition of $^{87}Sr/^{86}Sr$ is a powerful tool to reconstruct the weathering regime and the hydrological conditions within the source region of the terrigenous material. The distinct changes in Sr isotope ratios are interpreted to reflect major changes in the evaporation/precipitation balance over the study area. $^{87}Sr/^{86}Sr$ isotope ratios suggest hyperarid conditions during the YD in the southern part of the study area. More humid conditions and intensified monsoonal rainfall are observed during the early and mid Holocene. In late-Holocene times, a decrease in the rate of chemical weathering indicates a return to arid conditions. In the northern part of the study area changes in the wind systems result in a “wetter” isotopic signal, from more distal source regions during the YD. Furthermore, the data presented in this study demonstrates that grain size has a significant impact on the isotopic composition of Sr. Consequently, investigations of bulk-sediment samples without grain-size separations are hard to interpret as the observed changes in isotopic values could simply be the result of changes in grain size due to varying input of dust and fluvial material.

To what extend do human activities influence the dust emission within the area?

The study shows that human activity influences dust emission through agriculture and changes in land-use in a region that is extremely sensitive to changes in precipitation. The data clearly show

an inverse linear relationship between precipitation and dust flux since 3 ka. This relationship becomes decoupled at the beginning of the nineteenth century, when both precipitation and dust flux increase, coinciding with the beginning of commercial agriculture in the area. The data show that human-induced dust production through land use exceeds natural dust production by far.

In summary, the results presented in this PhD thesis achieved the objectives and clearly demonstrate that terrigenous sediment supply offshore NW Africa is extremely vulnerable to climate change. Although the data provide new insights into the hydrological changes and the variability of source areas of the terrigenous fraction since the YD, a number of questions raised up during this study. Future studies should determine detailed investigations of the differences in the supply of fluvial and aeolian sediments along the NW African coast to gain further information about the local characteristics and the temporal development of climate changes over the entire NW Africa. In addition, downcore investigations of strontium and neodymium isotopes will help to examine more details of possible source areas as well as temporal changes over time. Isotopic investigations of on-shore sediment samples would help to further define these geological source areas and their evolution through time.

References

Åberg, G., et al. (1989), Weathering rates and $^{87}Sr/^{86}Sr$ ratios: An isotopic approach, *Journal of Hydrology,* 109(1-2), 65-78.

Adkins, J., et al. (2006), The "African humid period" and the record of marine upwelling from excess 230Th in Ocean Drilling Program Hole 658C, *Paleoceanography,* 21, PA4203.

Aitchison, J. (1989), *Measures of location of compositional data sets,* Math. Geol., 21, 787-790.

Armstrong, R. A., et al (2009), Settling velocity spectra and the ballast ratio hypothesis, *Deep-Sea Res. II,* 56, 1470-1478.

Austin, G. (2009), Cash Crops and Freedom: Export Agriculture and the Decline of Slavery in Colonial West Africa, *International Review of Social History,* 54(01), 1-37.

Appleby, P. G. and Oldfield, F (1978), The calculation of lead-210 dates assuming a constant rate of supply of unsupported 210Pb to the sediment, *Catena,* 5, 1-8.

Berger, A., and M. F. Loutre (1991), Insolation values of the last 10 million years, *Quaternary Science Reviews,* 10, 297-317.

Biscaye, P. (1965), Mineralogy and sedimentation of recent Deep-sea clay in the Atlantic Ocean and adjacent seas and oceans, *Geological society of America bulletin,* 76, 803-832.

Biscaye, P. E., et al. (1997), Asian provenance of glacial dust (stage 2) in the Greenland Ice Sheet Project 2 Ice Core, Summit, Greenland, *J. Geophys. Res.,* 102(C12), 26765-26781.

Bischoff, A. and T. Geiger (1995), Meteorites from the Sahara: Find locations, shock classification, degree of weathering and pairing, *Meteoritics,* 30, 113.

Blum, J. D., and Y. Erel (1997), Rb-Sr isotope systematics of granitic soil chronosequence: The importance of biotite weathering, *Geochimica et Cosmochimica Acta,* 61(15), 3193-3204.

Blum, J. D., and Y. Erel (2003), *Radiogenic Isotopes in Weathering and Hydrology,* in Treatise on Geochemistry, Vol.5 edited by J. I. Drever, Elsevier-Pergamon, Oxford.

Bond, G., et al. (2001), Persistent Solar Influence on North Atlantic Climate During the Holocene, *Science,* 294(5549), 2130-2136.

Borg, L. E., and J. L. Banner (1996), Neodymium and strontium isotopic constraints on soil sources in Barbados, West Indies, *Geochimica et Cosmochimica Acta,* 60(21), 4193-4206.

Bory, A. J. M. and Newton, P. P (2000), Transport of airborne lithogenic material down through the water column in two contrasting regions of the eastern subtropical North Atlantic Ocean, *Glob. Biogeochem. Cycles,* 14, 297-315.

Broecker, W. S. (2006), Abrupt climate change revisited, *Global and Planetary Change,* 54(3-4), 211-215.

Bronson, F. L. (2003), Validation of the accuracy of the LabSOCS software for mathematical efficiency calibration of Ge detectors for typical laboratory samples, *J. Radioanal. Nucl. Chem.,* 255, 137-141.

Brooks, N., et al. (2005), The climate-environment-society nexus in the Sahara from prehistoric times to the present day, *The Journal of North African Studies*, 10(3-4), 253–292.

Capo, R. C., et al. (1998), Strontium isotopes as tracers of ecosystem processes: theory and methods, *Geoderma,* 82(1-3), 197-225.

Caquineau, S., et al. (2002), Mineralogy of Saharan dust transported over northwestern tropical Atlantic Ocean in relation to source regions, *Journal of Geophysical Research*, 107(D15), 4251.

Carlson, T. N., and J. M. Prospero (1972), The Large-Scale Movement of Saharan Air Outbreaks over the Northern Equatorial Atlantic, *Journal of Applied Meteorology*, 11(2), 283-297.

Castañeda, I. S., et al. (2009), Wet phases in the Sahara/Sahel region and human migration patterns in North Africa, *Proceedings of the National Academy of Sciences,* 106(48), 20159-20163.

Chester, R., and L. R. Johnson (1971), Atmospheric dusts collected off the West African Coast, *Nature*, 229, 105-107.

Chiapello, I., et al. (1995), An additional low layer transport of Sahelian and Saharan dust over the North-Eastern Tropical Atlantic, *Geophysical Research Letters*, 22(23), 3191-3194.

Claussen, M., et al. (2003), Climate Change in Northern Africa: The Past is Not the Future, *Climatic Change,* 57(1), 99-118.

Cole, J. M., et al. (2009), Contrasting compositions of Saharan dust in the eastern Atlantic Ocean during the last deglaciation and African Humid Period, *Earth and Planetary Science Letters,* 278(3-4), 257-266.

Colin, C., et al. (2006), Evolution of weathering patterns in the Indo-Burman Ranges over the last 280 kyr: Effects of sediment provenance on 87Sr/86Sr ratios tracer, *Geochem. Geophys. Geosyst.,* 7(3), Q03007.

Collins, J. A., et al. (2010), Interhemispheric symmetry of the tropical African rainbelt over the past 23,000 years, *Nature Geosci,* 4, 42–45

Compston, W., et al. (1965), The rubidium-strontium age of the Bishopville aubrite and its component enstatite and feldspar, *Geochimica et Cosmochimica Acta,* 29(9), 1085-1099.

Cullen, H. M., et al. (2000), Climate change and the collapse of the Akkadian empire: Evidence from the deep sea, *Geology,* 28(4), 379-382.

Dallmeyer, R. D., and J. P. Lecorche (1991), *The West African Orogens and Circum-Atlantic Correlatives*, 405 pp., Springer, Berlin.

Dansgaard, W., et al. (1993), Evidence for general instability of past climate from a 250-kyr ice-core record, *Nature,* 364(6434), 218-220.

Dasch, E. J. (1969), Strontium isotopes in weathering profiles, deep-sea sediments, and sedimentary rocks, *Geochimica et Cosmochimica Acta,* 33(12), 1521-1552.

Davies, G.R., et al. (1989), A combined chemical and Pb-Sr-Nd isotope study of the Azores and Cape Verde hot-spots: the geodynamic implications, *Geological Society,* London, Special Publications, 42(1), 231-255.

Davies, G. R., et al. (1985), Upper crustal recycling in southern Britain: evidence from Nd and Sr isotopes, *Earth and Planetary Science Letters,* 75(1), 1-12.

De Boor, C. (1978), *A Practical Guide to Splines,* 325 pp., Springer, New York.

DeMenocal, P.B., et al. (2000a), Abrupt onset and termination of the African Humid Period: rapid climate responses to gradual insolation forcing, *Quaternary Science Reviews,* 19, 347-361.

DeMenocal, P.B., et al. (2000b), Coherent high- and low-latitude climate variability during the Holocene Warm Period, *Science,* 288, 2198-2202.

DeMenocal, P.B., and D. Rind (1993), Sensitivity of Asian and African Climate to Variations in Seasonal Insolation, Glacial Ice Cover, Sea Surface Temperature, and Asian Orography, *J. Geophys. Res.,* 98(D4), 7265-7287.

DePaolo, D. J. (1988), *Neodymium isotope geochemistry: an introduction,* 187 pp., Springer, New York.

Derry, L. A., and C. France-Lanord (1996), Neogene Himalayan weathering history and river 87Sr/86Sr: impact on the marine Sr record, *Earth and Planetary Science Letters,* 142(1-2), 59-74.

Diester-Haaß, L. (1981), Factors contributing to Late Glacial and Holocene sedimentation on the continental shelf and slope off NW Africa, Banc d'Arguin, 19ºN., *Meteor Forschungsergebnisse*, Reihe C, 35, 1-22.

Drake, N., and C. Bristow (2006), Shorelines in the Sahara: geomorphological evidence for an enhanced monsoon from palaeolake Megachad, *The Holocene,* 16(6), 901-911.

Ehrlich, R. and W.E. Full (1987), Sorting Out Geology – Unmixing Mixtures, in *Use and Abuse of Statistical Methods in Earth Sciences*, edited by W. Size, 33–46pp., Oxford University Press, Oxford.

Edmond, J. M. (1992), Himalayan Tectonics, Weathering Processes, and the Strontium Isotope Record in Marine Limestones, *Science,* 258(5088), 1594-1597.

Engelstaedter, S., et al. (2006), North African dust emissions and transport, *Earth-Science Reviews,* 79(1-2), 73-100.

Ennih, N., and J.-P. Liegeois (2008), The boundaries of the West African craton, with special reference to the basement of the Moroccan metacratonic Anti-Atlas belt, *Geological Society,* London, Special Publications, 297(1), 1-17.

Evan, A. T., et al. (2006), New evidence for a relationship between Atlantic tropical cyclone activity and African dust outbreaks, *Geophys. Res. Lett.*, 33(19), L19813.

Fabre J. and N. Petit-Maire (1988), Holocene climatic evolution at 22-23°N from two palaeolakes in the Taoudenni area (Northern Mali), *Palaeogeography, Palaeoclimatology, Palaeoecology*, 65, 3-4, pp. 133-148

Fagel, N., et al. (2002), Sources of Labrador Sea sediments since the last glacial maximum inferred from Nd-Pb isotopes, *Geochimica et Cosmochimica Acta,* 66(14), 2569-2581.

Faure, G., and J. L. Powell (1972), *Strontium isotope geology*, 197 pp. Springer, New York

Faure, G. (1986), *Principles of Isotope Geology,* 589 pp., Wiley & Sons, New York.

Feng, J.-L., et al. (2010), Variations in trace element (including rare earth element) concentrations with grain sizes in loess and their implications for tracing the provenance of eolian deposits, *Quaternary International,* 236 (1-2), 116-126

Filipson H. et al., 2011 (in press), Relationships between primary productivity and bottomwater oxygenation off NW Africa during the last deglaciation, *Journal of Quaternary Science*

Filzmoser, P. and K. Hron (2008), Outlier detection for compositional data using robust methods. *Math. Geosci.,* 40, 233-248.

Fischer, G. et al. (2009). Mineral ballast and particle settling rates in the coastal upwelling system off NW Africa and the South Atlantic, *Int. J. Earth Sci*., 98, 281-298.

Folland, C. K., et al. (1986), Sahel rainfall and worldwide temperatures, 1901-85, *Nature,* 320, 602-606.

Fontes, J. C., and F. Gasse (1991), Chronology of the major palaeohydrological events in NW Africa during the late Quaternary: PALHYDAF results, *Hydrobiologia,* 214(1), 367-372.

Frank, M. (2002), Radiogenic isotopes: Tracers of past ocean circulation and erosional input, *Rev. Geophys.,* 40(1), 1001.

Franke, J. et al., (2008), Modeling variations of marine reservoir ages during the last 45 000 years, *Clim. Past.,* 4, 125-136.

Franzén, L. (1989), A Dustfall Episode on the Swedish West Coast, October 1987, Geografiska Annaler. Series A, *Physical Geography,* 71(3/4), 263-267.

Freudenthal, T., et al. (2002), Upwelling intensity and filament activity off Morocco during the last 250,000 years, *Deep Sea Research Part II:* Topical Studies in Oceanography, 49(17), 3655-3674.

Gac, J. Y., and A. Kane (1986), Le fleuve Senegal: I. Bilan hydrologique et flux continentaux de matieres particulaires a l'embouchure, *Sci. Geol. Bull.*, 39, 99–130.

Gassani, J. et al., (2005), Preliminary results of Saharan dust deposition during the rainy season 2005 in Mâle (Southern Mauritania), *Geo-Eco-Trop,* 29, 69-76.

Gasse, F. and E. Van Campo (1994), Abrupt post-glacial climate events in West Asia and North Africa monsoon domains, *Earth and Planetary Science Letters,* 126(4), 435-456.

Gasse, F. (2000), Hydrological changes in the African tropics since the Last Glacial Maximum, *Quaternary Science Reviews,* 19, 189-211.

Gasse, F., et al. (1990), The arid–humid transition in the Sahara and the Sahel during the last deglaciation, *Nature,* 346(6280), 141-146.

Gasse, F. (2002), Diatom-inferred salinity and carbonate oxygen isotopes in Holocene waterbodies of the western Sahara and Sahel (Africa), *Quaternary Science Reviews*, 21(7), 737-767.

Giannini, A., et al. (2003), Oceanic forcing of Sahel rainfall on interannual to interdecadal time scales, *Science,* 302, 1027-1030.

Giles, J. (2005), Climate science: The dustiest place on Earth, *Nature*, 434(7035), 816-819.

Glaccum, R. A., and J. M. Prospero (1980), Saharan aerosols over the tropical North Atlantic - mineralogy, *Marine Geology,* 37(3-4), 295-321.

Goldstein, S. L., and R. K. O'Nions (1981), Nd and Sr isotopic relationships in pelagic clays and ferromanganese deposits, *Nature,* 292(5821), 324-327.

Goldstein, S. L., et al. (1984), A Sm-Nd isotopic study of atmospheric dusts and particulates from major river systems, *Earth and Planetary Science Letters*, 70(2), 221-236.

Goudie, A. S., and N. J. Middleton (2001), Saharan dust storms: nature and consequences, *Earth-Science Reviews,* 56(1-4), 179-204.

Goudie, A. S., and N. J. Middleton (2006), *Desert dust in the global system,* 287 pp., Springer, Berlin

Goossens, D. and J.L. Rajot (2008). Techniques to measure the dry aeolian deposition of dust in arid and semi-arid landscapes: a comparative study in West Niger. *Earth Surf. Proc. Land.* 33, 178-195.

Govindaraju, K. (1994), 1994 compilation of working values and descriptions for 383 geostandards, *Geostandards Newslett*., 18, 1–158.

Grousset, F. E., et al. (1988), Neodymium isotopes as tracers in marine sediments and aerosols: North Atlantic, *Earth and Planetary Science Letters,* 87(4), 367-378.

Grousset, F. E., et al. (1992), Antarctic (Dome C) ice-core dust at 18 ky BP: Isotopic constraints on origins, *Earth and Planetary Science Letters*, 111, 175-182.

Grousset, F. E., et al. (1998), Saharan wind regimes traced by the Sr-Nd isotopic composition of subtropical Atlantic sediments: Last Glacial Maximum vs Today, *Quaternary Science Reviews,* 17, 395-409.

Grousset, F. E., and P. E. Biscaye (2005), Tracing dust sources and transport patterns using Sr, Nd and Pb isotopes, *Chemical Geology,* 222(3-4), 149-167.

Gubbins, D. (2004), *Time Series Analysis and Inverse Theory for Geophysicists,* 237pp. Cambridge University Press, Cambridge.

Harrison, S. P., et al. (2001), The role of dust in climate changes today, at the last glacial maximum and in the future, *Earth-Science Reviews*, 54(1-3), 43-80.

Haynes, C. V., Jr. (1987), Holocene migration rates of the Sudano-Sahelian wetting from the ArbaViin Desert, Eastern Sahara. , in *Prehistory of Arid North Africa*, edited by A. E. Close, 69-84 pp, Southern Methodist University Press, Dallas.

Hein, L., and N. De Ridder (2006), Desertification in the Sahel: a reinterpretation, *Global Change Biology,* 12(5), 751-758.

Hillaire-Marcel, C., et al. (1983), Radiocarbon chronology of Holocene hydrologic changes in northeastern Mali, *Quaternary Research,* 20(2), 145-164.

Hillier, S. (1995), Erosion, sedimentation and sedimentary origin of clays, in *Origin and Mineralogy of Clays - Clays and the Environment* edited by B. Velde, pp. 162-219 Springer, Berlin.

Hoelzmann, P., et al. (2000), Precipitation estimates for the eastern Saharan palaeomonsoon based on a water balance model of the West Nubian Palaeolake Basin, *Global and Planetary Change,* 26(1-3), 105-120.

Hoelzmann, P., et al. (2004), Palaeoenvironmental changes in the arid and sub arid belt (Sahara-Sahel-Arabian Peninsula) from 150 kyr to present, in *Past Climate Variability through Europe and Africa,* edited by R. W. Batterbee et al., pp. 219-256, Springer, Dordrecht.

Hoernle, K., et al. (1991), Sr Nd Pb isotopic evolution of Gran Canaria: Evidence for shallow enriched mantle beneath the Canary Islands, *Earth and Planetary Science Letters,* 106(1- 4), 44-63.

Holz, C., et al. (2004), Terrigenous sedimentation processes along the continental margin off NW-Africa: implications from grain-size analyses of surface sediments, *Sedimentology,* 51(5), 1145-1154.

Holz, C., et al. (2007), Variability in terrigenous sedimentation processes off northwest Africa and its relation to climate changes: Inferences from grain-size distributions of a Holocene marine sediment record, *Sedimentary Geology*, 202(3), 499-508.

Hong, Y. T., et al. (2003), Correlation between Indian Ocean summer monsoon and North Atlantic climate during the Holocene, *Earth and Planetary Science Letters,* 211(3-4), 371-380.

Hooghiemstra, H. (1988), Changes of major wind belts and vegetation zones in NW Africa 20,000-5000 yr B.P., as deduced from a marine pollen record near cap blanc, *Review of Palaeobotany and Palynology,* 55(1-3), 101-140.

Hughen, K. A., et al. (1996), Rapid climate changes in the tropical Atlantic region during the last deglaciation, *Nature,* 380(6569), 51-54.

Hurtado, S., et al. (2007). A self-sufficient and general method for self-absorption correction in gamma-ray spectrometry using GEANT4, *Nucl. Instrum. Methods A,* 580, 234-237.

Itambi, A. C., et al. (2009), Millennial-scale northwest African droughts related to Heinrich events and Dansgaard-Oeschger cycles: Evidence in marine sediments from offshore

Senegal, *Paleoceanography*, 24(1), PA1205.

Isupova, M. V. & V. N. Mikhailov, (2008), Hydrological and morphological processes in Senegal River mouth area, *Water Res.,* 35, 30–42.

Jacobsen, S. B., and G. J. Wasserburg (1980), Sm-Nd isotopic evolution of chondrites, *Earth and Planetary Science Letters*, 50(1), 139-155.

Jickells, T. D., et al. (2005), Global Iron Connections Between Desert Dust, Ocean Biogeochemistry, and Climate, *Science*, 308(5718), 67-71.

Jullien, E., et al. (2007), Low-latitude "dusty events" vs. high-latitude "icy Heinrich events", *Quaternary Research,* 68(3), 379-386.

Jung, S. J. A., et al. (2004), Stepwise Holocene aridification in NE Africa deduced from dust-borne radiogenic isotope records, *Earth and Planetary Science Letters,* 221(1-4), 27.

Juteau, M., et al., (1986), The Pb-Sr-Nd isotope geochemistry of some recent circum-Mediterranean granites, *Contributions to Minerology and Petrology,* 92, 331-340.

Kattan, Z., et al. (1987), Suspended sediment load and mechanical erosion in the Senegal Basin - Estimation of the surface runoff concentration and relative contributions of channel and slope erosion, *Journal of Hydrology*, 92(1-2), 59-76.

Kennett, J. P. (1990), The younger dryas cooling event: an introduction, *Paleoceanography*, 5(6), 891-895.

Knippertz, P., et al. (2003), Long-term precipitation variability in Morocco and the link to the large-scale circulation in recent and future climates, *Meteorology and Atmospheric Physics,* 83, 67-88.

Koopmann, B. (1981), Sedimentation von Saharastaub im subtropischen Nordatlantik während der letzten 25.000 Jahre, *Meteor Forschungsergebnisse C*, 35, 23-59.

Körner, A., and R. J. Stern (2004), Africa: Pan-african orogeny, in *Encyclopedia of Geology*, edited by R. Selly, et al., pp. 1-12, Elsevier.

Krastel, S., et al. (2004), Cap Timiris Canyon: a newly discovered channel system offshore of Mauritania, *EOS: Transactions American Geophysical Union*, 85, (42), 417-423.

Kröpelin, S., et al. (2008), Climate-Driven Ecosystem Succession in the Sahara: The Past 6000 Years, *Science,* 320(5877), 765-768.

Kuhlmann, H., et al. (2004a), Reconstruction of paleoceanography off NW Africa during the last 40,000 years: influence of local and regional factors on sediment accumulation, *Marine Geology,* 207(1-4), 209-224.

Kuhlmann, H., et al. (2004b), The transition of the monsoonal and the N Atlantic climate system off NW Africa during the Holocene, *Geophysical Research Letters,* 31(22), L22204.

Kuper, R., and S. Kröpelin (2006), Climate-controlled Holocene occupation in the Sahara: motor of Africa's evolution, *Science*, 313, 803-807.

Kutzbach, J. E., and F. A. Street-Perrott (1985), Milankovitch forcing of fluctuations in the level of tropical lakes from 18 to 0 kyr BP, *Nature*, 317(6033), 130-134.

Kutzbach, J. E., et al. (1996), Vegetation and soil feedbacks on the response of the African monsoon to orbital forcing in the early to middle Holocene, *Nature*, 384(6610), 623 – 626.

Lamb, H. F., and S. van der Kaars (1995), Vegetational response to Holocene climatic change: pollen and palaeolimnological data from the Middle Atlas, Morocco, *The Holocene*, 5(4), 400-408.

Lancaster, N. (2002), How dry was dry?-Late Pleistocene palaeoclimates in the Namib Desert, *Quaternary Science Reviews,* 21(7), 769-782.

Lecorche, J. P., et al. (1991), The Mauritanide orogeny and its northern extensions (Western Sahara and Zemmour), West Africa, in *The West African Orogens and Circum-Atlantic Correlatives* edited by R. D. Dallmeyer and Lecorche, pp. 187-229, Springer, Berlin.

Lézine, A.-M. (1989), Late quaternary vegetation and climate of the Sahel, *Quaternary Research,* 32(3), 317-334.

Lézine, A.-M., and J. Casanova (1989), Pollen and hydrological evidence for the interpretation of past climates in tropical west Africa during the holocene, *Quaternary Science Reviews*, 8(1), 45-55.

Liu, Z., et al. (2007), Simulating the transient evolution and abrupt change of Northern Africa atmosphere-ocean-terrestrial ecosystem in the Holocene, *Quaternary Science Reviews,* 26(13-14), 1818-1837.

Loutre, M. F., et al. (1992), Astronomical frequencies for climate research at the decadal to century time scale, *Climate Dynamics,* 7(4), 181-194.

Lutgens, F., and E. Tarbuck (2001), *The atmosphere,* 484 pp., Pentice Hall, New York.

Mahowald, N. M., et al. (2002), Understanding the 30-year Barbados desert dust record, *Journal of Geophysical Research,* 107(D21), 4561.

Mahowald, N. M., et al. (2005), Atmospheric global dust cycle and iron inputs to the ocean, *Global Biogeochem. Cycles,* 19(4), GB4025.

Maronna, R., et al., (2006), *Robust statistics: theory and methods.* 397 pp. Wiley& Sons, New York.

Marret, F., and J.-L. Turon (1994), Paleohydrology and paleoclimatology off Northwest Africa during the last glacial-interglacial transition and the Holocene: Palynological evidences, *Marine Geology,* 118(1-2), 107-117.

Mayewski, P. A., et al. (1993), The Atmosphere During the Younger Dryas, *Science*, 261(5118), 195-197.

Mbow, C., et al. (2008), The history of environmental change and adaptation in eastern Saloum-Senegal-Driving forces and perceptions, *Global and Planetary Change,* 64(3-4), 210-221.

McDermott, F., and C. J. Hawkesworth (1990), Intracrustal recycling and upper-crustal evolution: A case study from the Pan-African Damara mobile belt, central Namibia, *Chemical Geology*, 83(3-4), 263-280.

McIntosh, R., and J. Tainter (2000), *The way the wind blows: climate, history, and human action*, Columbia Univ Pr.

McIntosh, S. K., and R. J. McIntosh (1983), Current Directions in West African Prehistory, *Annual Review of Anthropology,* 12, 215-258.

McGregor, H. V. et al., (2007), Rapid 20th-century increase in coastal upwelling off northwest Africa. *Science* 315, 637-639.

McTainsh, G. (1984), The nature and origin of the aeolian mantles of central northern Nigeria, *Geoderma*, 33(1), 13-37.

Messerli, B. and M. Winiger, (1992), Climate, Environmental Change, and Resources of the African Mountains from the Mediterranean to the Equator. In: *Utilisation et conservation des ressources. Montagnes et Hauts-Pays de l'Afrique.* ed. by Bencherifa, A., pp.3-33, Rabat.

Meyer, I., et al. (2011), Grain-size control on Sr-Nd-isotope provenance studies and impact on paleoclimate reconstructions: an example from deep-sea sediments offshore NW-Africa, *Geochemistry, Geophysics, and Geosystems,12, Q03005, doi:10.1029/2010GC003355.*

Miller, R. L., and I. Tegen (1999), Radiative Forcing of a Tropical Direct Circulation by Soil Dust Aerosols, *Journal of the Atmospheric Sciences*, 56(14), 2403-2433.

Milliman, J. D., and R. H. Meade (1983), World-Wide Delivery of River Sediment to the Oceans, *The Journal of Geology*, 91(1), 1-21.

Milliman, J. D., and J. P. M. Syvitski (1992), Geomorphic/Tectonic Control of Sediment Discharge to the Ocean: The Importance of Small Mountainous Rivers, *The Journal of Geology,* 100(5), 525-544.

Mittelstaedt, E. (1991), The ocean boundary along the northwest African coast: Circulation and oceanographic properties at the sea surface, *Progress in Oceanography,* 26: 307-355.

Moreno, T., et al. (2006), Geochemical variations in aeolian mineral particles from the Sahara-Sahel Dust Corridor, *Chemosphere*, 65(2), 261-270.

Mudelsee, M. (2003), Estimating Pearson's correlation coefficient with bootstrap confidence interval from serially dependent time series, *Math. Geol.,* 35, 651-665.

Muhs, D. R., et al. (1990), Geochemical evidence of Saharan dust parent material for soils developed on Quaternary limestones of Caribbean and Western Atlantic islands, *Quaternary Research,* 33, 157-177.

Müller, P. J. and Schneider, R. (1993), An automated leaching method for the determination of opal in sediments and particulate matter, *Deep-Sea Res. I,* 40, 425-444.

Mueller, P. and J. Vervoort (2010), http://serc.carleton.edu/research_education/geochemsheets/techniques/TIMS.html.

Mulitza, S., et al. (2008), Sahel megadroughts triggered by glacial slowdowns of Atlantic meridional overturning, *Paleoceanography,* 23(4206).

Mulitza, S., et al. (2010), Increase in African dust flux at the onset of commercial agriculture in the Sahel region, *Nature,* 466(7303), 226-228.

Muscheler, R., et al. (2008), Tree rings and ice cores reveal ^{14}C calibration uncertainties during the Younger Dryas, *Nature Geosci,* 1(4), 263-267.

Nakai, S. I., et al. (1993), Provenance of dust in the Pacific ocean, *Earth and Planetary Science Letters,* 119, 143-157.

Neumann, K. (1993), Holocene vegetation of the Eastern Sahara: Charcoal from prehistoric sites, in *Environmental Change and Human Culture in the Nile Basin and Northern Africa Until the Second Millennium B.C.*, edited by L. Krzyzaniak, et al., pp. 153-169, Poznan Archaeological Museum, Poznan.

Niang, A. J., et al. (2008), Fifty years of landscape evolution in Southwestern Mauritania by means of aerial photos, *J. Arid Environ.,* 72, 97-107.

Nicholson, S.E., and H. Flohn (1980), African environmental and climatic changes and the general atmospheric circulation in late Pleistocene and Holocene, *Climatic Change*, 2(4), 313-348.

Nicholson, S. E. (1982), The Sahel: a Climatic Perspective, Club du Sahel, *Committee for Drought Control on the Sahel*, 80 pp., CILSS, OECD.

Nicholson, S. E., et al. (1998), Desertification, Drought, and Surface Vegetation: An Example from the West African Sahel, *Bulletin of the American Meteorological Society*, 79(5), 815-829.

Nicholson, S. E. (2000), The nature of rainfall variability over Africa on time scales of decades to millennia, *Global and Planetary Change*, 26, 137-158.

Nizou, J. et al., (2011), Deciphering signals of late Holocene fluvial and aeolian supply from a shelf sediment depocenter off Senegal (NW Africa), *Journal of Quaternary Science.*

Okin, G. S., et al. (2004), Impact of desert dust on the biogeochemistry of phosphorus in terrestrial ecosystems, *American Geophysical Union*, Washington.

Orange, D., and J.-Y. Gac (1990), Bilan géochimique des apports atmosphériques en domaines sahélien et soudano-guinéen d'Afrique de l'Ouest (bassins supérieurs du Sénégal et de la Gambie), *Géodynamique,* ORSTOM, Paris, 5(l):51-65.

Ott, S.-T., et al. (1991), Analysis of a Trans-Atlantic Saharan Dust Outbreak Based on Satellite and GATE Data, *Monthly Weather Review,* 119(8), 1832-1850.

Pachur, H.-J., and S. Kröpelin (1987), Wadi Howar: Paleoclimatic Evidence from an Extinct River System in the Southeastern Sahara, *Science*, 237(4812), 298-300.

Pachur, H. J., and P. Hoelzmann (2000), Late Quaternary palaeoecology and palaeoclimates of the eastern Sahara, *Journal of African Earth Sciences*, 30, 929-939.

Pittauerová, D. et al. (2009), Application of self-absorption correction method in gamma spectroscopy for ^{210}Pb and ^{137}Cs sediment chronology on the continental slope off NW Africa, *Radioprotection,* 44, 457–461.

Potrel, A., et al. (1996), 3.5 Ga old terranes in the West African Craton, Mauritania, *Journal of the Geological Society*, 153(4), 507-510.

Prince, S. D., et al. (2007), Desertification in the Sahel: a reinterpretation of a reinterpretation, *Global Change Biology,* 13(7), 1308-1313.

Prins, M. A., and G. J. Weltje (1999), End-member modeling of siliciclastic grain-size distributions: the Late Quaternary record of eolian and fluvial sediment supply to the Arabian Sea and its paleoclimatic significance., in *Numerical experiments in stratigraphy: Recent advances in stratigraphic and sedimentologic computer simulations.* SEPM Special Publication 62, edited by J. Harbaugh, et al., pp. 91-111, Society for Sedimentary Geology, Tulsa.

Prospero, J.M. and Carlson, T.N. (1972), Vertical and areal distribution of Saharan dust over the western equatorial North Atlantic Ocean, *Journal of Geophysical Research,* 77: 5255-5265.

Prospero, J. M., and T. N. Carlson (1980), Saharan air outbreaks over the tropical North Atlantic, *Pure and Applied Geophysics,* 119(3), 677-691.

Prospero, J. M., et al. (1981), Atmospheric transport of soil dust from Africa to South America, *Nature*, 289, 570-572.

Prospero, J. M., et al. (2002), Environmental characterization of global sources of atmospheric soil dust identified with the Nimbus 7 total ozone mapping spectrometer (TOMS) absorbing aerosol product, *Reviews of Geophysics,* 40(1), 1-31.

Prospero, J. M., and P. J. Lamb (2003), African droughts and dust transport to the Caribbean: climate change implications, *Science,* 302, 1024-1027.

Pye, K. (1987), *Aeolian dust and dust deposits*, 334 pp., Academic Press, London.

Pye, K., and S. J. Blott (2004), Particle size analysis of sediments, soils and related particulate materials for forensic purposes using laser granulometry, *Forensic Science International,* 144(1), 19-27.

Pye K. and H. Tsoar (2009), *Aeolian sand and sand dunes*, 412 pp., Srpinger Verlag, Berlin.

Ramanathan, V., et al. (2001), Aerosols, cimate, and the hydrological cycle, *Science*, 294, 2119-2124.

Ramdani, F. (1998), Geodynamic implications of intermediate-depth earthquakes and volcanism in the intraplate Atlas mountains (Morocco), *Physics of The Earth and Planetary Interiors,* 108(3), 245-260.

Rea, D. K., et al. (1985), Geologic Approach to the Long-Term History of Atmospheric Circulation, *Science*, 227(4688), 721-725.

Rea, D. K. (1994), The paleoclimatic record provided by eolian deposition in the deep sea: the geologic history of wind, *Reviews of Geophysics,* 32(2), 159-195.

Reed, R. J., et al. (1977), The structure and properties of African wave disturbances as observed during phase III of GATE, *Monthly Weather Review,* 105(3), 317-373.

Renssen, H., et al. (2006), Simulation of the Holocene climate evolution in Northern Africa: The termination of the African Humid Period, *Quaternary International*, 150(1), 95-102.

Ritchie, J.C. et al., (1985), Sediment and pollen evidence for an early to mid-Holocene humid period in the eastern Sahara, *Nature,* 330, 645-647.

Rousseeuw, P. J. and B. C. van Zomeren (1990), Unmasking multivariate outliers and leverage points, *J. Am. Stat. Assoc*., 85, 633-651.

Ruddiman, W. F. (2001), *Earth's climate - past and future,* 465 pp., W.H. Freeman and Company, New York.

Rutberg, R. L., et al. (2005), Sr isotope evidence for sources of terrigenous sediment in the southeast Atlantic Ocean: Is there increased available Fe for enhanced glacial productivity?, *Paleoceanography,* 20(1), PA1018.

Sachs, L. (2002), *Angewandte Statistik,* 852pp. Berlin, Springer.

Salzmann, U. and M. Waller (1998), The Holocene vegetational history of the Nigerian Sahel based on multiple pollen profiles, *Review of Palaeobotany and Palynology,* 100(1-2), 39-72.

Salzmann, U. (2000), Are modern savannas degraded forests?-A Holocene pollen record from the Sudanian vagetation zone of NE Nigeria, *Vegetation History and Archaeobotany,* 9(1), 1-15.

Sarnthein, M. and B. Koopmann (1980), Late Quaternary Deep-Sea Record on Northwest African dust supply and wind circulation, *Palaeoecology of Africa and the Surrounding Islands,* 12, 239-253.

Sarnthein, M., et al. (1981), Glacial and interglacial wind regimes over the eastern subtropical Atlantic and North-West Africa, *Nature*, 293, 193-196.

Sarnthein, M., et al. (1982), Atmospheric and oceanic circulation patterns off northwest Africa during the past 25 million years, in *Geology of the Northwest African Continental Margin,* edited by U. H. v. Rad, K., Sarnthein, M., Seibold, E., pp. 545-604, Springer Berlin.

Sarnthein, M., et al. (1994), Changes in East Atlantic Deepwater Circulation Over the Last 30,000 years: Eight Time Slice Reconstructions, *Paleoceanography*, 9(2), 209-267.

Schmincke, H.-U. (1982), Volcanic and chemical evolution of the Canary Islands, in *Geology of the Northwest African Continental Margin,* edited by U. H. v. Rad, K., Sarnthein, M., Seibold, E., pp. 273-307, Springer, Berlin.

Schmincke, H.-U. (2000), *Vulkanismus*, Wissenschaftliche Buchgesellschaft, Darmstadt.

Schramm, R. and J. Heckel (1998), Fast analysis of traces and major elements with ED(P) XRF using polarized X-rays: TURBOQUANT, *J. Phys.* IV, 8, 335–342.

Schulz, H. D. and M. Zabel (2006), *Marine Geochemistry*. 550pp, Springer, Berlin.

Schulz, H. D., and cruise participants (1998), *Report and preliminary results of Meteor Cruise M41/1*, 124 pp, University Bremen, Bremen.

Schulz, M., and A. Paul (2002), Holocene climate variability on centennial-to-millennial time scales: 1. Climate records from the North-Atlantic realm, in *Climate development and history of the North Atlantic realm*., edited by G. Wefer, pp. 41-54, Springer, Berlin.

Schütz, L., et al. (1981), Saharan dust transport over the North Atlantic Ocean, *Geological Society of America Special Paper*, 186, 87-100.

Shanahan, T. M., et al. (2009), Atlantic Forcing of Persistent Drought in West Africa, *Science*, 324(5925), 377-380.

Smalley, I. J. and C. Vita-Finzi (1968), The formation of fine particles in sandy deserts and the nature of „desert' loess, *Journal of Sedimentary Research,* 38, 766-774

Solmon, F., et al. (2008), Dust aerosol impact on regional precipitation over western Africa, mechanisms and sensitivity to absorption properties, *Geophys. Res. Lett.*, 35(24), L24705.

Sterk, G. (2003), Causes, consequences and control of wind erosion in Sahelian Africa: a review, *Land Degradation & Development,* 14(1), 95-108.

Street-Perrott, F. A., and R. A. Perrott (1990), Abrupt climate fluctuations in the tropics: the influence of Atlantic Ocean circulation, *Nature*, 343(6259), 607-612.

Sturm, J. F. (1999), Using SeDuMi 1.02, a MATLAB toolbox for optimization over symmetric cones. *Optim. Method Softw*. 11, 625-653.

Stuut, J.-B. W., et al. (2009), Aeolian dust in Europe: African sources and European deposits, *Quaternary International,* 198(1-2), 234-245.

Stuut, J.-B. W., et al. (2005), Provenance of present-day eolian dust collected off NW Africa, *Journal of Geophysical Research*, 110(4202), 14.

Stuut, J.-B. W., and F. Lamy (2004), Climate variability at the southern boundaries of the Namib (southwestern Africa) and Atacama (northern Chile) coastal deserts during the last 120,000 yr, *Quaternary Research,* 62(3), 301-309.

Stuut, J.-B. W., et al. (2002), A 300-kyr record of aridity and wind strength in southwestern Africa: inferences from grain-size distributions of sediments on Walvis Ridge, SE Atlantic, *Marine Geology,* 180(1-4), 221-233.

Summerhayes, C. P., et al. (1976), Northwest African Shelf Sediments: Influence of Climate and Sedimentary Processes, *The Journal of Geology,* 84(3), 277-300.

Sun, D., et al. (2008), Contrasting the 2007 and 2005 hurricane seasons: Evidence of possible impacts of Saharan dry air and dust on tropical cyclone activity in the Atlantic basin, *Geophys. Res. Lett.*, 35(15), L15405.

Swap, R., et al. (1992), Saharan dust in the Amazon Basin, *Tellus*, 44B(2), 133-149.

Swezey, C. (2001), Eolian sediment responses to late Quaternary climate changes: temporal and spatial patterns in the Sahara, *Palaeogeography, Palaeoclimatology, Palaeoecology,*167(1-2), 119-155.

Talbot, R. W., et al. (1986), Distribution and geochemistry of aerosols in the tropical North Atlantic troposphere: relationship to Saharan dust, *Journal of Geophysical Research*, 91, 5173-5182.

Tanaka, T. Y., et al. (2005), Possible transcontinental dust transport from North Africa and the Middle East to East Asia, *Atmospheric Environment*, 39(21), 3901-3909.

Teanby, N. A. (2007), Constrained smoothing of noisy data using splines in tension, *Math. Geol.,* 39, 419-434.

Tegen, I., and I. Fung (1995), Contribution to the atmospheric mineral aerosol load from land surface modification, *J. Geophys. Res.*, 100(D9), 18707-18726.

Tegen, I., et al. (2004), Relative importance of climate and land use in determining present and future global soil dust emission, *Geophys. Res. Lett*., 31(5), L05105.

Tjallingii, R., et al. (2008), Coherent high- and low-latitude control of the northwest African hydrological balance, *Nature Geoscience,* 1(10), 670-675.

Tjallingii, R., et al. (2007), Influence of the water content on X-ray fluorescence core-scanning measurements in soft marine sediments. *Geochem. Geophys. Geosyst.,* 8, Q02004.

Torres-Padrón, M. E., et al. (2002), Variability of dust inputs to the CANIGO zone, *Deep Sea Research Part II: Topical Studies in Oceanography,* 49(17), 3455-3464.

Trauth, M. H., and T. Schlüter (2006), *Geological atlas of Africa: with notes on stratigraphy, tectonics, economic geology, geohazards and geosites of each country*, 272 pp., Springer, Berlin.

Tucker, C. J., et al. (1991), Expansion and Contraction of the Sahara Desert from 1980 to 1990, *Science*, 253(5017), 299-300.

Vogt, C., et al. (2002), Investigation of the Clay Fraction (<2 μm) of the Clay Minerals Society Reference Clays, *Clays and Clay Minerals*, 50(3), 388-400.

Vörösmarty, C. J., et al. (2000), Global system of rivers: its role in organizing continental land mass and defining land-to-ocean linkages, *Global Biogeochemical Cycles*, 14(2), 599-621.

Webb, J. L. A. (1995), *Desert Frontier: Ecological and Economic Change Along the Western Sahel 1600-1850,* University of Wisconsin Press.

Webster, P. J. (1987), *The elementary monsoon, in Monsoons,* edited by J. S. Fein and P. L. Stephens, pp. 3-32, Wiley-Interscience.

Weldeab, S., et al. (2002), Provenance of lithogenic surface sediments and pathways of riverine suspended matter in the Eastern Mediterranean Sea: evidence from $^{143}Nd/^{144}Nd$ and $^{87}Sr/^{86}Sr$ ratios, *Chemical Geology,* 186(1-2), 139-149.

Weltje, G. J. and Tjallingii, R. (2008), Calibration of XRF core scanners for quantitative geochemical logging of sediment cores: Theory and application, *Earth Planetary Science Letters,* 274, 423-438.

Weltje, G. J., and M. A. Prins (2007), Genetically meaningful decomposition of grain-size distributions, *Sedimentary Geology*, 202(3), 409-424.

Weltje, G. J., and M. A. Prins (2003), Muddled or mixed? Inferring palaeoclimate from size distributions of deep-sea clastics, *Sedimentary Geology*, 162(1), 39-62.

Weltje, G. J. (1997), End-member modelling of compositional data: Numerical-statistical algorithms for solving the explicit mixing problem, *Journal of Mathematical Geology*, 29(4), 503-549.

White, W. M., et al. (1986), Hf isotope ratios of marine sediments and Mn nodules: evidence for a mantle source of Hf in seawater, *Earth and Planetary Science Letters*, 79(1-2), 46-54.

Wien, K., et al. (2005), Fast application of X-ray fluorescence spectrometry aboard ship: how good is the new portable Spectro Xepos analyser?, *Geo-Mar. Lett.,* 25, 248–264.

Wright, J. B., et al. (1985), *Geology and Mineral Resources of West Africa,* Allen and Unwin, London.

Wynn, R.B. et al., (2000), Turbidity current sediment waves on the submarine slopes of the western Canary Islands, *Marine Geology,* 163: 185–198.

Wynn, R. B., et al. (2002), Turbidite depositional architecture across three interconnected deep-water basins on the north-west African margin, *Sedimentology*, 49(4), 669-695.

Yoshioka, M., et al. (2007), Impact of Desert Dust Radiative Forcing on Sahel Precipitation: Relative Importance of Dust Compared to Sea Surface Temperature Variations, Vegetation Changes, and Greenhouse Gas Warming, *Journal of Climate*, 20(8), 1445-1467.

Zabel, M., et al. (1999), Significance of the sedimentary Al:Ti ratio as an indicator for variations in the circulation patterns of the equatorial North Atlantic, *Paleoceanography*, 14(6), 789-799.

Zabel, M., et al. (2001), Late Quaternary climate changes in Central Africa as inferred from terrigenous input to the Niger Fan, *Quaternary Research*, 56, 207-217.

Zühlsdorff, C., et al. (2007), Late Quaternary sedimentation within a submarine channel-levee system offshore Cap Timiris, Mauritania, *Marine Geology*, 240(1-4), 217-234.